SHOCK TEMPERATURES OF MATERIALS: EXPERIMENTS AND APPLICATIONS TO THE HIGH PRESSURE EQUATION OF STATE

Thesis by

Gregory Allen Lyzenga

In Partial Fulfillment of the Requirements

for the Degree of

Doctor of Philosophy

California Institute of Technology

Pasadena, California

1980

(Submitted May 19, 1980)

ACKNOWLEDGMENTS

I express my sincere gratitude to Thomas J. Ahrens for his invaluable support and guidance throughout all phases of this research. I also am extremely grateful for the generous support of the Fannie and John Hertz Foundation during my graduate residence. I have benefited greatly from my associations and discussions with the faculty and students of the Institute; and, in particular, the help of Raymond Jeanloz and Ian Jackson, in addition to that of T. J. Ahrens, is gratefully acknowledged. The experimental work presented here has been made possible through the expert assistance of the staff members of the Seismological Laboratory, and I am grateful to E. Gelle, C. Hudson, J. Long, M. Long, N. Motta, E. Steffensen and R. Wickes for their efforts. J. K. Erickson and his colleagues at the Jet Propulsion Laboratory have contributed to the success of this work as well.

The experiments of this research program have been largely supported by the facilities and personnel of Lawrence Livermore Laboratory, and I am very grateful for this opportunity and for the valuable advice and assistance of A. C. Mitchell, W. J. Nellis and M. Van Thiel. The technical assistance of D. Bakker, E. Jerbic, H. Martinez, J. Samuels, and C. Wallace of LLL is greatly appreciated. Thanks are extended to J. W. Shaner of Los Alamos Scientific Laboratory for motivating advice and valuable collaborations. I am most grateful to Helen F. White and Laszlo Lenches for extraordinary help in the preparation of this thesis. In addition to the support from DOE through Lawrence Livermore Laboratory,

the financial support of the National Science Foundation and NASA is gratefully acknowledged.

The support and understanding of my wife, Mary White Lyzenga, and of my families have ranged from technical and financial to spiritual backing, and it is to them that this work is dedicated.

ABSTRACT

The experimental determination of temperatures in the high-pressure shocked state of condensed matter provides a useful supplement to equation-of-state models derived from Hugoniot measurements. An optical pyrometry technique has been developed to obtain temperature measurements during impact-driven shock wave experiments with solid and liquid samples at pressures near 100 GPa. Experimental results confirm that throughout moderate ranges of shock pressure amplitude, transparent dielectrics emit thermal radiation from the region of the shock front, with a spectrum which is characteristic of the Hugoniot state temperature. Shock temperatures in sodium chloride crystals have been measured in the pressure range 70-105 GPa. The observed temperatures, between 4000 and 8000 K, are in agreement with the results of earlier determinations and with calculations assuming the occurrence of shock-induced melting. Results of experiments to measure shock temperatures in metallic silver include a successful measurement of 5950 K at a pressure of 185 GPa. This result is consistent with the melting of silver under shock, with a melting pressure dependence described by the Lindemann criterion.

Shock temperature measurements in silica (SiO_2) have produced anomalous results suggestive of melting occurring in the stishovite phase near 100 GPa pressure and 4700 K temperature. Experimental measurements with α-quartz and fused silica samples extend from pressures of approximately 60 GPa to 140 GPa, with shock temperatures between approximately 4500 K

and 7000 K. The experimental data allow quantification of the thermodynamic relations among silica phases, including heats of transition and the Grüneisen parameter. Shock temperatures in single crystal forsterite (Mg_2SiO_4) between pressures of 150 GPa and 175 GPa range from 4500 K to 4950 K, a result which is consistent with occurrence of a polymorphic solid state transition accompanied by a substantial heat of transition (~1.5 MJ/kg). These results have potentially important implications for solid earth geophysics, and knowledge of the melting curves of candidate minerals of the earth's mantle provides some constraints on the geotherm.

Hugoniot temperatures have been measured in liquid water between approximately 50 GPa and 80 GPa, with results ranging from 3500 K to 5400 K. The observed temperatures are well reproduced by theoretical calculations assuming a constant specific heat model, but further work is required to characterize fully the thermal variation of H_2O properties at high temperature. Compression measurements in pressure-volume states other than Hugoniot shock states and, in particular, in states of compression at constant entropy can provide both independent thermal equation-of-state information and the properties of high-density condensed phases inaccessible to shock wave experiments. Numerical calculations have been carried out for hypothetical experiments on water as well as carbon dioxide and liquid molecular hydrogen. The results of these calculations indicate that various experimental impact configurations may be employed to convert shock compression into isentropic compression, with pressures on the order of 100 GPa attained via impact velocities of a few kilometers per second. In the case of water, a net entropy production of a few percent of the Hugoniot entropy at the same pressure is predicted on the basis of these calculations.

TABLE OF CONTENTS

Chapter 1

SHOCK TEMPERATURES AND THE THERMAL EQUATION OF STATE

The Hugoniot Shock State and Thermal Pressure in Solids

The compression of condensed materials by passage of a steady, one-dimensional shock wave through macroscopic specimens is a useful technique for the study of equations of state as well as the structure and chemical properties of matter at high pressures. The theory of the formation and propagation of shocks in matter is the subject of a large body of literature in gasdynamics and hydrodynamics. The present study considers the application of these results to the study of solids, and what follows is a brief sketch of the development of some of the useful results.

In general, a compressive disturbance of finite pressure amplitude in a homogeneous medium does not propagate with a constant profile, since the compressibility (and therefore the sound speed) of real substances changes with increasing pressure. For most materials, the adiabatic compressibility increases with pressure so that infinitesimal acoustic disturbances propagate at ever higher velocities as the pressure increases in the material. As discussed in the review material of [1], an initial pressure pulse of arbitrary spatial profile will, as time progresses, steepen in its pressure gradient as later, higher pressure disturbances overrun the beginning of the wave. For such a material, in which $(\partial^2 P/\partial v^2)_s > 0$ (the Bethe-Weyl condition for stability of weak shocks),

the wave steepens and stabilizes as a single shock transition, which is a nearly discontinuous pressure profile of the kind illustrated in Figure 1-1.

The processes within the narrow region of the shock front are important to a consideration of the final compressed material state or Hugoniot state. As the gradients of pressure and density in a steepening wave become very large, dissipative effects of viscosity and heat conduction become important in the flow, and these effects result in the net production of entropy in the final state. Zel'dovich and Raizer [1] discuss the role of dissipative processes in the shock front, demonstrating that while the net entropy difference between the initial and final states is independent of the details of these processes, the spatial width and structure of the front depend upon the viscosity and thermal conductivity of the fluid. In particular, the viscous shock front width is proportional to the coefficients of viscosity and thermal conductivity, each of which is proportional to molecular mean free path in the limit of gas or dilute fluid behavior.

For the practical purposes of most experimental measurements of pressure and density, the shock front is treated as a simple surface of discontinuity in the properties of the material. The present study considers the applications of shocks in solids, in which the details of the scale and mechanism of the shock front rise may differ from the gasdynamic case. In typical experiments with solids, the shock front may be as narrow as several atomic lattice spacings, or much larger if rate-limiting structure changes occur. Nevertheless, the stability of the quasi-discontinuous steady shock outlined above allows the final states of pressure, density and energy to be determined from considerations independent of the details of the front. The locus of such final states will be referred to as the

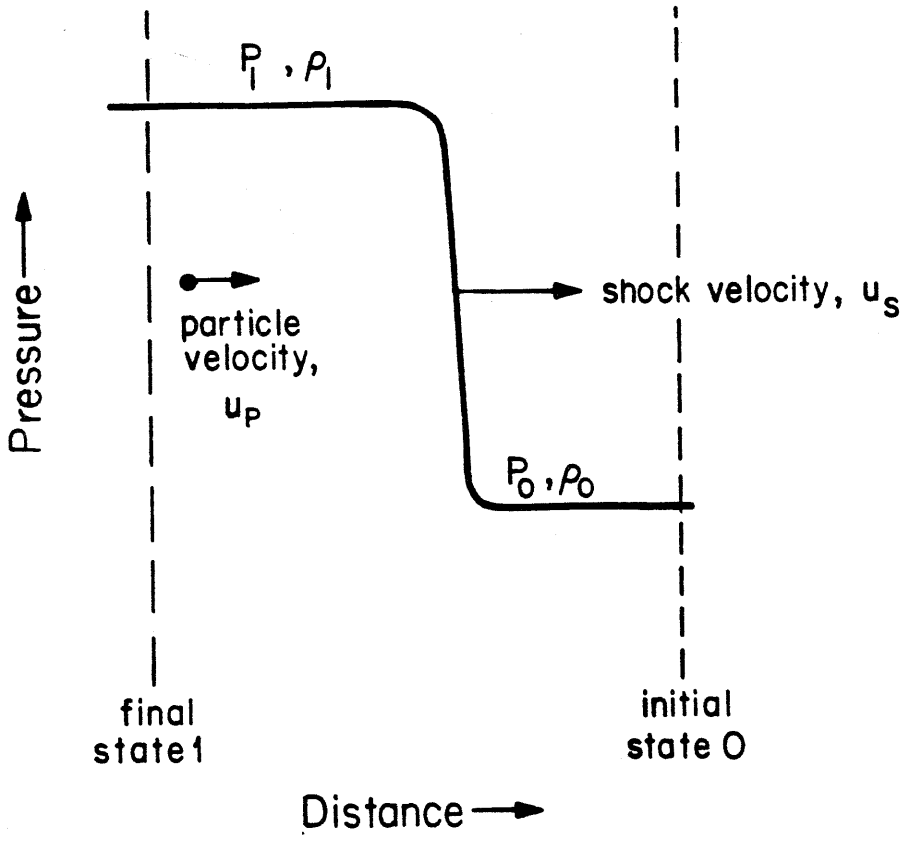

Figure 1-1. Schematic profile of pressure and flow in steady shock front. Shock front propagates into undisturbed material at velocity u_s, leaving material at pressure P_1 and moving with mass velocity u_p. Dashed lines represent boundaries fixed in the material and moving with the mass velocity.

Hugoniot or shock adiabat of a given material.

In considering the motion of mass under the influence of a shock wave moving into undisturbed material at velocity u_s, the final velocity of material behind the front or the particle velocity will be denoted by u_p. V denotes the specific volume of a given state and is the reciprocal of the density ρ. The conservation of mass in the flow of material through the shock front as shown in Figure 1-1 requires that the flux of mass into the leading edge of the front equals the flux of mass emerging in the final state. That is,

$$\rho_0 u_s = \rho_1 (u_s - u_p). \tag{1}$$

Now consider the region between the dashed lines in Figure 1-1 including the shock front. The net stress on the cross section of this region must equal the rate of momentum per unit area appearing within the boundaries. This gives rise to the second conservation equation,

$$P_1 - P_0 = \rho_0 u_s u_p . \tag{2}$$

Finally, the rate at which work is done on the moving boundary is equal to the time rate of change of the kinetic plus internal energy of the material within the region. Therefore,

$$P_1 u_p = \rho_0 u_s [u_p^2/2 + (E_1 - E_0)], \tag{3}$$

where E is the internal energy per unit mass. These three equations involve the five quantities u_s, u_p, P_1, ρ_1, and E_1 appropriate to the final state. This means that specification of any two of these quantities suffices for a complete description of the Hugoniot state, and in particular, an experimental measurement of the kinematic parameters u_s and u_p for a shock wave, allows the direct calculation of pressure,

density and internal energy in the Hugoniot state.

Rearrangement of the three conservation relations yields

$$u_s = V_0 \sqrt{\frac{P_1-P_0}{V_0-V_1}} , \tag{4}$$

$$u_p = \sqrt{(P_1-P_0)(V_0-V_1)} , \tag{5}$$

and

$$E - E_0 = \frac{1}{2}(P_1+P_0)(V_0-V_1) , \tag{6}$$

which are the familiar forms of the Rankine-Hugoniot relations. While the shock compression process is adiabatic, it is not isentropic since it is accompanied by a large amount of irreversible heating. This is evident not only from a consideration of the discontinuous shock transition but also upon examination of the internal energy rise given in equation (6). As illustrated graphically in Figure 1-2, the internal energy jump, which is numerically equal to the area of the shaded triangle, is greater than the area under any hypothetical adiabat ($\int PdV$) connecting the initial and final states.

The above derivation has referred throughout to the hydrostatic pressure P, appropriate to an ideal fluid with no shear strength. It should be emphasized that the Rankine-Hugoniot equations apply with equal validity for solids as well as fluids of arbitrary rheological properties. When the stress component along the direction of shock propagation replaces the hydrostatic pressure, the above derivation remains valid. The one-dimensional symmetry of the assumed flow causes this stress component to be the only component which enters into the mass flow, momentum or energy of the final strained state. As a matter of practical application, the pressures

considered in the present study (10^5-10^6 bars) are so large compared with the yield strengths of solids that the difference between the Hugoniot and the hydrostat is negligible. Thus, in the treatment that follows, the distinction between the pressure P and the dynamic stress will be ignored.

As seen in Figure 1-2, the actual compression isentrope of a material lies everywhere at lower pressures than the Hugoniot at the same density, the pressure offset between the two being determined by the difference in thermal energy between the two states. For this reason, the pressure difference ΔP is called the thermal pressure difference between the two states. The zero point of thermal pressure at a given volume lies on the cold compression isotherm at absolute zero temperature, since the pressure on this zero isotherm is due to the elastic deformation of the cold crystal lattice with no thermal component (except for pressure arising from the volume dependence of zero-point quantum oscillations).

Obtaining the high-pressure equation of state of a given solid then reduces to the separate problems of the nonthermal elastic pressure component and the thermal pressure. In experimental practice, the compression isotherm is difficult to obtain except at relatively modest pressures, while the Hugoniot curve is routinely measured for most solids to pressures of several megabars (1 megabar = 100 GPa $\approx 10^6$ atmospheres). Therefore, in characterizing the complete equation of state of a solid, we need to determine the relationship between thermal pressure and thermal energy at a given volume. In short, a thermal equation of state of the form

$$P = P_{thermal}(E,V) + P_{zero}(V) \qquad (7)$$

is sought.

Consider a crystalline solid which consists of N atoms within a total

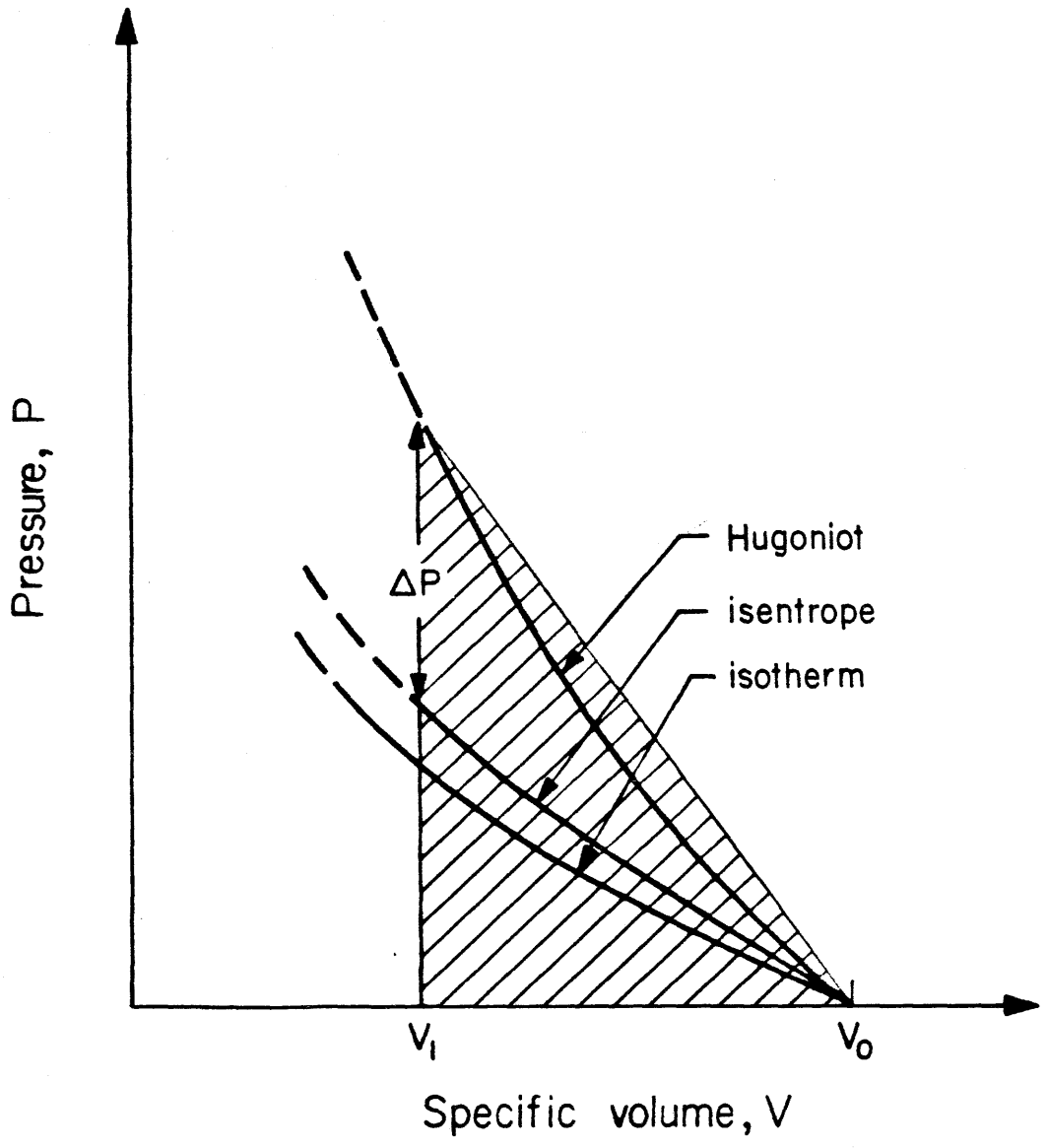

Figure 1-2. Relation of shock adiabat (Hugoniot) to equilibrium curves of isothermal and isentropic compression. Hugoniot energy $1/2\ P_1(V_0-V_1)$ is given by area of shaded triangle. ΔP denotes pressure difference due to thermal contribution.

volume v. The solid may vibrate with 3N normal mode frequencies in the semiclassical harmonic oscillator model. The solid may then be described as an ensemble of quantum oscillators, characterized by 3N quantum numbers n_j for the mode frequencies ν_j. The total internal energy of this solid is

$$U = U_0 + \sum_{j=1}^{3N} n_j h\nu_j \ , \tag{8}$$

where U_0 is the cold compression energy of the lattice at absolute zero, plus the zero-point quantum oscillator energy

$$U_{zp} = \sum_{j=1}^{3N} \frac{1}{2} h\nu_j \ . \tag{9}$$

Here and below, h is equal to Planck's constant.

The statistical mechanical partition function for this system is given by a sum of the terms $\exp(-\varepsilon_j/kT)$ for ε_j the energy of the j^{th} microstate accessible to the system. Thus,

$$Z = \sum_{n_1} \sum_{n_2} \cdots \sum_{n_{3N}} \exp(-\sum_j n_j h\nu_j/kT)\exp(-U_0/kT). \tag{10}$$

Expressing this sum as the product of each of the independent sums over the n_j,

$$Z = \exp(-U_0/kT) \sum_{n_1} \exp(-n_1 h\nu_1/kT) \cdots \sum_{n_{3N}} (-n_{3N} h\nu_{3N}/kT). \tag{11}$$

Each of these sums is evaluated as a geometric series, yielding

$$Z = \exp(-U_0/kT) \prod_{j=1}^{3N} [1 - \exp(-h\nu_j/kT)]^{-1}. \tag{12}$$

Given this partition function, we may write an expression for the Helmholtz free energy,

$$F = -kT \ \ell nZ = U_0 + \sum_j kT \ \ell n[1 - \exp(-h\nu_j/kT)]. \tag{13}$$

The entropy is given by

$$S = -\left(\frac{\partial F}{\partial T}\right)_v \tag{14}$$

and the internal energy is $U = F + TS$. Thus we obtain

$$U = U_0 + \sum_j \frac{h\nu_j}{\exp(h\nu_j/kT) - 1} \tag{15}$$

for the internal energy of the solid in thermal equilibrium at temperature T.

Similarly, the pressure may be evaluated from F using

$$P = -\left(\frac{\partial F}{\partial v}\right)_T \tag{16}$$

which gives

$$P = -\frac{dU_0}{dv} + \sum_j \frac{-h\left(\frac{\partial \nu_j}{\partial v}\right)_T}{\exp(h\nu_j/kT) - 1} \tag{17}$$

or

$$P = P_{zero}(v) + \frac{1}{v}\sum_j \gamma_j \frac{h\nu_j}{\exp(h\nu_j/kT) - 1} \tag{18}$$

where

$$\gamma_j \equiv -\frac{v}{\nu_j}\left(\frac{\partial \nu_j}{\partial v}\right)_T = -\left(\frac{\partial\, \ell n \nu_j}{\partial\, \ell n v}\right)_T . \tag{19}$$

The approximation which was originally suggested by Grüneisen [2,3] is that each of the ν_j undergoes the same fractional change for a change in volume. Note that for a perfectly harmonic solid, all the γ_j vanish and there is no thermal pressure or thermal expansion. In this sense, the γ_j are a measure of the anharmonicity of the solid.

If the Grüneisen assumption is made and the γ_j are all equal, they factor out of the summation, yielding a simple relationship between thermal pressure and thermal energy. In this approximation,

$$P_{thermal} = \frac{\gamma}{v}\sum_j \frac{h\nu_j}{\exp(h\nu_j/kT) - 1} \tag{20}$$

and we obtain

$$P_{thermal} = \frac{\gamma}{v} U_{thermal} = \frac{\gamma}{V} E_{thermal} \qquad (21)$$

which is the Mie-Grüneisen equation of state. In the Mie-Grüneisen formulation, γ is assumed to be a function only of volume, so that the thermal pressure of a solid is assumed to be directly proportional to the thermal internal energy at fixed volume.

This equation of state is widely used as a description of the solid at high pressures, with γ treated as an empirically determined parameter. Within the assumption that Mie-Grüneisen is valid, γ may be derived from thermodynamic properties of the solid. If equation (21) is valid, then

$$\gamma(V) = V\left(\frac{\partial P}{\partial E}\right)_V = \alpha V K_T / C_v. \qquad (22)$$

This is a straightforward application of thermodynamic identities, where α is the thermal coefficient of volume expansion, K_T is the isothermal bulk modulus, and V and C_v are the specific volume and heat capacity per unit mass respectively. Thus the formal Grüneisen parameter is derivable from macroscopic material properties that are easily measurable, at least at standard conditions of pressure and temperature.

In practice, the Mie-Grüneisen equation is commonly assumed to hold for general substances, even in the case of liquids for which any argument about vibrational modes breaks down. It is interesting to note that formally the Mie-Grüneisen equation of state holds for the ideal gas, with γ equal to a constant whose magnitude depends upon the ratio of specific heats. The Mie-Grüneisen equation breaks down when the thermal pressure exhibits other than a simple proportionality to internal energy, and this failure is sometimes expressed by allowing a temperature (or energy)

dependence for γ.

In applying these results to the shock wave equation of state, it is apparent that a knowledge of $\gamma(V)$ allows the calculation of the pressure offset between the Hugoniot and the isentrope, since the internal energies along each of these curves is known as a function of V. Similarly, given a compression isotherm, its internal energy is given by

$$E - E_0 = \int_{V_0}^{V} \left(T_0 \frac{\gamma C_v}{V} - P\right) dV \tag{23}$$

from a TdS thermodynamic relation.

Theoretical Shock Temperatures

It is apparent from the above discussion that the temperature of a Mie-Grüneisen material in a state on the Hugoniot curve will depend upon the energy difference between the Hugoniot state and the isothermal state at the same volume, with this difference depending upon γ. Furthermore, C_v, the specific heat at constant volume, will determine the Hugoniot temperature, given this energy difference.

The simplest scheme for performing this calculation, which was given by Walsh and Christian [4], requires the imposition of some restrictions on γ and C_v, and it is limited in the range of conditions under which it is applicable. The Walsh and Christian analysis begins with the thermodynamic identities,

$$TdS = C_v dT + T\gamma \frac{C_v}{V} dV, \tag{24}$$

and

$$TdS = dE + PdV. \tag{25}$$

Now for states on the Hugoniot,

$$E - E_0 = \frac{1}{2} P(V_0 - V), \tag{26}$$

where the initial pressure P_0 is taken as zero. If equation (25) describing the first law of thermodynamics is integrated from the initial state (zero subscripts) along the path described by the Hugoniot to an ultimate state of P, V, and S, we have

$$\int_{S_0}^{S} TdS = \frac{1}{2} P(V_0 - V) + \int_{V_0}^{V} PdV. \tag{27}$$

Differentiating with respect to V, we define

$$\frac{d}{dV} \int_{S_0}^{S} TdS = \frac{1}{2} \frac{d}{dV} P(V)(V_0 - V) + \frac{1}{2} P(V) \equiv f(V), \tag{28}$$

which is a function of V obtained directly from the Hugoniot curve, P(V). Now if the specific heat may be regarded as constant, equation (24) yields

$$\int_{S_0}^{S} TdS = C_v \int_{T_0}^{T} dT + \int_{V_0}^{V} T\gamma \frac{C_v}{V} dV, \tag{29}$$

and

$$\frac{d}{dV} \int_{S_0}^{S} TdS = f(V) = C_v \frac{dT}{dV} + \frac{\gamma C_v}{V} T. \tag{30}$$

This is a first-order ordinary differential equation for T(V), whose solution is given by

$$T(V) = \exp\left(-\int_{V_0}^{V} (\gamma/V')dV'\right)\{T_0 + \int_{V_0}^{V} \frac{f(V')}{C_v} \exp\left[\int_{V_0}^{V'} (\gamma/v)dv\right]dV'\}. \tag{31}$$

An additional result of the Walsh and Christian formulation is independent of restrictive assumptions about C_v. If $\gamma(V)$ is correctly given by the Mie-Grüneisen equation, then the temperature gradient measured along the Hugoniot curve is

$$\left.\frac{dT}{dV}\right|_H = \frac{1}{C_v}\left[\frac{1}{2}(V_0-V)\left.\frac{dP}{dV}\right|_H + \frac{1}{2}P - \frac{T\gamma C_v}{V}\right]. \qquad (32)$$

The final term within the brackets which involves γ is typically small (~10%) compared with the first two pressure terms, so it is apparent that under most circumstances, the effect of C_v on the slope of the temperature Hugoniot is considerably greater than that of γ.

The Walsh and Christian scheme for calculation of shock temperatures is applicable for cases in which the quantities in equation (31), including γ, the Hugoniot pressure, and its derivative are continuous properties of a single phase. If the material under consideration undergoes a shock-induced transformation to a new phase, the above derivation breaks down.

As illustrated in Figure 1-3, when a phase transition occurs under shock wave loading, the locus of final shocked states passes through a region of mixed phases over a range of pressures (and temperatures). This contrasts with the behavior observed during isothermal compression, in which case the passage through the mixed phase regime occurs at constant pressure. Under isothermal compression, the path through the mixed phase region represents a locus of equilibrium states between two coexistent phases at constant T. The Gibbs phase rule thus requires the pressure to remain fixed as the mole ratio of phase A to phase B varies. The Hugoniot curve, however, does not describe an isothermal or even an equilibrium path, but merely a locus of final shocked states, so that a

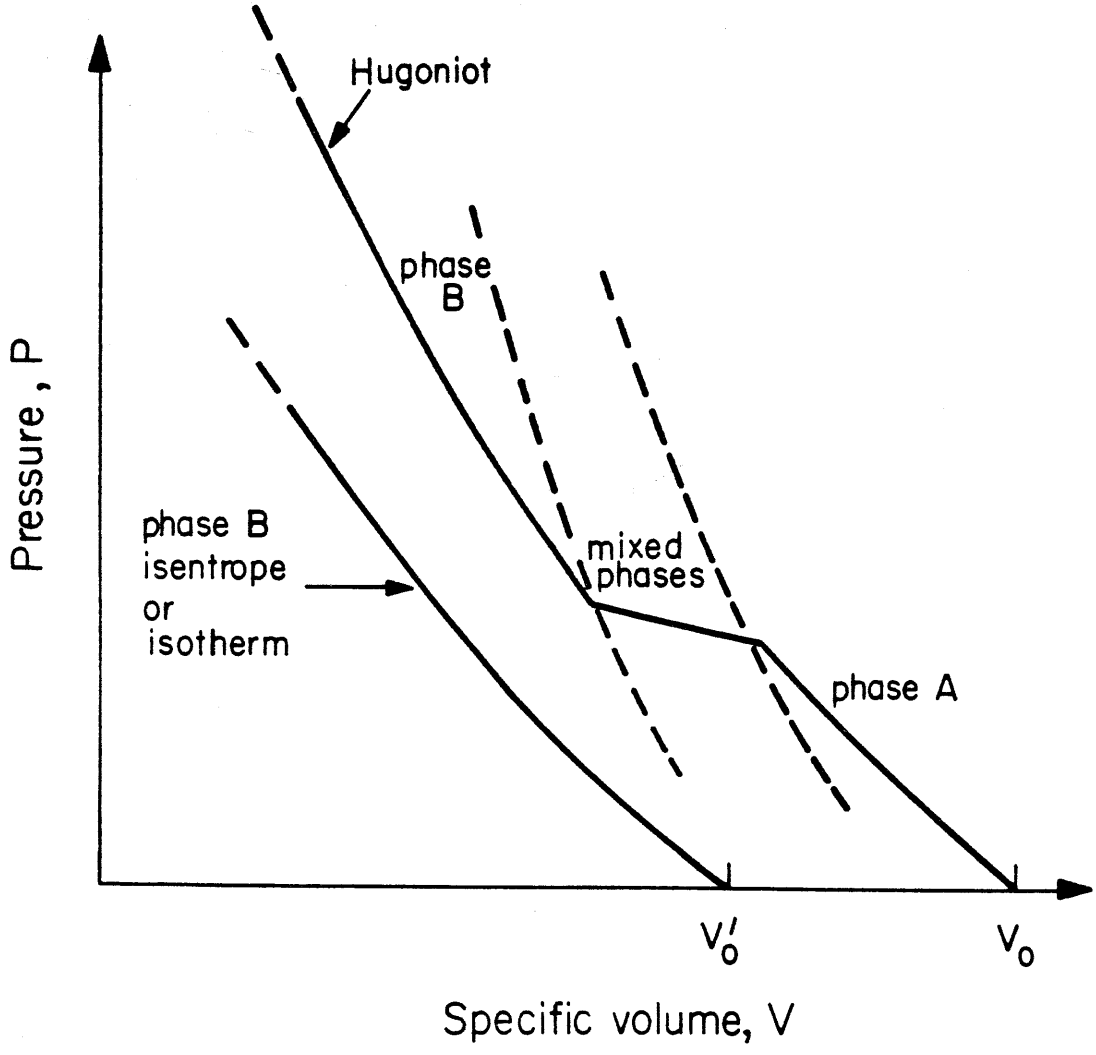

Figure 1-3. Hugoniot curve with phase transition. High-pressure phase has metastable zero-pressure specific volume of V_0'.

finite range of pressures occurs over which the Hugoniot energy induces only partial transformation from initial phase A to final phase B. A more detailed description of this behavior under various conditions of density contrast and latent heat between phases is given by McQueen et al. [5].

Since continuous integration along the Hugoniot through the mixed phase regime is not applicable, an alternate approach to the calculation of Hugoniot temperatures is required. As illustrated schematically in Figure 1-3, we may construct, at least in principle, an isotherm or isentrope of compression of the high-pressure phase from a metastable state at standard pressure and temperature, and specific volume V_0'. Given such a reference curve for the high-pressure phase (denoted by the subscript "R"), the Mie-Grüneisen equation gives the energy difference between the Hugoniot and reference curve at a given volume as,

$$E_H - E_R = \frac{V}{\gamma}(P_H - P_R). \tag{33}$$

The temperature T_H in the Hugoniot state is then obtained by solving

$$E_H - E_R = \int_{T_R}^{T_H} C_v dT. \tag{34}$$

Here, C_v and γ assume values appropriate to the new phase and are assumed known. When the reference curve is the isotherm, the reference temperature T_R is simply T_0, the standard state temperature (usually 298 K). In the case that the isentrope of compression is used as a reference curve, T_R becomes

$$T_R = T_0 \exp\left(-\int_{V_0}^{V} (\gamma/V)dV\right), \tag{35}$$

which is obtained by setting $TdS = 0$ in equation (24).

Since in the vast majority of cases, the Hugoniot curve is the only experimentally determined equation of state at very high pressures, the reference curve (either isotherm or isentrope) must be calculated. We will consider first the calculation of the isentrope, assuming that $\gamma(V)$ for the high-pressure phase is a known function. Equating the Hugoniot energy at some arbitrary volume with the energy of isentropic compression along the unknown adiabat $P_S(V)$ plus the energy of heating the material at constant volume to the Hugoniot pressure $P_H(V)$,

$$\frac{1}{2} P_H(V_0-V) = E_{tr} - \int_{V_0'}^{V} P_S dV + \frac{V}{\gamma} (P_H-P_S). \qquad (36)$$

Here, E_{tr} represents the specific energy added to the stable low-pressure phase in order to transform it into the high-pressure phase at S.T.P. This integral equation for the unknown curve $P_S(V)$ may be solved numerically, for example, by approximating it with a centered difference equation after the manner of McQueen *et al.* [5]. Alternatively, differentiation of this equation yields

$$\frac{dP_S}{dV} = \frac{dP_H}{dV} + \frac{\gamma}{V} \frac{d}{dV}\left(\frac{V}{\gamma}\right)(P_H-P_S) + \frac{\gamma}{2V}\left[(V_0-V) \frac{dP_H}{dV} - P_H - 2P_S\right]. \qquad (37)$$

This ordinary differential equation for $P_S(V)$ is readily solved by numerical integration techniques, for example the Runge-Kutta method, and such methods are well suited to computer or calculator solution.

A practical complication presents itself in the actual calculation of a high-pressure isentrope in this manner. In most cases (for example, see the calculations for SiO_2 and Mg_2SiO_4) the zero-pressure volume of the metastable phase is at a larger volume than the beginning of the high-pressure phase region of the Hugoniot curve. This means that unless

equation (37) is integrated from a sufficiently high starting pressure, the integration is performed through a region where $P_H(V)$ describes the mixed phase regime, and equation (36) is no longer valid.

This problem is avoided by replacing the Hugoniot $P_H(V)$, which is centered on the initial low-pressure phase, with the metastable Hugoniot $P'_H(V)$. This is the locus of shocked states that would be achieved if the initial material was metastable high-pressure phase. This metastable Hugoniot is calculable from the principal Hugoniot by a straightforward application of the Mie-Grüneisen equation and a knowledge of $\gamma(V)$ and ΔE_{tr}. This calculation is detailed by McQueen et al. [5,6], but for the present discussion we will specialize to a particular case. Once the metastable Hugoniot is determined, calculation of the isentrope from equation (37) may proceed unhindered, since $P'_H(V)$ now refers strictly to the phase of interest.

It will be convenient to consider the special case of a metastable Hugoniot curve for material which is in the transformed phase (of specific volume V'_0) but which has been given an initial porosity so that its bulk volume equals V_0, the specific volume of the low-pressure phase. In this special case, the pressure offset between the principal Hugoniot and its metastable counterpart assumes a particularly simple form.

Referring to Figure 1-4, the energy of a state on the principal Hugoniot (state 1) is simply

$$E_H(1) = \frac{1}{2} P_H(1)(V_0-V). \tag{38}$$

On the other hand, the energy of a sample which has been prepared in the high-pressure phase and shocked from a porous initial volume V_0 is

$$E_H(2) = E_{tr} + \frac{1}{2} P'_H(2)(V_0-V). \tag{39}$$

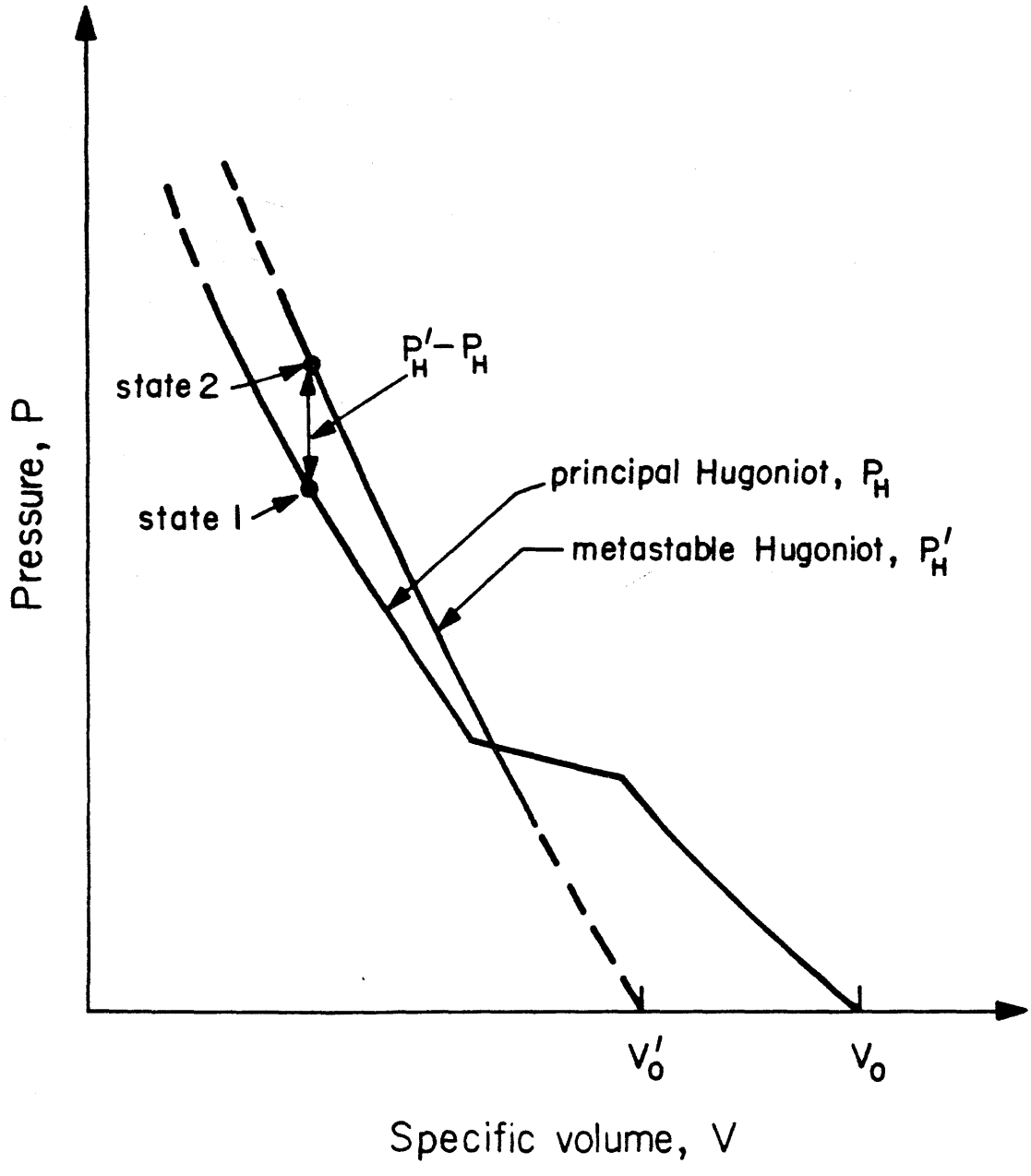

Figure 1-4. Metastable high-pressure phase Hugoniot derived from principal experimental Hugoniot. When metastable initial phase has porous volume V_0, the pressure offset $P_H' - P_H$ is simply proportional to the transition energy E_{tr}.

Taking the difference between these energies and equating it to the Mie-Grüneisen offset, we obtain an expression which solved for the pressure difference gives

$$P'_H - P_H = \frac{\gamma}{V} E_{tr}\{1 - \frac{\gamma}{2}[(V_0/V) - 1]\}^{-1}. \qquad (40)$$

Since the principal Hugoniot P_H is experimentally measured, application of equation (40) allows the direct conversion of this curve into P'_H. The metastable Hugoniot P'_H passes in principle through zero pressure at volume V'_0, since negligible pressure is required to collapse the pore space and bring the material to normal density. The effect of the initial porosity is instead manifested in the subsequent compression and its higher thermal pressure (see, for example, Al'tshuler [7]).

Recapitulating, the metastable Hugoniot obtained as described above and fit with an appropriate analytic interpolation formula is used in equation (37) to solve for the high-pressure isentrope $P_S(V)$. E_{tr} enters directly into P'_H, and this transition energy thus has an immediate and important effect upon the position of the calculated isentrope. With this isentrope in hand, it is finally a simple matter to apply equations (33) and (34) with a suitable model for the specific heat C_v to obtain the Hugoniot temperature T_H at each value of V in the phase of interest. The foregoing discussion applies with equal validity to materials which do not undergo a shock-induced phase change, but since this derivation is based upon the same Mie-Grüneisen assumptions as the single-phase Walsh and Christian calculation, their results are identical in that application.

For the sake of completeness, the following equation replaces (36) in the case that the reference curve is an isotherm instead of an adiabat. The differential equation for the isotherm is derived from

$$\frac{1}{2} P_H(V_0-V) = \Delta E_{tr} - \int_{V_0'}^{V} (P_T dV - T_0 \frac{\gamma C_v}{V}) dV + \frac{V}{\gamma} (P_H-P_T) \quad , \qquad (41)$$

where the subscript "T" indicates the isotherm. The remaining analysis proceeds by analogy with the isentropic case. The temperature of an equilibrium Hugoniot state in the mixed phase region may be calculated assuming that the reference isotherms of the low- and high-pressure phases have already been determined. As detailed by Ahrens et al. [8], two independent equations in the two component phases are derived which may be solved for the unknowns T_H and the mass fraction of material transformed to the high-pressure phase.

Experimental Shock Temperatures

As indicated in the above derivations, knowledge of the parameters of the thermal equation of state and heat capacity of a given material allow the calculation of shock temperatures for a variety of phase relationships. Conversely, experimental measurement of temperatures along the Hugoniot may be used to characterize the equation of state, beyond the pressure-volume information obtained from conventional Hugoniot measurements.

As pointed out earlier in this chapter, the measured temperature gradient along the Hugoniot provides a strong constraint on the specific heat C_v of the phase in question, while γ is not so well bounded. On the other hand, information about the magnitude and variation of the Grüneisen parameter may be derived indirectly from shock temperature measurements. The case of SiO_2 (Chapter 4) illustrates this possibility, as the configuration of phase boundaries and transition energies in the

silica system, found through Hugoniot temperature measurements, have allowed correct values of γ in the stishovite and newly identified liquid phases to be estimated. Furthermore, in cases for which γ has been previously evaluated under the assumptions of the Mie-Grüneisen equation, experimental temperatures can provide a check on the consistency of these assumptions with the actual case. Departures from ideal Mie-Grüneisen behavior may be thus detected through anomalous temperature dependence in γ, as is discussed in the case of shock temperature results for liquid H_2O (Chapter 5).

Not to be neglected is the importance of Hugoniot temperature measurements in the detection and characterization of first-order phase transformations, including polymorphic solid-solid transitions, as well as shock induced melting and freezing. The standard condition free energy difference E_{tr} between competing phases quantitatively influences the position of the measured temperature Hugoniot, and the existence of phase equilibrium boundaries can profoundly affect the qualitative nature of the observed temperature trajectories. In some cases, the temperature signature associated with the heat of transition is the only observable indication of the phase change under the difficult measurement conditions of the shock wave experiment.

The nature of shock wave experiments make the task of temperature measurement a formidable one. The short time scales involved (typically 10^{-7} seconds or less) present a problem for thermometry or thermocouple techniques which require an appreciable time to reach thermal equilibrium. Furthermore, in many cases, the presence of an <u>in situ</u> gauge for temperature measurement in the shock-compressed material can give rise to reflected shocks and rarefactions which seriously disturb the desired

state (and temperature) in the material for the length of the experiment. For these reasons, the approach to temperature measurement in high-pressure shock experiments has been predominantly through the measurement of thermal radiation.

Shock-wave investigators have long observed that transparent dielectrics shocked to sufficiently high pressures will become self-luminous in the compressed region behind the shock front. This radiation escapes through the transparent unshocked layers of the sample, and in many cases the spectrum of emitted light is continuous and characteristic of a thermal (blackbody) source. Early experiments designed to use this radiation for Hugoniot temperature determinations were performed by Kormer [9,10], using alkali halide crystal specimens. These temperature determinations were made by measuring the radiation intensity versus time at two visible wavelengths. The Kormer analysis necessarily assumed the blackbody nature of the radiation, but the results obtained were internally consistent and indicative of the validity of the optical pyrometry technique.

Considerable interest has also centered on the problem of shock temperature measurements in opaque specimens, and experimental research in this direction has been along two lines. The first has been the measurement of residual post-shock temperatures at the free surfaces of opaque samples subjected to shock loading and subsequently released to zero pressure. This work was done by Raikes [11] for a variety of metals and silicate minerals, and the degree of residual temperature rise was used to estimate indirectly the thermal nature of the shock compressed state. The second line of experiments has examined the thermal radiation from the impedance-matched interface between an opaque (metallic) sample and

a transparent "window" layer. The function of the transparent window is to allow radiation from the shocked metal layer to be detected, while retaining the sample in its elevated pressure state. This work has been described by Grover and Urtiew [12,13] and forms the basis of some of the present series of experiments, as described further in Chapter 3.

The present chapter is intended as an introduction and to provide motivation for the measurement of shock temperatures. The succeeding chapters will discuss the techniques and results coming from this research, discussing their implications both for the physics and chemistry of high-pressure shock phenomena generally, and for the properties of the specific materials studied here, including those materials which are of importance in geophysics.

REFERENCES

1. Zel'dovich, Ya. B., and Yu. P. Raizer, Physics of Shock Waves and High-Temperature Hydrodynamic Phenomena, edited by W. D. Hayes and R. F. Probstein, Academic Press, New York (1966).

2. Grüneisen, E., Handbuch der Physik, 10, 22 (1926).

3. Slater, J. C., Introduction to Chemical Physics, p. 219, McGraw-Hill, New York (1939).

4. Walsh, J. M., and R. H. Christian, Equation of state of metals from shock wave measurements, Phys. Rev., 97, 1544-1556 (1955).

5. McQueen, R. G., S. P. Marsh and J. N. Fritz, Hugoniot equation of state of twelve rocks, J. Geophys. Res., 72, 4999-5036 (1967).

6. McQueen, R. G., J. N. Fritz and S. P. Marsh, On the equation of state of stishovite, J. Geophys. Res., 68, 2319-2322 (1963).

7. Al'tshuler, L. V., Use of shock waves in high-pressure physics, Sov. Phys. Usp., 8, 52-91 (1965).

8. Ahrens, T. J., C. F. Petersen and J. T. Rosenberg, Shock compression of feldspars, J. Geophys. Res., 74, 2727-2746 (1969).

9. Kormer, S. B., M. V. Sinitsyn, G. A. Kirillov and V. D. Urlin, Experimental determination of temperature in shock-compressed NaCl and KCl and of their melting curves at pressures up to 700 kbar, Sov. Phys. JETP, 21, 689-700 (1965).

10. Kormer, S. B., Optical study of the characteristics of shock-compressed condensed dielectrics, Sov. Phys. Usp., 11, 229-254 (1968).

11. Raikes, S. A., and T. J. Ahrens, Post-shock temperatures in minerals, Geophys. J. R. Astr. Soc., 58, 717-748 (1979).

12. Urtiew, P. A., and R. Grover, Temperature deposition caused by shock interactions with material interfaces, J. Appl. Phys., 45, 140-145 (1974).

13. Grover, R., and P. A. Urtiew, Thermal relaxation at interfaces following shock compression, J. Appl. Phys., 45, 146-152 (1974).

Chapter 2

THE OPTICAL PYROMETRY TECHNIQUE IN SHOCK COMPRESSION EXPERIMENTS

Introduction

Among the principal methods of modern physics for the study of the equations of state and physical properties of materials at high pressure and temperature is the technique of dynamic compression by shock waves. Several authors [1,2] have reviewed the techniques of shock compression of condensed matter and discussed the information which may be obtained in experiments at pressures of 100 GPa or higher.

A major difficulty with the use of pressure-density-energy equation-of-state data obtained from shock wave experiments on various elements and compounds [3,4] and with understanding the thermodynamics and interatomic dynamic behavior of these materials is the general lack of knowledge of their temperatures. If the Mie-Grüneisen equation of state is assumed for a material, then its shock temperature T_H is given by the simultaneous solution of the equations which are summarized in the preceding chapter. As discussed there, the final temperature of the shock state along the Hugoniot curve of a given material is controlled by the specific heat and Grüneisen parameter of that material as well as by the energetics of any shock-induced phase transformations that may occur. An experimental measurement of T_H can therefore provide constraints on C_v and γ, both of which are essential parameters in thermal equations of state.

Such measurements aid in an understanding of lattice anharmonicity [5], melting [6,7], and other aspects of vibrational lattice dynamics.

The present chapter describes a fast (~5 ns) time response optical pyrometer system which has been applied to the measurement of shock temperatures in transparent materials to pressures of 175 GPa and over the temperature range of 4000-8000 K. The pyrometer is designed to be used in conjunction with a two-stage light-gas gun [8], a device which is capable of accelerating projectiles to speeds of up to ~7 km/s. Strong shock waves are driven into sample materials upon impact of these high-speed projectiles in vacuums of 10^{-2} Torr.

Because typical shock experiments near 100 GPa pressure are less than 10^{-6} s in duration, the only practical means of temperature determination is a time-resolved measurement of the thermal radiation emitted by the sample. Use of optics and solid-state detectors in the visible wavelength range permit temperature measurements between approximately 2000 K and 10^4 K. These limits are determined by the lower sensitivity limit of the silicon detectors and by the increasing insensitivity of the slope of the visible Planck radiation spectrum to changes in temperature, respectively. Pioneering work in the measurement of shock temperatures by optical techniques was done by Kormer [6,7]. The present work incorporates substantial improvements in time resolution and spectral coverage over previous studies and so allows a wider range of materials and pressures to be studied.

Light-Gas Gun Experiments

The present series of shock wave experiments has been carried out

jointly with the collaboration and support of the Lawrence Livermore Laboratory shock physics group, directed by W. J. Nellis. The principal apparatus for the generation and characterization of shock waves in the 100 GPa pressure range is the Livermore two-stage light-gas gun.

The design and principles of operation of the two-stage gun are detailed by Jones et al. [8], and the following is a general description of the technique. Figure 2-1 is a schematic diagram of the operation of a light-gas gun. The overall length of this device is approximately 23 meters, and acceleration of the projectile to the desired velocity is achieved in two stages.

In the first stage, expanding combustion products from the burning of approximately 1 kg of gunpowder accelerate a massive (~7 kg) piston down the length of the pump tube. The pump tube is initially filled with hydrogen gas at a pressure of approximately 10 bars, and as the piston moves in the pump tube, this gas is rapidly adiabatically compressed. At a fixed gas pressure near 1400 bars, a rupture valve opens, initiating the second stage.

A 20 g mass projectile of 28 mm diameter is accelerated through the length of a smooth bore launch tube (or barrel), reaching a final velocity of up to 7 km/s, depending upon the initial explosive mass. The projectile consists of a flat metallic impactor plate, molded into the leading face of a lightweight plastic sabot which acts as a gas seal. The impact of this plate with a planar target induces a flat shock front in the target as well as the flyer plate. The lateral dimensions of the uniform one-dimensional flow are determined by the width of the flyer plate (~25 mm) and the duration of pressure application is limited by the finite thickness

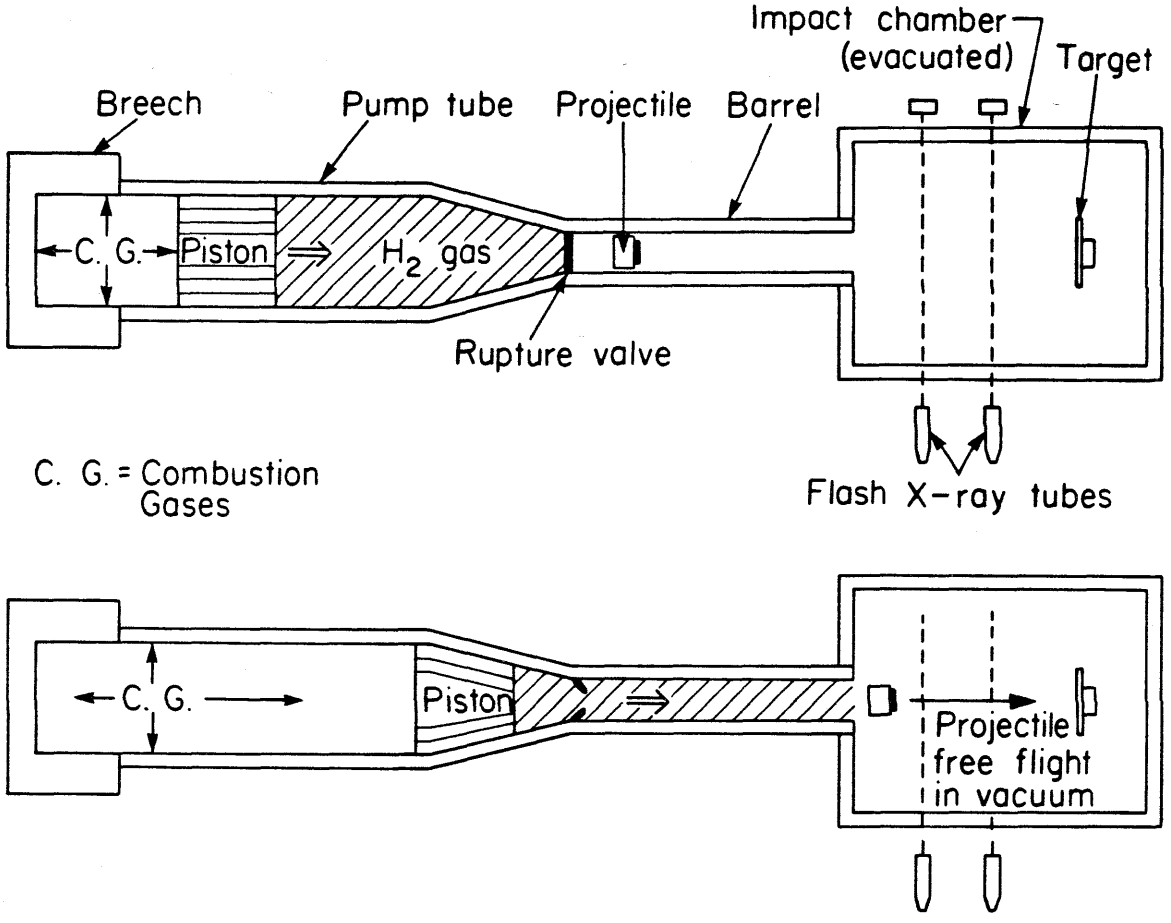

Figure 2-1. Schematic operation of two-stage light-gas gun. Expanding gases from burning propellant drives piston, compressing hydrogen gas. Rupture valve opens, accelerating projectile through the barrel. Projectile velocity is determined via timing of flash x-ray firings.

of the plate.

The diagnostic measurements in such an experiment include measurement of the projectile impact velocity and the shock velocities or other physical quantities of interest which pertain to the target. Projectile velocity is measurable to an absolute accuracy of ~0.1%, utilizing flash x-ray radiography of the projectile in flight. The time between x-ray "snapshots" of the flyer at positions typically a few tens of centimeters apart are accurately measured in order to make the velocity determination.

In the course of conventional Hugoniot equation-of-state experiments, the shock velocity is measured as the wave passes through the target. When the Hugoniot equation of state of the impactor material is already known, measurement of the shock velocity u_s and the flyer velocity are sufficient to determine the particle velocity u_p, and thus the complete Hugoniot P-V-E state. This is accomplished using the impedance match method described by Al'tshuler [2].

The present set of experiments has been designed specifically to determine the temperature of the target material under shock compression, assuming that the Hugoniot equation of state of the studied material is already known from previous experiments. With the sample Hugoniot known, all that is required to characterize the pressure state in the sample is a measurement of the impactor velocity. This provides the pressure scale for each measured Hugoniot temperature point obtained in a given shot. Additionally, an unexpected bonus of information is often obtainable from the shock temperature experiments. In many materials, the time-resolved temperature records provide an accurate measure of the time of shock wave transit through the sample, and thus they allow an independent check on the shock velocity

and Hugoniot of the sample. This technique is described in the discussion of results from SiO_2 samples (Chapter 4), as it proved to be particularly useful in that instance.

In other experiments, investigators have undertaken measurements of many physical properties including electrical conductivity [9], x-ray diffraction [10,11], optical characteristics [7,12] and others during the period of shock compression lasting a few hundred nanoseconds. The following is a description of a newly developed multiwavelength pyrometry technique for the measurement of shock temperatures in light-gas gun driven experiments.

Pyrometer Design

The pyrometer design consists of an optical subsystem for light collection and spectral filtering, and a detection subsystem consisting of the photodetectors and associated recording electronics.

As shown in Figure 2-2, the optics are located outside the impact tank, protected by polycarbonate windows of 10 mm thickness. Six channels view the sample in a two-by-three rectangular array, with a window center-to-center distance of 9.2 cm. Each of the optical channels has a 5-cm-diam achromatic objective lens of 51-cm focal length which provides parallel light to the filter which follows in the optical path. Each filter is a narrow-band interference filter with approximately 50% peak intensity transmission and ~9-nm half-height bandwidth. The six channels span the visible and near infrared spectrum, with filters centered near wavelengths of 450, 500, 550, 600, 650, and 800 nm. Finally, an achromat of 19-cm focal length in each channel provides a filtered image of the target source at the sensitive surface of the respective photodetector.

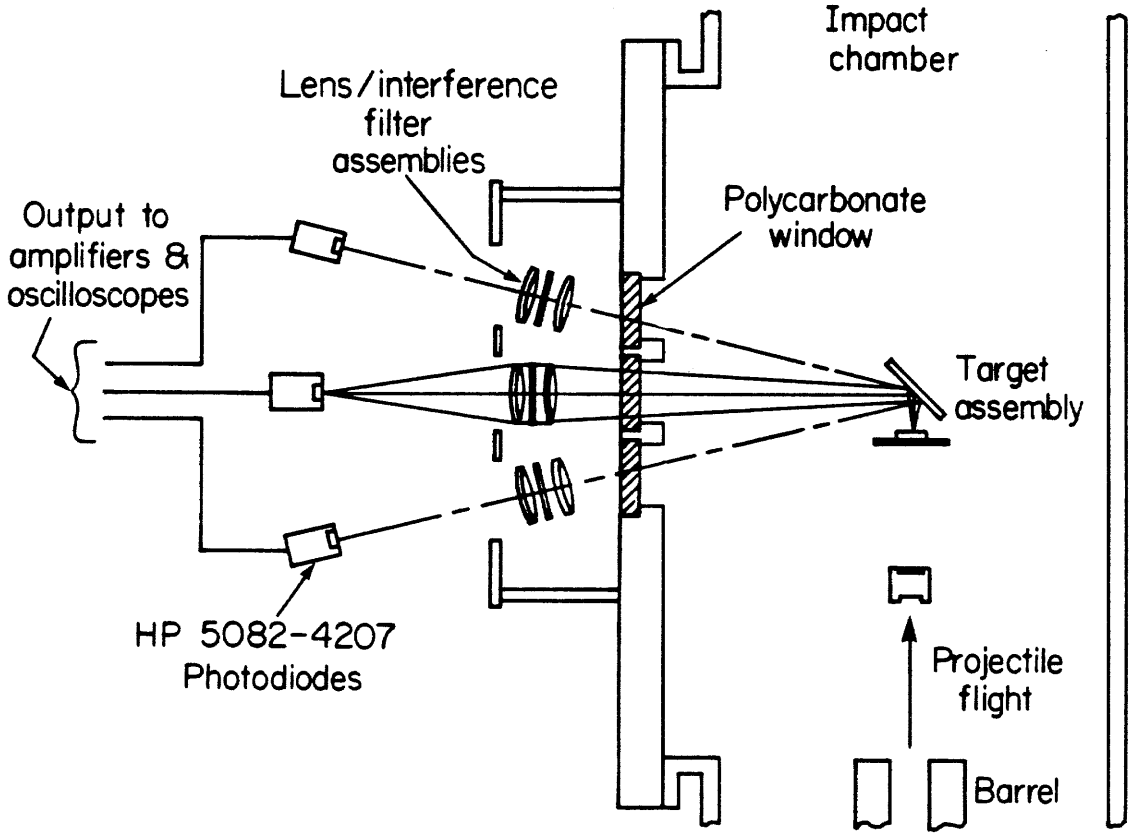

Figure 2-2. Schematic design of pyrometer. Optical components exterior to evacuated impact chamber deliver filtered images of the target to photodetectors.

The basic detector consists of a Hewlett-Packard 5082-4207 PIN silicon photodiode, which is reverse biased at 10 V. The diode has an active area approximately 1 mm in diameter and produces a nominal photocurrent of 0.5 mA/mW for radiation of wavelength 770 nm. In the experimental configuration, the detector has a rated speed of response of about 1 ns. The detector is sensitive to light of wavelengths between about 400 and 1000 nm. Since the optical system produces an image of the sample which is several millimeters wide at the detector, the photodiode output current is proportional to the power per unit area radiated by the sample. It is assumed that each detector views the same region of the sample and that the radiation flux is constant across the detected region. The validity of this latter assumption has been checked in the case of crystalline quartz (SiO_2) as the investigated sample. The details of this work are discussed in Chapter 4.

As shown in the schematic diagram of Figure 2-3, the photodiodes in each channel act as current sources driving 50 Ω impedance low-loss transmission lines. The signals are recorded on high-speed oscilloscopes, in this case Tektronix 585 and 7903 models. In experiments with small expected signals (less than a few mV), intermediate stages of amplification are employed. The Hewlett-Packard 8447 A wide-band amplifier has been used for this purpose. The recording oscilloscopes are triggered at signal onset by the impact-generated shock wave closing self-shorting electrical contacts [8].

Figure 2-4 illustrates the layout of a typical target in a shock pyrometry experiment. An expendable aluminized front-surface mirror mounted behind the sample and base plate reflects radiation to the optical

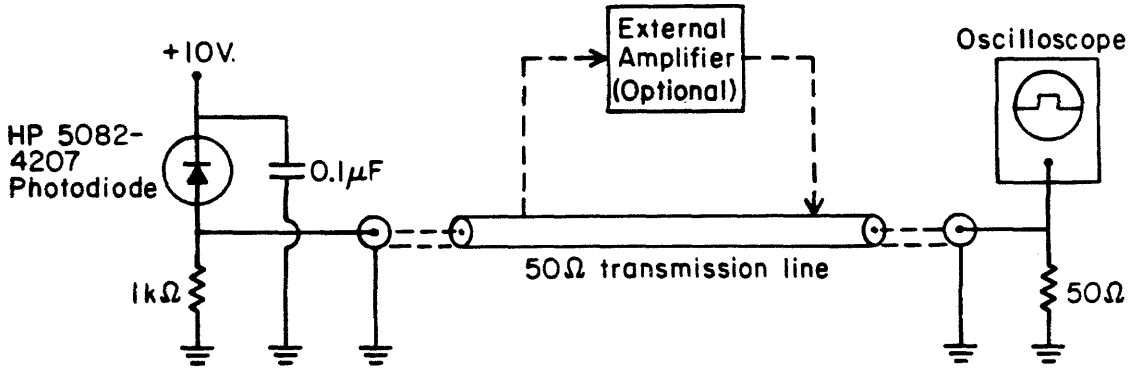

Figure 2-3. Detector circuit for typical pyrometer channel. Remote recording oscilloscopes receive signals via 50 Ω cable with ~200 ns delay.

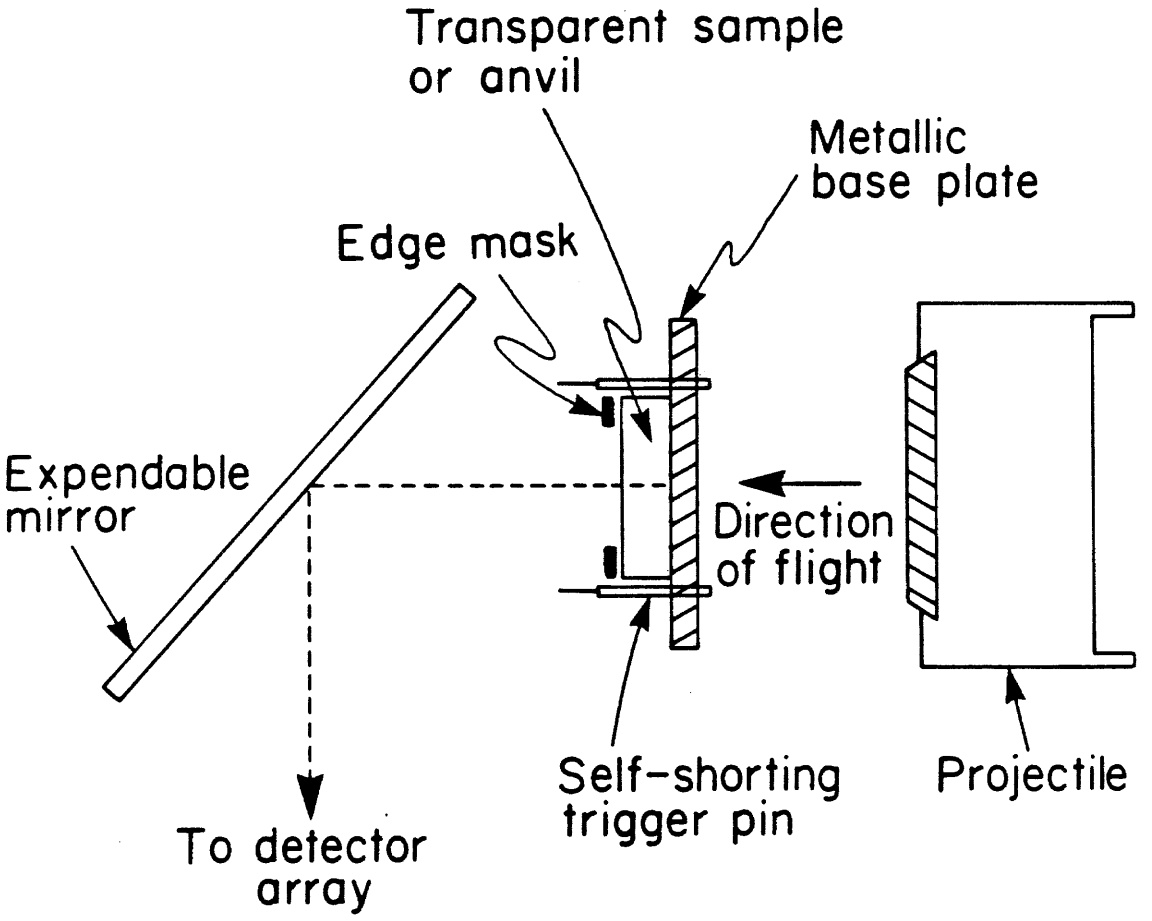

Figure 2-4. Configuration of target in shock pyrometry experiment. Radiation from shock compressed material emerges from rear surface and enters pyrometer optics.

channels. In the case that the investigated sample is a liquid, the target is modified to include a containment chamber and a radiation window. Alignment and focusing of the optical and detector systems prior to an experiment is achieved with the target in place. A compact light source is affixed to the target rear surface and focusing is accomplished with the interference filters removed. Positioning of the detectors within ~1 mm of the focal plane provides a detected flux reproducible to a few tenths of a percent.

Calibration of the pyrometer requires a determination of the sensitivity of each channel in its actual geometric configuration. A calibrated tungsten ribbon spectral radiance source is used in place of the target. The voltage output in this dc calibration is then used to find the voltage response for a given sample spectral radiance in power per unit area and solid angle per unit spectral bandwidth. Assuming that the detector efficiency is the same for transient and static illumination and that its intensity response is linear, the voltages measured during a shot may be interpreted directly in terms of radiation output. The calibration lamp used is a General Electric commercial type having a tungsten SR-8A filament. The lamp is calibrated by the Eppley Laboratory, Inc., Newport, RI, against National Bureau of Standards calibrated standard sources. Figure 2-5 shows the signals expected for a blackbody source as a function of temperature, as measured for two of the actual pyrometer channels. The uncertainty in radiance calibration by the tungsten ribbon standard technique is approximately 2%. More detailed descriptions of the calibration equipment and procedures as well as a documentation of the operational details of the present system appear in Appendix I.

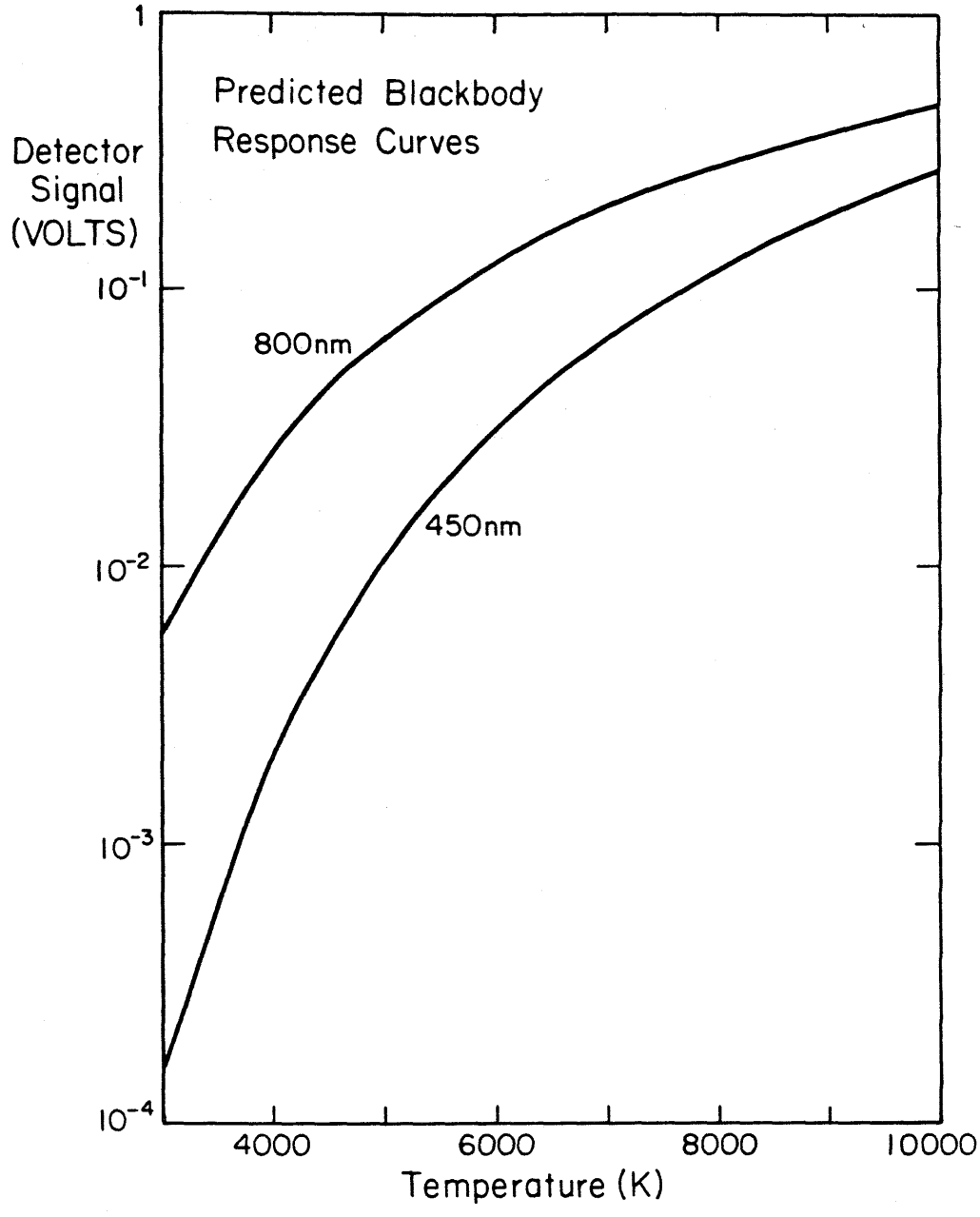

Figure 2-5. Pyrometer predicted response to ideal blackbody source. Wavelength channels 450 nm and 800 nm are illustrated.

Experimental Results and Data Treatment

The pyrometer has been primarily used to determine shock temperatures in initially transparent materials. This is because radiation from the heated material behind the shock front can escape through the unshocked transparent material, allowing the light to be detected during shock transit through the sample, rather than only at the instant of shock arrival at the free surface.

The materials which have been studied to date by this technique include NaCl, H_2O, SiO_2, and Mg_2SiO_4. NaCl is a material whose shock temperature has been the subject of earlier work by Kormer [6,7] and it provides a point reference from which to extend these studies. SiO_2 and Mg_2SiO_4 (quartz and forsterite) are minerals whose geophysical importance makes the characterization of their thermal equations of state significant.

Figure 2-6 shows a typical experimental oscilloscope record from an experiment with quartz. The recorded light intensity rises abruptly as the shock front enters the sample, and subsequently rises more gradually, approaching an asymptotic value. Upon arrival of the shock front at the sample free surface, the recorded intensity immediately relaxes to a value characteristic of the residual zero-pressure state of the sample. Figure 2-6 presents a typical experimental record; however, different materials at various Hugoniot pressures have shown different detailed behavior. Some materials do not show the gradual intensity rise, but rather exhibit constant brightness throughout the shock transit. In many experiments, an initial brief flash is observed as an overshoot in the records and is believed to be an effect of interfacial gaps between the sample and base plate.

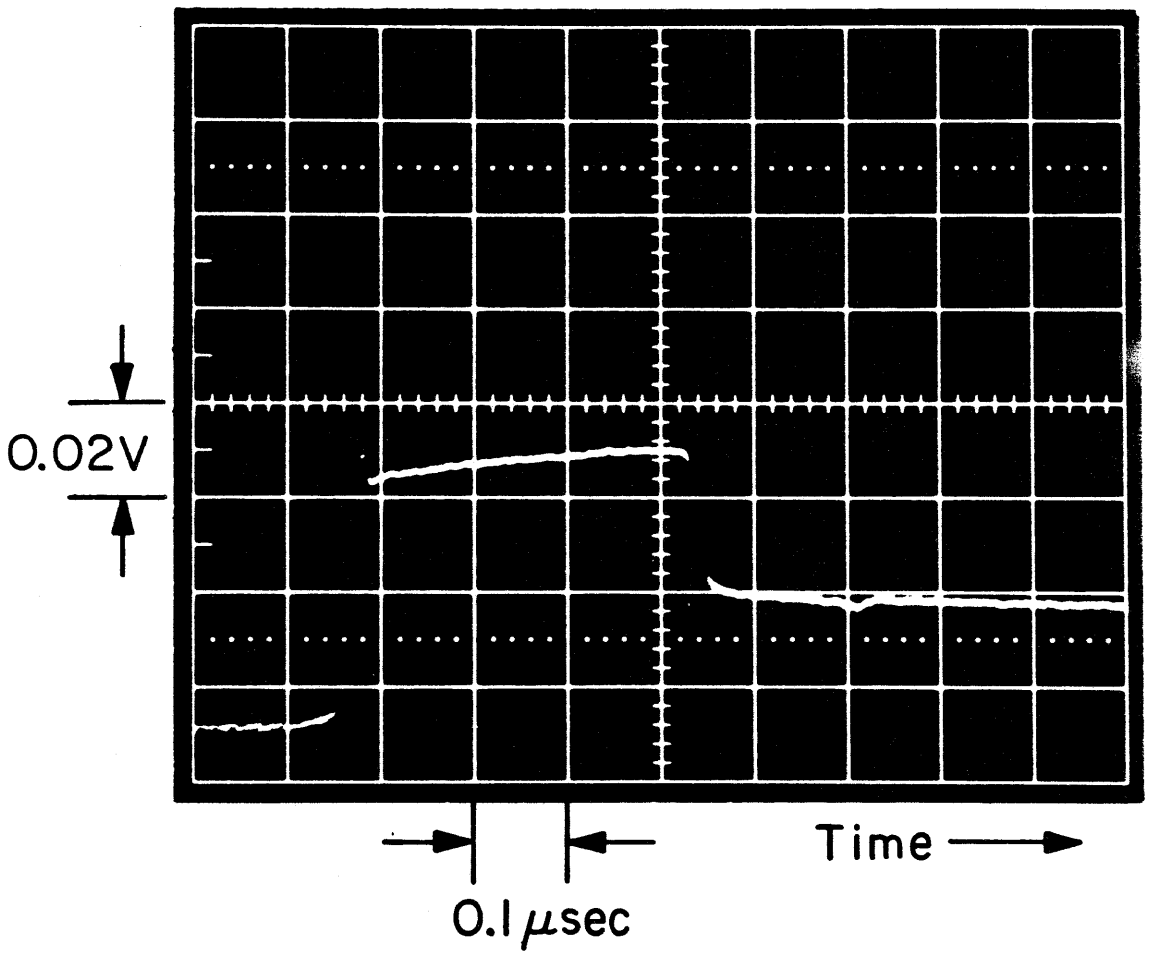

Figure 2-6. Typical oscilloscope record from one channel in shock pyrometry experiment. Example is from a shot on fused quartz at ~80 GPa pressure.

Considerable interest centers on the origin and nature of the radiation observed in these experiments, since its interpretation in terms of the Hugoniot temperature hinges upon questions of thermal equilibrium and emissivity. As the observations in the following discussions suggest, the measured radiation does indeed appear to display the intensity and spectrum of a thermal radiator with a large emissivity (i.e., nearly a blackbody). This raises the problem of explaining how a material which is initially a transparent insulator abruptly changes character, becoming an opaque blackbody radiator. The solution to this problem may be related to the very short rise and fall times observed for the shock-induced luminescence.

Apparently, the abrupt onset and shutoff of this radiation can be explained if the light originates in a very thin layer of material coincident with the shock front or immediately behind it. If the shock front represents the site of copious strain-induced lattice defects, this represents a possible source of conduction band electrons and the observed optical opacity. Theoretical arguments given in the Chapter 4 discussion of SiO_2 and Mg_2SiO_4 results suggest that under most circumstances, the time required for this defect ionization and thermal equilibration to occur is long enough that the radiation temperature does accurately reflect the final Hugoniot state of the compressed lattice. Exceptions to this will occur if longer time scale changes, such as those related to a shock-induced phase transition, take place behind the shock front. Such relaxation effects related to a phase change (fusion) have been measured in SiO_2, and further discussion of this phenomenon is deferred to Chapter 4. For the majority of cases investigated here, the assumption that the

measured radiative temperature is identical with T_H, the Hugoniot state temperature seems justified, at least within the accuracy of the measurement.

Interpretation of the pyrometer signals in terms of temperature requires comparison of the measured values of spectral radiance with a thermal radiation spectrum. At a given wavelength λ and temperature T, the spectral radiance of a blackbody is given by the Planck radiation formula,

$$N_\lambda = C_1\lambda^{-5}(e^{C_2/\lambda T} - 1)^{-1}, \qquad (1)$$

where $C_1 = 1.191 \times 10^{-16}$ W m^2/sr and $C_2 = 1.439 \times 10^{-2}$ m K. A real source which differs from the ideal blackbody case has its spectral radiance reduced by a factor $\varepsilon(\lambda)$, the emissivity, which may depend upon the bulk properties of the radiating material and its surface properties.

Given the measured values of N_λ at six wavelengths in an experiment, the emissivity and temperature may be simultaneously varied to obtain the best fit of equation (1) to the data. In practice, an emissivity which is constant or linearly varying with wavelength is used. The emissivity is then varied to minimize the sum of the squares of deviations in temperatures calculated for each channel from the mean temperature of all channels.

Figure 2-7 shows the results obtained for a SiO_2 crystal experiment. The measured spectral radiance points are shown along with a Planck radiation curve fit. The curve shown is for a temperature of 4625 K and a constant emissivity of 0.68. This fit has uncertainties of approximately 2% in temperature and 7% in emissivity. Temperature determinations above ~6000 K yield less well constrained solutions because of the relative insensitivity of the visible spectrum shape to temperature in this region.

In summary, this pyrometry technique which has been applied to shock compression experiments represents a potentially valuable new tool for

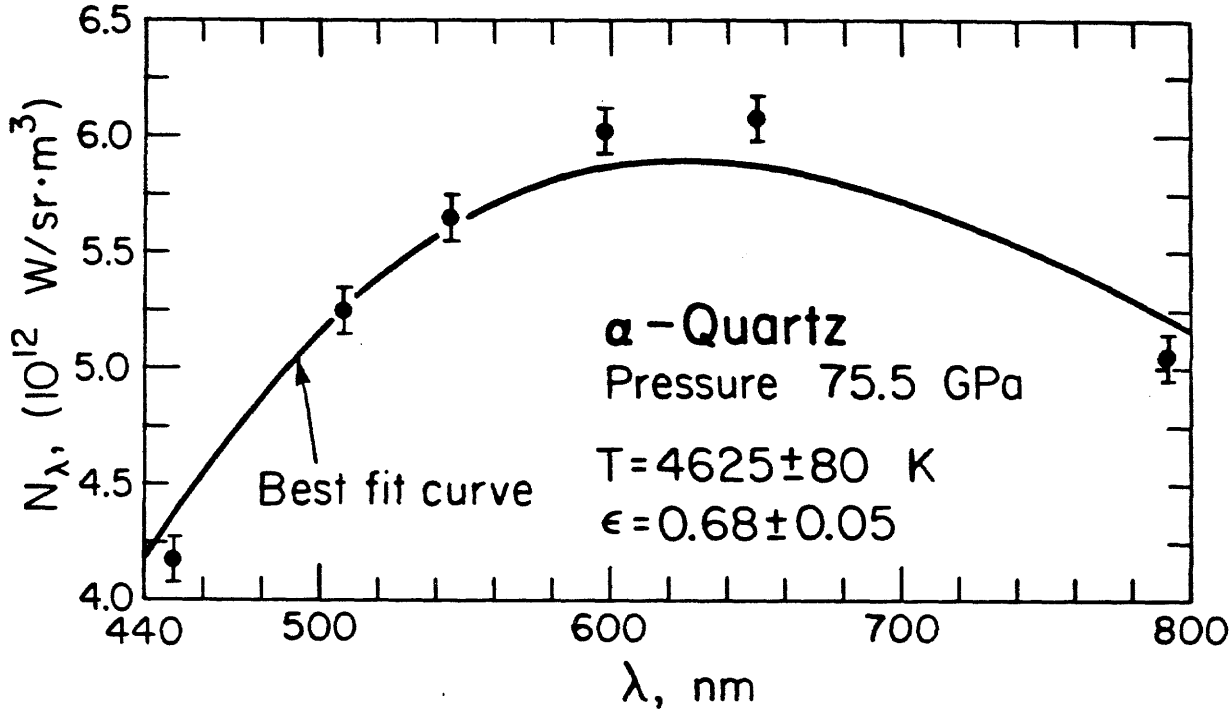

Figure 2-7. Experimental spectral radiance data for a shot on crystalline SiO_2. Blackbody fit shown with best fit temperature and emissivity.

the exploration of high pressure shock wave equations of state. The succeeding chapters describe and discuss the results to date which have come from this work and are illustrative of results that can be expected in the future as this technique finds more widespread application.

REFERENCES

1. Ahrens, T. J., Dynamic compression of earth materials, Science, 207, 1035-1041 (1980).

2. Al'tshuler, L. V., Use of shock waves in high-pressure physics, Sov. Phys. Usp., 8, 52-91 (1965).

3. Walsh, J. M., M. H. Rice, R. G. McQueen and F. L. Yarger, Shock-wave compressions of twenty-seven metals. Equations of state of metals, Phys. Rev., 108, 196-216 (1957).

4. McQueen, R. G., S. P. Marsh and J. N. Fritz, Hugoniot equation of state of twelve rocks, J. Geophys. Res., 72, 4999-5036 (1967).

5. Barron, T. H. K., in Lattice Dynamics, edited by R. F. Wallis (Pergamon, New York, 1965), p. 247.

6. Kormer, S. B., M. V. Sinitsyn, G. A. Kirillov and V. D. Urlin, Experimental determination of temperature in shock-compressed NaCl and KCl and of their melting curves at pressures up to 700 kbar, Sov. Phys. JETP, 21, 689-700 (1965).

7. Kormer, S. B., Optical study of the characteristics of shock-compressed condensed dielectrics, Sov. Phys. Usp., 11, 229-254 (1968).

8. Jones, A. H., W. M. Isbell and C. J. Maiden, Measurement of the very high pressure properties of materials using a light-gas gun, J. Appl. Phys., 37, 3493-3499 (1966).

9. Mitchell, A. C., M. I. Kovel, W. J. Nellis and R. N. Keeler, Electrical conductivity of shocked water and ammonia, preprint UCRL-82126, Lawrence Livermore Laboratory (1979).

10. Johnson, Q., A. Mitchell, R. N. Keeler and L. Evans, X-ray diffraction during shock-wave compression, Phys. Rev. Lett., 25, 1099-1101 (1970).

11. Johnson, Q., and A. Mitchell, First x-ray diffraction evidence for a phase transition during shock-wave compression, Phys. Rev. Lett., 29, 1369-1371 (1972).

12. Urtiew, P. A., Effect of shock loading on transparency of sapphire crystals, J. Appl. Phys., 45, 3490-3493 (1974).

Chapter 3

RESULTS AND APPLICABILITY OF SHOCK PYROMETRY EXPERIMENTS

Introduction

During the course of this research in experimental shock temperatures, several different materials were examined, both to learn about the thermal equations of state of a wide range of solids and liquids and to investigate the range of applicability of the pyrometry technique. The current chapter presents the results from a selection of these experiments. The initial trials of the shock pyrometer were performed using NaCl (sodium chloride) crystal samples, building upon the groundwork provided by the earlier work of Kormer et al. [1,2].

Simultaneously with this effort to measure Hugoniot temperatures in a simple ionic solid, experiments were considered to make such measurements in silicate and oxide minerals of importance in problems of solid-earth geophysics. The phenomenology of these experiments is surveyed in this chapter; however, the detailed interpretation of the measured shock temperatures in SiO_2 and Mg_2SiO_4 is the subject of a separate chapter (Chapter 4).

Finally, a limited amount of experimental work has been done toward the goal of shock temperature measurements in metals. This problem offers considerable challenge to the optical pyrometry technique, and the current progress toward its solution is discussed here.

NaCl Shock Temperatures

Shock pyrometry experiments were carried out on NaCl samples using the Lawrence Livermore Laboratory light-gas gun in the experimental configuration described in Chapter 2. The sample material consisted of synthetic sodium chloride single crystals, cut and polished as discs 4 mm in thickness and 19 mm in diameter. These infrared-grade crystals were supplied by the Harshaw Chemical Co., Solon, Ohio. In all the experiments, the crystal sample was mounted on a tantalum standard base plate 2 mm in thickness, and this target assembly was impacted by a 2 mm thick tantalum flyer plate.

Table 3-1 presents the results of five pyrometry shots carried out on NaCl between shock pressures of approximately 70 and 105 GPa. The reported shock pressures were obtained via the impedance match method (Al'tshuler [3]). The Hugoniot equations of state of NaCl and the tantalum standard were assumed known, so that a measurement of impactor velocity determined the pressure in each experiment. As determined by Mitchell et al. [4], the Ta Hugoniot (initial density 16.66 g/cm^3) is described between 30 and 430 GPa by the shock velocity-particle velocity relation,

$$u_s = (1.298 \pm .012)\, u_p + 3.313 \pm .025 \text{ km/s}. \qquad (1)$$

The reference for Hugoniot data on NaCl was the Livermore shock wave data compilation [5]. Table 3-1 also contains the best fit temperature and emissivity solutions obtained from the pyrometer spectral radiance measurements. Here and in the cases of other Hugoniot temperatures reported in this thesis, only the reduced temperature and emissivity values are given. For completeness, a collection of the unreduced spectral radiance data appears in Appendix II, cataloged by material.

Table 3-1

NaCl Hugoniot Temperature Data

Ta Impactor Velocity (km/s)	Shock Pressure (GPa)	Shock Temperature (K)	Effective Emissivity
4.80 ± .01	72.5 ± 1.0	4440 ± 150	.67 ± .07
4.90 ± .01	74.5 ± 1.0	4650 ± 150	.85 ± .08
5.5 ± 0.3	87 ± 5	5750 ± 200[a]	~1
5.80 ± .01	95.0 ± 1.5	6850 ± 300	.73 ± .14
6.18 ± .01	104.5 ± 1.0	7850 ± 250	.91 ± .08

[a]Blackbody temperature based upon three wavelength intensity measurements.

Figure 3-1 gives a pressure-temperature plot of the NaCl Hugoniot data, along with the reported experiments and interpolation of Kormer [1]. It is evident that the data from the present work are largely consistent with the results of Kormer, joining smoothly with it in the pressure region of overlap near 70-80 GPa. At relatively high pressures, Kormer's implicit assumption of blackbody emissivity for the sample seems fairly reasonable, although at the lower end of investigated pressures, the emissivity indicated by this work is significantly less than unity. This decline in emissivity accounts for the somewhat lower temperatures obtained by Kormer through the blackbody assumption compared with the present work near 70 GPa.

Kormer's temperature points were obtained from light intensity recordings at two visible wavelengths (instead of six in the present experiments). These intensity values, measured remotely by photomultipliers in high-explosive-driven shock experiments, were converted into blackbody temperatures assuming the emissivity of an opaque layer equal to unity. Separate temperature determinations were obtained from the red (625 nm) and blue (478 nm) temperatures, and vertical bars are used to indicate the range between these two values in Figure 3-1. The agreement between these values was taken by Kormer as evidence that the blackbody assumption was justified, although it may be noted in retrospect that the fact that the blue temperatures are always several hundred degrees higher than the red temperatures reported indicates a systematic overestimate of the emissivity.

A second but related issue in the comparison of the current work with that of Kormer pertains to the time dependence of the measured light. Figure 3-2a shows an oscilloscope record of detected light intensity from an NaCl shot in the current series, at a pressure of 72.5 GPa. This

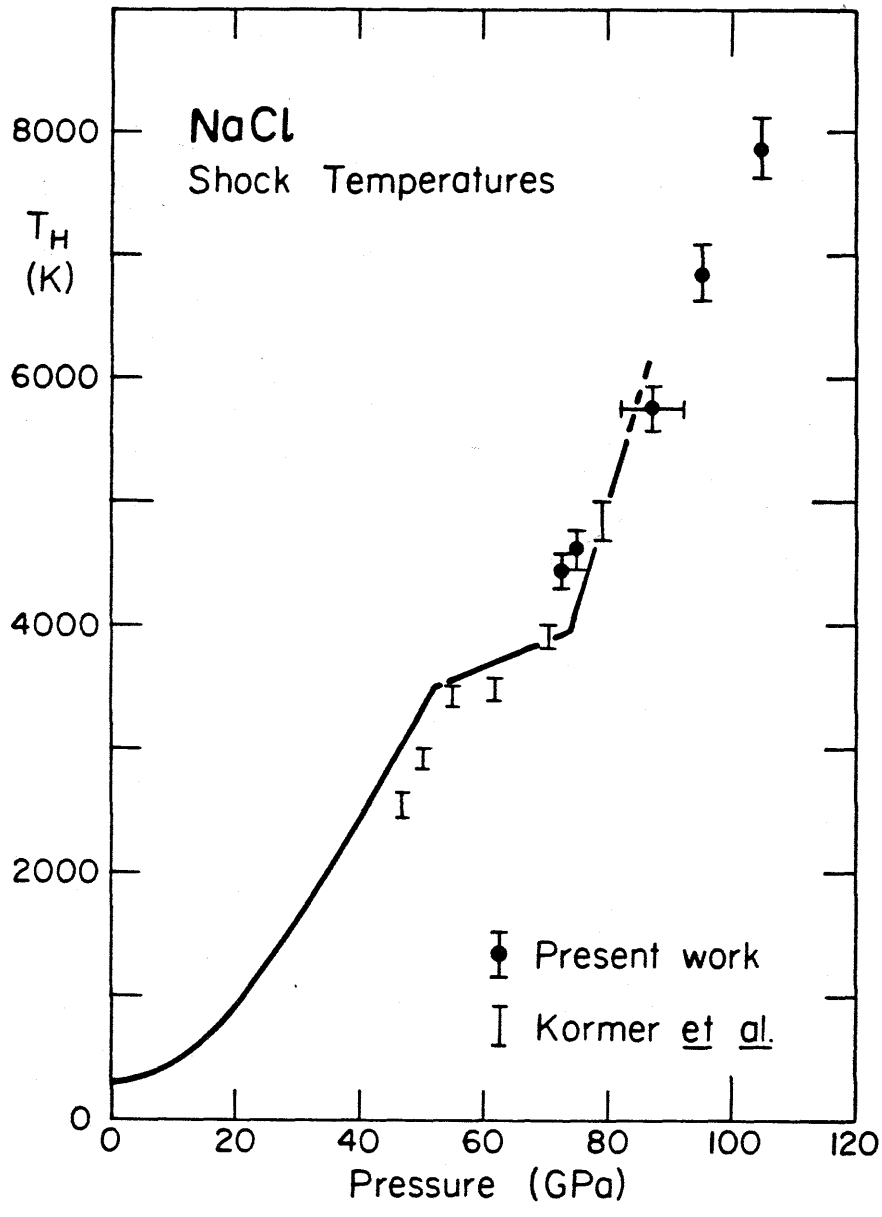

Figure 3-1. Experimental Hugoniot temperatures versus pressure in single crystal NaCl. Solid points from present investigation. Vertical bars are measurements by Kormer [1], with upper value at λ = 478 nm (blue) and lower value at λ = 625 nm (red). Solid line shows Kormer's calculation, with melting assumed.

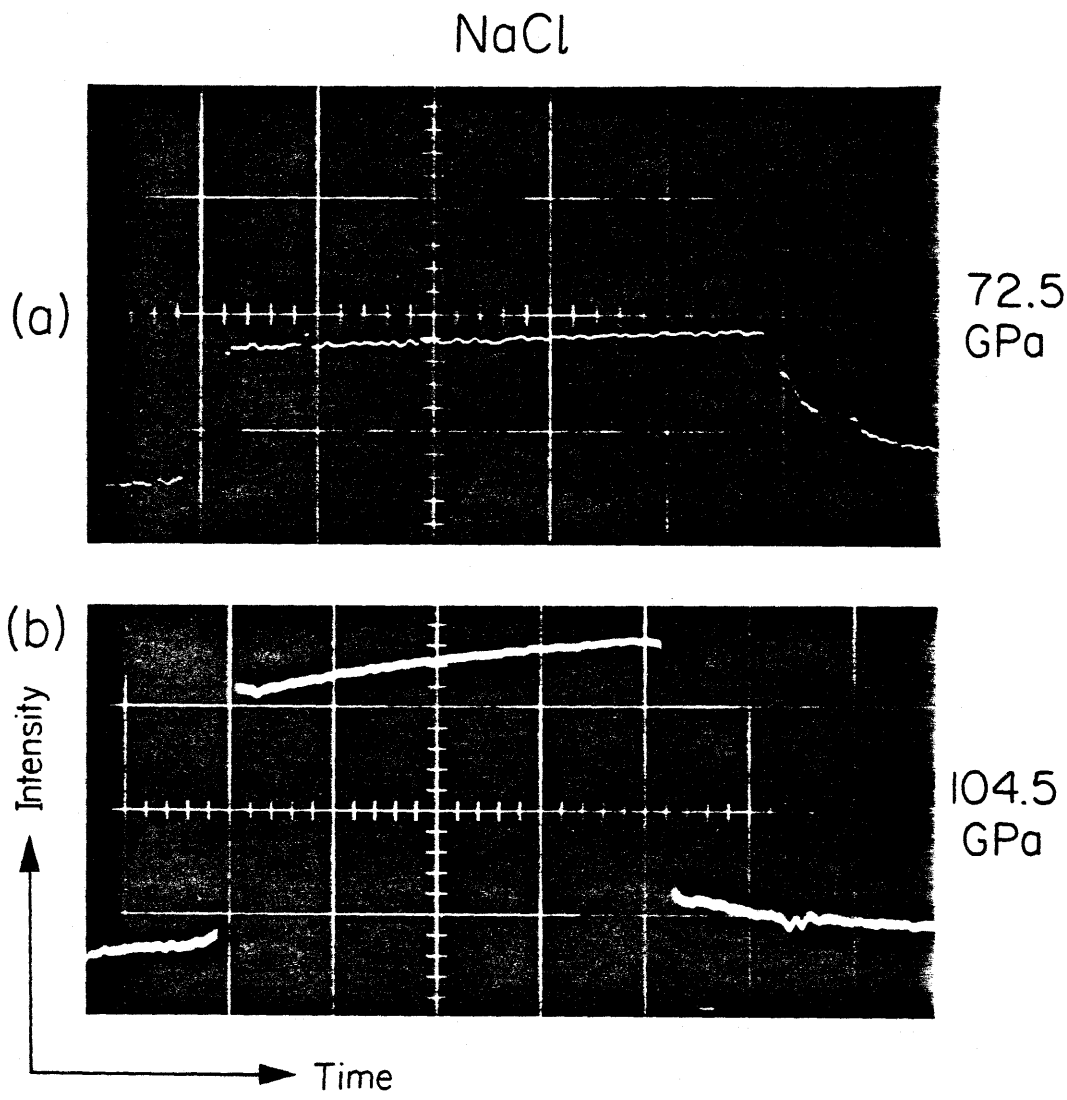

Figure 3-2. Oscilloscope records of thermal radiation intensity (vertical dimension) in NaCl experiments. (a), Hugoniot pressure 72.5 GPa. (b), Hugoniot pressure 104.5 GPa. Horizontal time scale, 100 ns per division both records. Note increased time dependence at higher pressure. Both records from 650 nm wavelength channel.

overlaps the pressure range investigated by Kormer, and the recorded intensity history is quite similar in its time dependence to that recorded for other materials, as illustrated in the previous and succeeding chapters. This result is in apparent contradiction with the reported results of Kormer in the same range. While the present studies indicate that the rise of shock-induced luminescence occurs in a time comparable or shorter than the instrumental rise time of ~5 ns, Kormer's earlier work indicated that the radiation required as long as a few hundred nanoseconds to reach full intensity. Kormer interpreted this long rise time as the period required for an opaque layer of shocked material to accumulate behind the shock front. In all of the NaCl experiments reported by Kormer, the light intensity did not reach a "plateau" value during the duration of shock propagation, and a correction in the temperature for this apparent emissivity effect was applied.

The present work strongly suggests that Kormer's observed rise times were either instrumental or due to peculiarities of the shock driving system, at least at the pressures overlapping those investigated here. The suggestion is strong that in the present experiments an effectively opaque radiating layer is achieved near the shock front, within a layer probably no thicker than about 30 μm, and possibly much thinner. In any case, it appears that the Kormer shock temperature points reported at lower pressures may underestimate the true shock temperatures. This possibility has a bearing on Kormer's proposed identification of the NaCl melting line.

The indicated region of slower temperature increase between approximately 55 and 70 GPa along the Hugoniot was taken by Kormer as an indication of shock-induced melting. In this picture, the region of shallow

temperature slope represents the region of mixed phases in which solid and liquid coexist and therefore defines the phase coexistence line in the P-T plane. While the current experiments do not confirm this result, a definitive answer to the problem should await further experiments utilizing the improved pyrometry technique. It is interesting to note that in addition to this apparent melting behavior in NaCl, Kormer reports the same results in experiments on KCl, KBr, and CsBr, with the apparent melting occurring at much the same temperature, near 4000 K in each of these materials. In addition, Kormer finds evidence for a change in slope of the u_s-u_p Hugoniot data for NaCl and KCl which correlates with the inferred transition.

While the details of the NaCl temperature Hugoniot influence the inferred melting temperature of that particular material, the issue of shock radiation rise times and emissivities has importance for the interpretation of all shock temperature experiments. Kormer [2] discusses the problem of equilibrium between free electrons and the crystal lattice in the vicinity of the shock front. Very high pressure experiments discussed by Kormer show that at large shock amplitudes corresponding to Hugoniot temperatures higher than ~7000 K, the observed brightness temperature of the shock front reaches a "saturation level," failing to rise further with increasing shock pressure as expected. This behavior in ionic crystals is attributed to screening of the lattice equilibrium temperature by a superimposed layer of shock-ionized free electrons which have insufficient time to reach equilibrium with the lattice.

In Kormer's view, while phonon-phonon relaxation times and the times for lattice thermal equilibrium are as short as 10^{-12}-10^{-13} seconds, free electrons ionized from the valence band by shock passage require a longer

time to acquire the lattice temperature in appreciable concentrations. In this model, at sufficiently high pressures an opaque layer of electrons at a low temperature not characteristic of the lattice may lag a few nanoseconds behind the shock front, screening radiation from layers in thermal equilibrium immediately behind. Since it is expected that the electron temperature of a fixed population of ionized electrons should reach thermal equilibrium within 10^{-9} s or so, this screening mechanism depends upon the ability of the shock to produce rapidly a dense concentration of free electrons, a process which it is reasonable to suggest depends upon large shock amplitudes. It is therefore important to view shock temperature measurements at high pressures with caution, and a criterion would be useful for judging whether the measured temperature is indeed characteristic of the lattice phonon value.

Figure 3-2a indicates that at lower pressures, the observed light intensity and temperature in NaCl rise abruptly to a level that remains nearly constant throughout the shock transit. As the shock amplitude is increased to ever higher pressures, however, an increasingly noticeable time dependence appears in the records. The light intensity is observed to rise slowly during shock propagation, apparently approaching an asymptotic value. Figure 3-2b illustrates the outcome of an experiment at 104.5 GPa pressure, just below the onset of temperature "saturation" reported by Kormer. The time dependence is becoming more pronounced at this high pressure and may be taken as a signal of the beginning of electron screening at the shock front.

It is interesting to note that an exactly analogous result has been obtained in the present work on H_2O and SiO_2, with the effect most

pronounced in the highest temperature shots on fused quartz (T_H approaching 7000 K). This coincides with a pressure region in which an anomalously high heat capacity is apparently otherwise required to explain the observed SiO_2 shock temperatures (Chapter 4). The present six-wavelength pyrometry method has verified that in such cases, the observed intensity rise represents a rise in the effective temperature, and not simply an increase in the emissivity of a source of constant temperature. Such observations may be taken as support of the view that temperature signals with strong time dependence signal the departure of observed temperatures from the true Hugoniot values, while the constant intensities recorded at more modest pressures faithfully reflect the lattice temperature.

In summary of the present work on NaCl, it is evident that the general agreement with the results of Kormer shows that pyrometric measurement of shock temperatures to moderately high pressures is practical. The disagreement with Kormer's conclusions regarding the opacity and absorption length in material behind the shock front remains unresolved, as does unequivocal confirmation of the melting observation. Future investigations should clarify these points by extending the range of pressures investigated with the new six-wavelength high-speed method to lower values. In the case of NaCl, it may be practical to use the present technique at pressures as low as 50 GPa, thus confirming or refuting the melting observation. Also, extension of this work to other alkali halides such as KCl would be extremely useful. From a standpoint of work completed to date, the conclusions drawn from the NaCl work allow us to proceed with interpretation of similar experiments in other materials of interest.

Observations in Other Dielectric Solids

Among the solids whose thermal equations of state at high pressures are of interest are silicate and oxide minerals which in general display larger incompressibilities than the ionic solids whose study is described above. As a result of this incompressibility, these solids characteristically reach lower temperatures at a given Hugoniot pressure than the alkali halides. For this reason, the radiation screening associated with high temperatures is apparently not a factor, but limitations on the shock pyrometry technique become apparent when temperatures are too low.

Three such minerals whose radiative behaviors at high shock pressure have been studied are Mg_2SiO_4 (forsterite), MgO (periclase) and Al_2O_3 (sapphire). In the case of forsterite, shock pressures between ~128 and 175 GPa have been investigated, with two types of results obtained. For three shots at the highest pressures (between 150 and 175 GPa), the expected shock radiation history with constant intensity characteristic of the Hugoniot temperature is obtained. As illustrated in Figure 3-3a, the recorded temperature is quite constant without indication of relaxation effects, but as detailed in the next chapter, the effective emissivity at these temperatures (near 4500 K) is comparatively low, and decreasing with decreasing pressure.

At pressures lower than this, quite a different behavior is observed. As shown in Figure 3-3b, forsterite shocked to approximately 140 GPa shows a rapid light intensity rise and a subsequent signal decay which persists throughout the entire shock transit time without stabilizing at any well-defined value. It is believed that at pressures below about 150 GPa, the shock front emissivity becomes so small that the shock-compressed

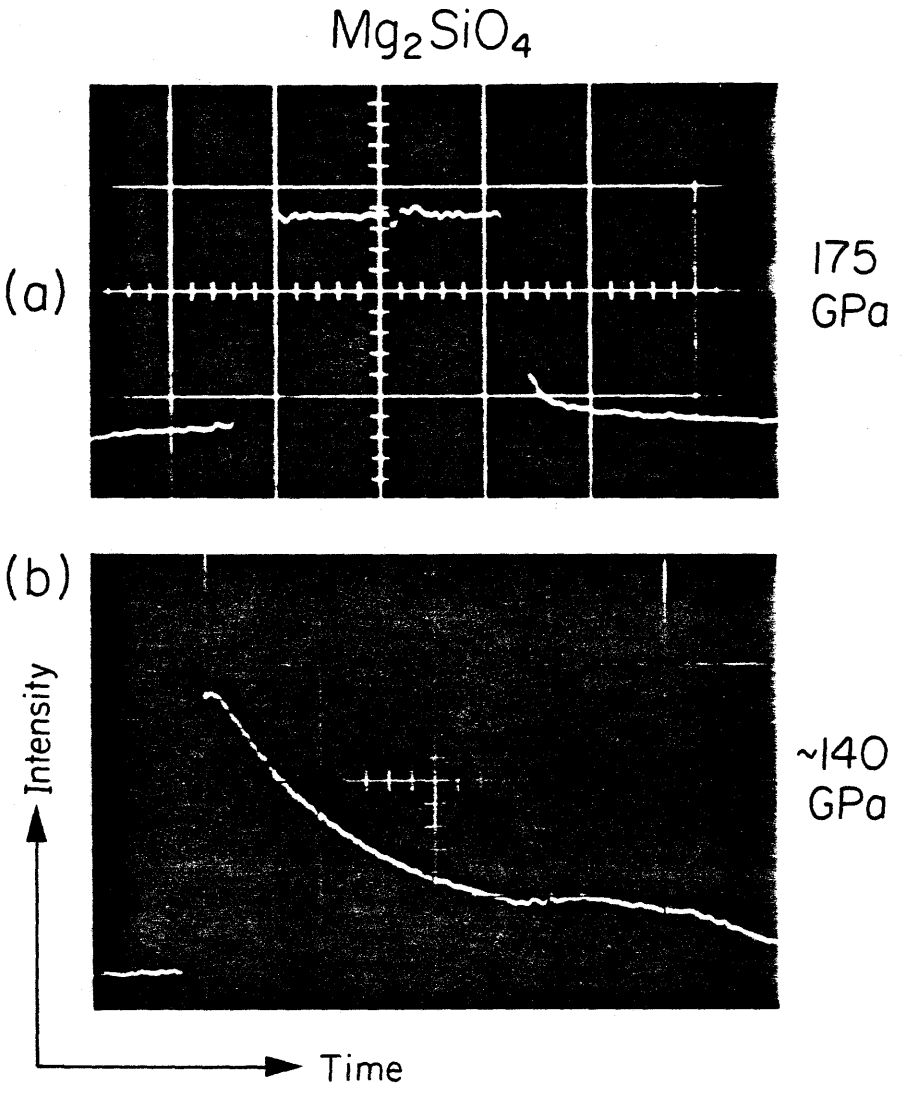

Figure 3-3. Forsterite (Mg_2SiO_4) light intensity records. (a), Shock pressure 175 GPa, 500 nm wavelength. (b), Pressure ~140 GPa, 600 nm wavelength. Record (a) shows normal constant shock luminescence throughout transit. Record (b) shows loss of emissivity in forsterite sample. Horizontal time scales 100 ns per division.

material is essentially transparent, and the recorded light originates in the metal base plate lying behind the sample. With this interpretation, the decaying radiation signature is well explained by the diffusion of heat from the metal/insulator interface. As discussed below, unless great pains are taken to eliminate interfacial gaps and roughness, an initial temperature "spike" will occur at the interface, which decays with a characteristic time dependent upon the thermal diffusivities of the target materials.

Al_2O_3 (sapphire) has displayed such transparency under shock compression over the entire investigated pressure range. While this poses problems for determining the sapphire Hugoniot temperature, it also means that sapphire crystal is a good optical window material in shock experiments in this range. Urtiew [6] has independently shown that Al_2O_3 crystals retain their transparency to shock pressures in excess of 130 GPa. This property has been exploited in the current research program, as described later in this chapter. A single temperature experiment with a crystalline MgO sample yielded indeterminate results suggestive of this type of behavior, but additional experiments will be necessary to verify the nature and range of the phenomenon in this material.

It is apparent that in at least some solid insulators, below some threshold shock temperature or pressure, the free electrons behind the shock front which are assumed to be the source of equilibrium radiation fail to occur. This observation places the lower practical limit on shock temperatures that may be observed by the present technique. This lower limit may not, however, represent so insurmountable an obstacle as the upper temperature limit imposed by electron screening. If a sufficiently

thin metallic layer can be introduced into the investigated sample, this layer will come to thermal equilibrium and radiate with the temperature of the surrounding crystal. Estimating the thermal diffusivity of the samples in question, it appears that a layer of good conductor such as aluminum 0.1 μm in width is sufficiently thin that thermal equilibrium would be achieved on the time scale of the experiment. Since this thickness is large compared with the optical skin depth of a good metal, it is expected that adequate thermal radiation would result. Experiments to investigate this possibility should assume a high priority in future research, especially for materials of geophysical interest in which the relevant temperature range may be below 3000-4000 K.

Shock Temperature Measurements in Metals

Considerable interest centers on the measurement of Hugoniot temperatures in opaque materials such as metals, in addition to the case of transparent insulators discussed above. Unfortunately, the above technique cannot be immediately applied to metals, since optical radiation from the shock-compressed material cannot escape from the opaque sample. Radiation from the free surface at the moment of shock arrival may be monitored, but such measurements pertain to the residual post-shock state of the sample.

A solution to this problem is illustrated schematically in Figure 3-4a. If a material can be found which offers a close shock impedance match to the studied metal and which also remains transparent under shock loading in the pressure range of interest, this material may be used as an "anvil" in a shock pyrometry experiment on the metal layer. When the transparent anvil is placed in contact with the metal sample rear surface, the shock

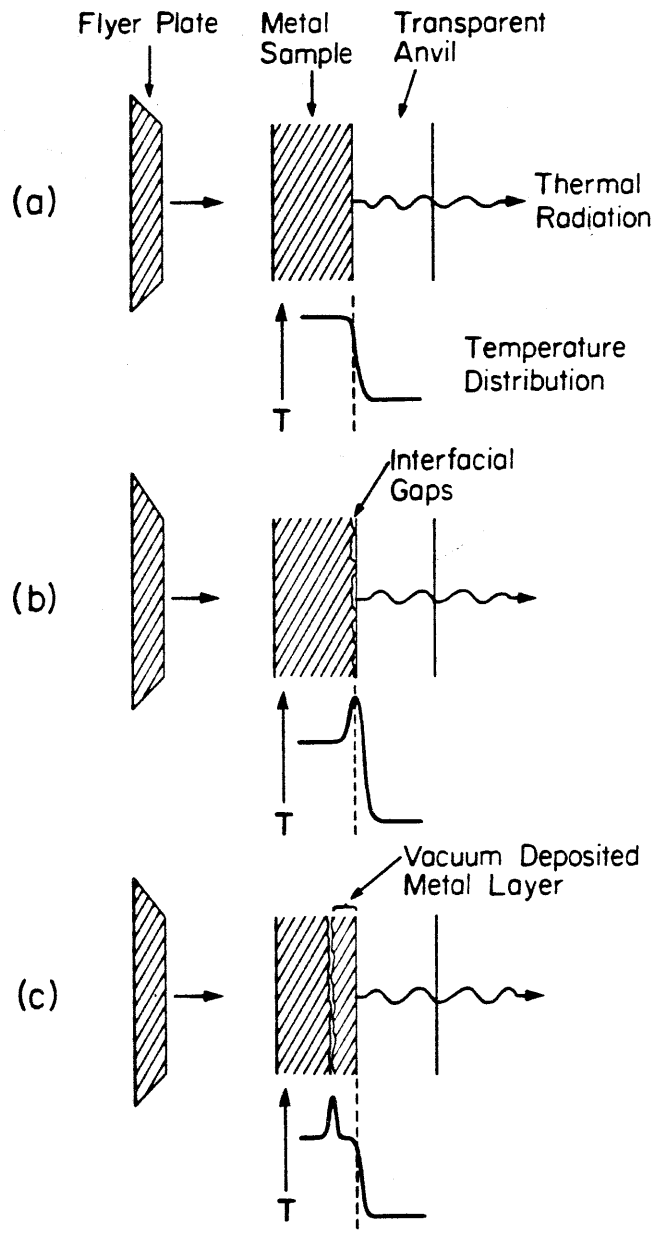

Figure 3-4. Schematic representation of metal Hugoniot temperature measurement. (a), Ideal contact interface between sample and shock anvil provides intermediate temperature value. (b), Interface gaps give rise to temperature perturbation on radiating interface. (c), Vacuum deposited metal layer eliminates gaps, removing temperature perturbation several tens of microns into metal layer.

wave will ideally pass from the metal layer to the anvil with minimal reflected shocks or rarefactions at the interface, thus retaining the metal sample near its original Hugoniot state. Thermal radiation from the hot, compressed metal is then detected by the pyrometer through the transparent anvil.

The temperature actually measured by the pyrometer is not that of the bulk metal sample but that of the sample/anvil interface. As indicated by Figure 3-4a, in a typical case, the anvil is considerably cooler than the Hugoniot temperature of the metal sample, so that this interface temperature gives an underestimate of the true Hugoniot value. It is easily shown (see Grover and Urtiew [7]) that for a heat flow problem governed by the classical one-dimensional thermal diffusion equation, the interface temperature between two semi-infinite media of different uniform initial temperatures T_1 and T_2 is independent of time and given by

$$T_i = T_1 + \frac{T_2 - T_1}{(1+\alpha)} \tag{2}$$

where

$$\alpha = \frac{\kappa_1}{\kappa_2}\left(\frac{D_2}{D_1}\right)^{1/2}. \tag{3}$$

κ and D denote the thermal conductivity and thermal diffusivity, respectively. In the limit that one material has a much higher thermal conductivity than the other, the interface temperature approaches that of the better conductor.

This suggests that given the proper anvil material, preferably one of low thermal conductivity, the proposed temperature measurement in the shock-compressed metal should be easily accomplished. However, a complication arises from the problem of material interfaces, as discussed by

Urtiew and Grover [8]. As shown in Figure 3-4b, the real interface between a polished metal plate and anvil will include roughness and gaps on a scale of microns. As treated quantitatively by Urtiew and Grover, when a shock wave encounters such a gap, release to zero pressure and immediate reshocking of the material immediately before the gap occur. This means that twice-shocked material with an anomalously high temperature will occur in a layer near the interface whose width is of the same order as the gap width (or roughness scale).

As shown, this temperature "spike" at the sample/anvil interface will mask the true Hugoniot temperature. Only after sufficient time has elapsed for this disturbance to dissipate, does the interface assume its time-independent temperature step profile, but for practical purposes, this time is longer than the duration of the experiment.

This problem of interface gaps can be eliminated by careful sample preparation. If the metal layer is prepared in intimate contact with the anvil surface, such as by vacuum deposition or melting, the problem of interface heating can be reduced by orders of magnitude. Since the latter method presents problems for most materials because of differential thermal expansion, vacuum deposition offers the most promise for ideal interface preparation. Since, however, only relatively thin layers can be prepared by this technique, the arrangement shown in Figure 3-4c is used.

A layer of the studied material is vacuum deposited onto the anvil, providing an ideal radiating interface. This thin layer is then backed by a thick plate of the same metal, serving as the impact target. The deposited metal film must be thick enough so that the temperature spike induced in the metal plate at the imperfect interface between the base

plate and film does not have time to diffuse through the film and affect the measured temperature during the length of the experiment.

The set of experiments conducted in the present investigation used silver (Ag) as the investigated metal and single crystal sapphire (Al_2O_3) as the transparent shock anvil. Urtiew [6] pointed out that Al_2O_3 provides a good shock impedance match to many incompressible metals and that furthermore it retains its qualities as a transparent window at high shock pressures where many metals will become hot enough to radiate. Silver was chosen to study because of its shock impedance match to sapphire, its known Hugoniot equation of state, and its ease of evaporation in a vacuum furnace. For the current set of experiments, single crystal sapphire anvils (density 3.98 g/cm^3) were supplied by Adolf Meller Co., cut to ~3 mm thickness and prepared with a surface finish smooth to one microinch. With an evaporated Ag coating on this surface, an effective interface roughness improvement of nearly two orders of magnitude is realized over mechanically joining the two surfaces, which may otherwise depart from uniform contact over the whole surface by microns.

The silver base plates and films were prepared from high purity (99.99%) stock. Early in the pursuit of this study, the technique of sputtering in a low density argon atmosphere was tried to achieve a silver layer of the required thickness. While a thick deposited layer was obtained, examination of the resulting film showed that sputtering yielded a metal layer of high porosity and unsuitable for the present study. Eventually, direct Ag evaporation in high vacuum yielded a good metal film of the required thickness. In order to achieve good adhesion of the film to the anvil, care was required in cleaning the deposition

interface and in cooling the anvil during plating.

A set of experiments was devised to check the validity of the above methods and hopefully to provide a first shock temperature determination in Ag. Using the shock wave data from the Livermore compendium [5] for Ag and Al_2O_3, it was determined that a shock of approximately 200 GPa amplitude in the silver base plate would be transmitted into the Al_2O_3 anvil as a shock of ~150 GPa pressure, with only a modest rarefaction reflected back into the metal. As long as the amount of release occurring due to impedance mismatch is relatively small, a small correction may be applied to the measured (released) temperature to give the temperature of the first shocked state.

Figure 3-5 summarizes the experimental records obtained from this series of shots. Record a) shows the result of a "control" experiment in which a sapphire crystal was simply wrung onto the Ag base plate with no special interface preparation. The contact surfaces were lapped smooth and when assembled, several white-light interference fringes were visible at the interface, indicating a gap size of a few microns. As seen in the oscilloscope trace a), the recorded light intensity reached a peak value immediately upon shock arrival at the anvil and steadily decayed thereafter. This is just the behavior predicted above for the imperfect interface illustrated in Figure 3-4b.

Figure 3-5b gives the oscilloscope record for an Ag shot with a vacuum deposited interface layer. Considering the high thermal diffusivity of a metal like Ag, it was anticipated that a layer thickness of a few tens of microns (μm) would be required to isolate the optical interface from anomalous heat spikes for the several hundred nanosecond

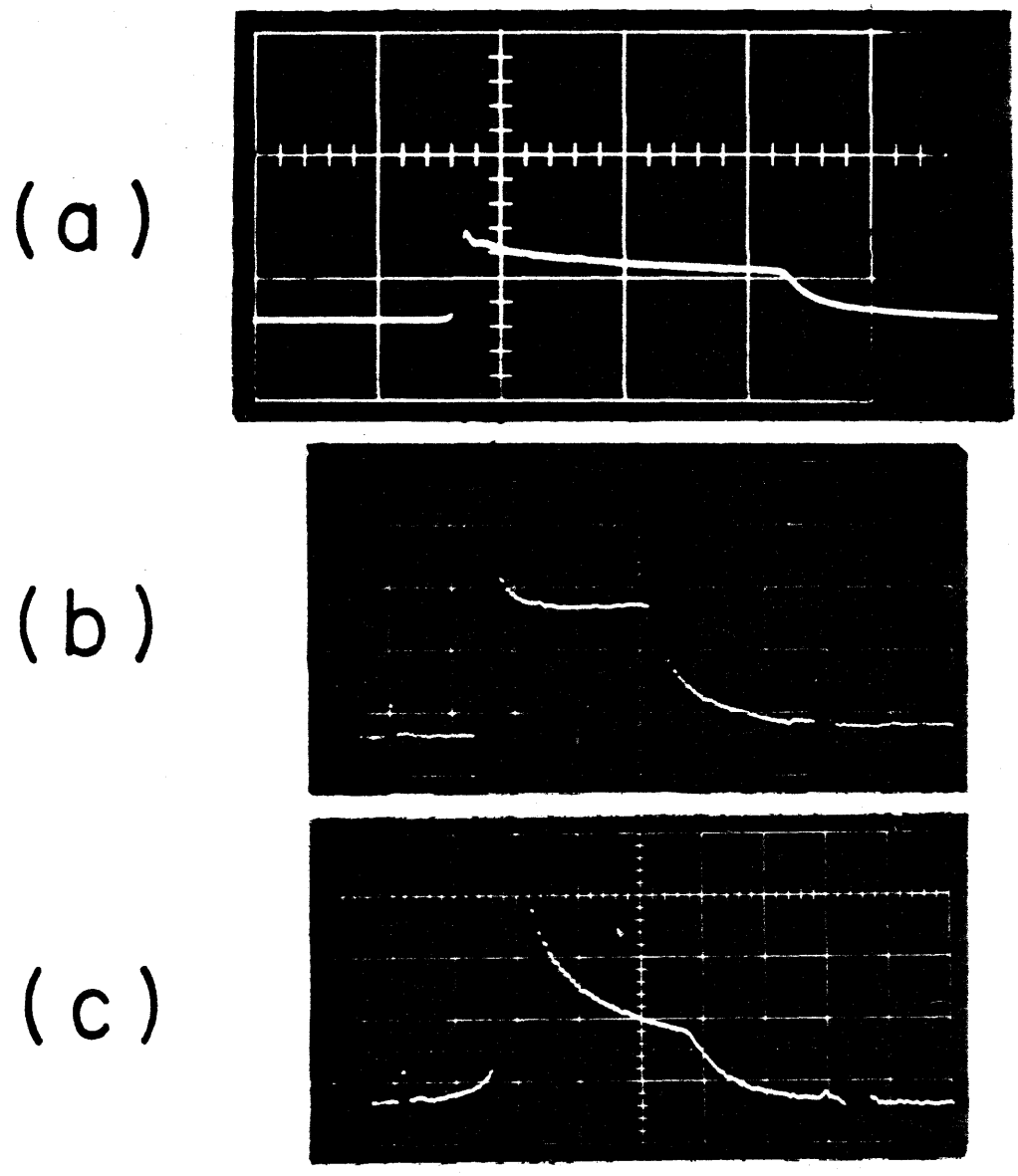

Figure 3-5. Oscilloscope records from Ag temperature experiments using Al_2O_3 anvil. (a), Ag metal base plate in contact with sapphire anvil. Ag shock pressure 222 GPa. (b), 51 μm thick vacuum deposited Ag coating on anvil interface. Ag shock pressure 185 GPa. Note improved temperature constancy. (c), Ag flyer plate direct impact on Al_2O_3 crystal. Shock pressure 120 GPa.

duration of the experiment. In the illustrated experiment, a 51 μm Ag coating was used. The record shows that following a relatively small interface "flash," the radiation settles down to the desired time-independent behavior, apparently giving the ideal interface temperature. The abrupt cutoff of light intensity upon shock arrival at the anvil free surface is apparently due to the breakup and spallation of that surface, resulting in an immediate loss of transparency.

While the experiment b) apparently gave successful results, an additional shot was conducted to explore an alternative solution. In the shot of Figure 3-5c, a silver flyer plate projectile was launched by the light-gas gun for direct impact upon a sapphire crystal with no base plate. The reasoning behind this experiment was that the direct Ag-Al_2O_3 impact would eliminate the problem of multiple-shocking near a gap between the two. While this problem is eliminated, examination of record c) shows that objectionable interface heating occurs regardless. Apparently, the collision process between flyer and target is accompanied by significant micro-jetting and local strong heating due to surface roughness and non-coplanarity, thus completely overwhelming the desired temperature signal. These results indicate that the vacuum plating approach of the experiment in Figure 3-5b is the most promising method. Assuming that this result does reflect the true Ag temperature, we may further examine these data in order to characterize the Ag thermal equation of state.

The parameters of this single successful Ag temperature shot are summarized in Table 3-2. P_1 is the shock pressure in the Ag base plate, while P_2 gives the pressure of the partially released Ag state seen at the metal/anvil interface. The interface temperature T_i was determined

Table 3-2

Ag Shock Temperature Experiment Parameters

Ta impactor velocity, $W = 4.375$ km/s $\pm$ .005

Ag shock pressure, $P_1 = 185.0$ GPa

Ag particle velocity, $u_p = 2.46$ km/s

Al_2O_3 anvil pressure (Ag released state), $P_2 = 134.7$ GPa

Al_2O_3 particle velocity, $u_r = 2.87$ km/s

Measured interface temperature, $T_i = 5030$ K $\pm$ 150

Effective emissivity, $\varepsilon = 0.68 \pm .05$

Estimated anvil temperature,[a] $T_{Al_2O_3} = 1250$ K

---

[a]Walsh and Christian calculation; $\gamma = 1.60\ (V/V_0)$, $\theta_D = 905$ K

as usual by solution of the six wavelength radiance measurements for temperature and emissivity.

In order to derive the Ag Hugoniot temperature from the measured interface value of 5030 K, two corrections must be applied. These corrections are for the cooling effect of the relatively cold anvil in contact with the sample and for the adiabatic cooling experienced by the metal in its partial release from Hugoniot pressure P_1 to P_2. The first of these corrections comes from consideration of equations (2) and (3). α is found by using the standard condition values for the thermal conductivities and diffusivities of Ag and Al_2O_3 as guides along with a general knowledge of how these quantities vary with increasing temperature and density. A general assessment of these quantities allows the parameter α to be estimated conservatively in the range ~3-10. Using $\alpha = 7$ in (3), we obtain the bulk Ag temperature of approximately 5570 K with an uncertainty of roughly 300 K.

In order to obtain the second temperature correction, giving the temperature in the initial state P_1, the amount of volume dilatation the metal has undergone in partial release must be estimated. Assuming that the release process is adiabatic and isentropic, the variation in temperature under isentropic compression (or rarefaction) for a Mie-Grüneisen solid was derived in Chapter 1. For isentropic release from volume V_1 to volume V_2, the temperature change is given by

$$T_2 = T_1 \exp\left[-\int_{V_1}^{V_2} (\gamma/V)\,dV\right]. \qquad (4)$$

For the case of Ag, γ will be assumed to be given by $\gamma(V) = 2.45(V/V_0)^{1.8}$

(see Grover [9]). Volume V_1 is obtained directly from the Hugoniot shock state, but the released volume V_2 is off the Hugoniot curve and must be estimated in some way.

Lyzenga and Ahrens [10] consider the flow in an isentropic rarefaction wave. In such a flow, which takes the material from pressure P_1 to P_2, the additional particle velocity imparted to the material, $u_r - u_p$ is related to the P-V release path through the Riemann integral,

$$u_r - u_p = \int_{P_2}^{P_1} \left(-\frac{dV}{dP}\right)^{1/2} dP. \tag{5}$$

Here, u_p is the particle velocity in the shocked state, while u_r is the released state particle velocity. In [10] it is shown that an extremum of (5) is obtained if the release path V(P) is a linear function. In particular, this gives a maximum for the velocity jump in (5), and for a given value of $u_r - u_p$, it provides a lower limit for the released volume V_2. It is shown in [10] that

$$V_2 \geq V_1 + \frac{(u_r - u_p)^2}{(P_1 - P_2)} \tag{6}$$

for any isentropic release path between P_1 and P_2.

This gives a lower limit for V_2, and for a sufficiently short release path, the linear release adiabat cannot be a bad approximation of the actual path. We therefore assume for the current problem that V_2 is given by the equality in (6). The Ag particle velocity at shock pressure $P_1 = 185$ GPa is $u_p = 2.46$ km/s. The released velocity, which is equal to the Al_2O_3 particle velocity at $P_2 = 134.7$ GPa is $u_r = 2.87$ km/s. With $V_1 = 6.265 \times 10^{-5}$ m^3/kg, we obtain $V_2 \approx 6.60 \times 10^{-5}$ m^3/kg.

With these values, we may now evaluate the integral of equation (4). The exponential term is ~0.94, so that the corrected Hugoniot temperature of Ag at 185 GPa is approximately 5950 K. This temperature may now be compared with the calculated Hugoniot temperature. When the temperature Hugoniot is computed by the Walsh and Christian method (Chapter 1), using the above $\gamma(V)$ and C_v given by the Debye model with $\theta_D = 225$ K, the calculated value of T_H at 185 GPa pressure is ~7200 K. The calculated temperature appears to be well above experimental value, and an explanation of this discrepancy is desired.

If the estimated Ag equation of state is not grossly incorrect, then a mechanism or transition is sought which will account for a shock temperature over 1000 K lower than predicted. The melting transition is a good candidate for this solution, especially since no evidence for a solid state transition with a large volume change is apparent in the existing Hugoniot data. An estimate of the melting behavior of Ag at high pressures may be obtained by appealing to a theory of melting, such as the semi-empirical Lindemann melting criterion.

As shown by Grover [9], Lindemann's law, which relates the volume dependence of the melting temperature to the average amplitude of atomic lattice vibrations, may be cast in a form involving the Grüneisen parameter γ. Grover shows that

$$\frac{d\ \ell n\ T_m}{d\ \ell n\ V} = -\frac{V}{T_m}\frac{dT_m}{dV} = 2\gamma - 2/3, \qquad (7)$$

which holds well for metals, and in the case of Ag, $\gamma_0 = 2.86$ gives the best fit for low pressures.

Figure 3-6 shows the T-V melting curve for Ag computed from (7),

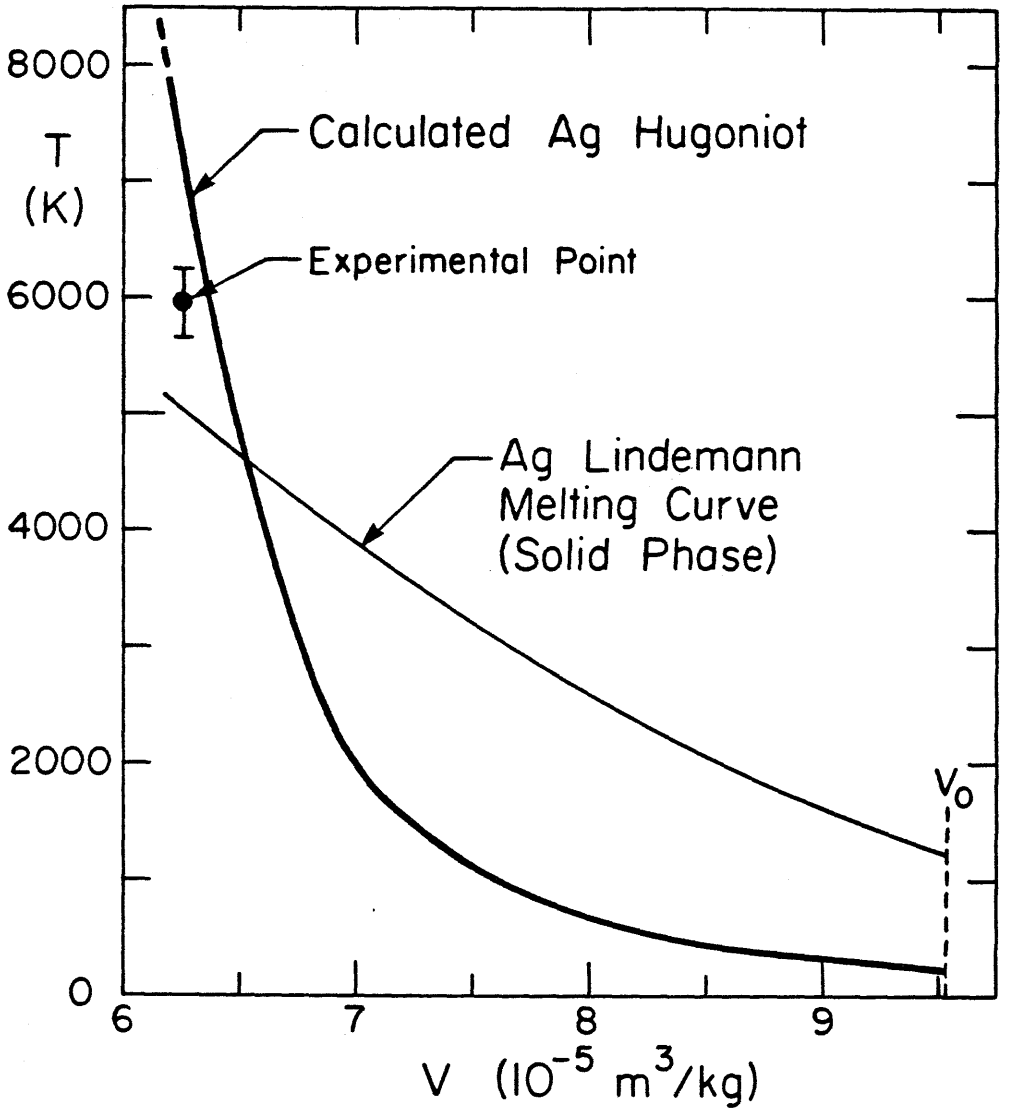

Figure 3-6. Calculated Ag Hugoniot and melting line in temperature-volume plane. Melting line is calculated from Lindemann law applied to solid phase and represents the solid-mixed phase boundary. Experimental point is corrected for release and heat diffusion effects.

assuming a zero-pressure melting temperature of 1234 K. As seen in this plot, the Lindemann melting line crosses the computed solid phase Hugoniot at a temperature near 4600 K, corresponding to a shock pressure of 137 GPa. This estimate is consistent with the occurrence of shock-induced melting in the present example at 185 GPa pressure. It will be useful to consider the slope of the estimated Lindemann melting line translated into the pressure-temperature plane. The total derivative dT/dP taken along the melting line is given by

$$\frac{dT}{dP} = \left(\frac{\partial T}{\partial P}\right)_V + \left(\frac{\partial T}{\partial V}\right)_P \left(\frac{dP}{dV}\right)^{-1} \tag{8}$$

Now the total derivative dP/dV for the solid phase along the melting line is given by

$$\frac{dT}{dV} = -\frac{T}{V}\left(2\gamma - \frac{2}{3}\right) = \left(\frac{\partial T}{\partial V}\right)_P + \left(\frac{\partial T}{\partial P}\right)_V \frac{dP}{dV}, \tag{9}$$

using (7) for dT/dV. This gives for dT/dP in (8),

$$\frac{dT}{dP} = \left(\frac{\partial T}{\partial P}\right)_V \left\{1 - \left[\frac{T}{V}\left(\frac{\partial V}{\partial T}\right)_P \left(2\gamma - \frac{2}{3}\right) + 1\right]^{-1}\right\}. \tag{10}$$

In the Mie-Grüneisen assumption, $\left(\frac{\partial T}{\partial P}\right)_V$ and $\left(\frac{\partial V}{\partial T}\right)_P$ are obtainable from the equation of state parameters γ, C_v, and K_T (Chapter 1). The above melting line slope is evaluated where the computed Hugoniot crosses the Lindemann line, at $V = 6.54 \times 10^{-5}$ m^3/kg, $T = 4575$ K and $P = 136.7$ GPa. The result obtained is $dT_m/dP \approx 12.3$ K/GPa.

Figure 3-7 shows the P-T Hugoniot along with the derived Lindemann law melting line. As illustrated in this plot, the temperature Hugoniot curve coincides with the phase coexistence line throughout the mixed phase region and moves up into the liquid field as the transition is complete. To a first approximation, the liquid Hugoniot should lie below the calculated solid Hugoniot by a temperature difference roughly equal to the latent

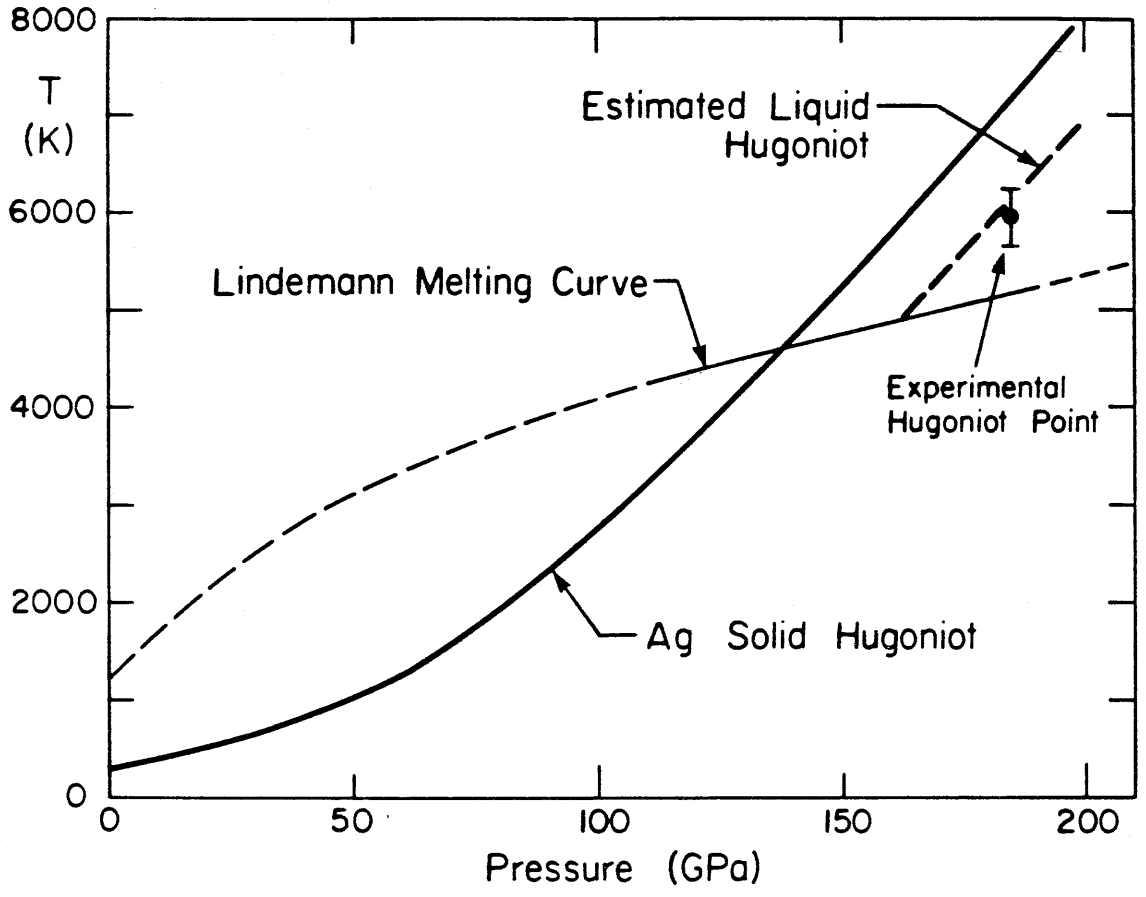

Figure 3-7. Ag in pressure-temperature plane. Calculated Hugoniot shown for solid phase and estimated for liquid phase (dashed) above Lindemann melting curve. Corrected experimental Ag shock temperature point is believed to fall on the liquid phase Hugoniot.

heat divided by the specific heat.

Knowing the slope of the melting line allows an estimate of the latent heat of fusion, L_m. Stishov [11] has examined the systematics of melting at high pressures and finds a high-pressure limit for the relative volume change $\Delta V/V$ upon melting of simple metals of roughly 1%. Using this in the Clausius-Clapeyron relation,

$$\frac{dT_m}{dP} = \frac{T\Delta V}{L_m} \tag{11}$$

we find $L_m \approx 0.24$ MJ/kg. This corresponds to an entropy of melting $\Delta S \approx 0.7$ R per mole of atoms, which agrees with Stishov's systematics for the high-pressure limit to ΔS.

Using this latent heat to estimate the position of the liquid temperature Hugoniot, it should lie below the solid Hugoniot by approximately 1040 K, as illustrated in Figure 3-7. Interestingly, the experimental Hugoniot temperature point at 185 GPa falls almost squarely on the calculated melt Hugoniot. Apparently, the observed temperature is well-explained by invoking shock-induced melting, with a pressure-volume dependence given by the Lindemann criterion. Of course, verification of this conclusion will require additional experiments, spanning the pressure range which includes the assumed melting transition.

While the possibility of detecting and characterizing the melting of silver at very high pressures is an interesting prospect in itself, it also raises the possibility of making similar measurements in other more important metals. Urtiew and Grover [12] have discussed the melting of magnesium under shock loading using similar techniques, but their work primarily explored states off the Hugoniot curve.

Fortuitously, the geophysically very important metal iron (Fe) also displays a good shock impedance match with Al_2O_3, so that the same temperature measurement technique described above is applicable. Assuming that the problems of vacuum deposition and sample preparation are solved for Fe, this technique should allow detection of the iron melting point in the pressure range 100-200 GPa. This measurement has far-reaching importance for the physics of the earth's core, since the liquid outer core and solid inner core are most probably alloys of iron, and a knowledge of the iron melting curve would serve to constrain the earth's internal temperature distribution. The hypothetical melting of iron under shock loading has been the subject of much investigation already, for example, Hopson et al. [13], and the present technique may well offer a most powerful tool for the solution of this problem.

In summary, shock temperatures in metals may be measured by the shock anvil technique, subject to the solution of two problems. These problems are the elimination of interfacial gap heating and the proper correction of interface temperature for heat diffusion into the anvil. The current results for silver suggest that these problems can be solved and, furthermore, that the technique offers great promise for other interesting metals.

REFERENCES

1. Kormer, S. B., M. V. Sinitsyn, G. A. Kirillov and V. D. Urlin, Experimental determination of temperature in shock-compressed NaCl and KCl and of their melting curves at pressures up to 700 kbar, Sov. Phys. JETP, 21, 689-700 (1965).

2. Kormer, S. B., Optical study of the characteristics of shock-compressed condensed dielectrics, Sov. Phys. Usp., 11, 229-254 (1968).

3. Al'tshuler, L. V., Use of shock waves in high-pressure physics, Sov. Phys. Usp., 8, 52-91 (1965).

4. Mitchell, A. C., W. J. Nellis and B. L. Hord, Tantalum Hugoniot measurements to 430 GPa (4.3 Mbar) (abstract), Bull. Am. Phys. Soc., 24, 719 (1979).

5. Van Thiel, M., editor, Compendium of Shock Wave Data, Report UCRL-50108, Lawrence Livermore Laboratory, University of California, Livermore, CA (1977).

6. Urtiew, P. A., Effect of shock loading on transparency of sapphire crystals, J. Appl. Phys., 45, 3490-3493 (1974).

7. Grover, R., and P. A. Urtiew, Thermal relaxation at interfaces following shock compression, J. Appl. Phys., 45, 146-152 (1974).

8. Urtiew, P. A., and R. Grover, Temperature deposition caused by shock interactions with material interfaces, J. Appl. Phys., 45, 140-145 (1974).

9. Grover, R., Liquid metal equation of state based on scaling, J. Chem. Phys., 55, 3435-3441 (1971).

10. Lyzenga, G. A., and T. J. Ahrens, The relation between the shock-induced free-surface velocity and the postshock specific volume of solids, J. Appl. Phys., 49, 201-204 (1978).

11. Stishov, S. M., The thermodynamics of melting of simple substances, Sov. Phys. Usp., 17, 625-643 (1975).

12. Urtiew, P. A., and R. Grover, The melting temperature of magnesium under shock loading, J. Appl. Phys., 48, 1122-1126 (1977).

13. Hopson, J. W., R. G. McQueen and J. M. Brown, The velocity of sound behind shocked iron (abstract), Trans. Am. Geophys. U., 60, 951 (1979).

Chapter 4

SHOCK TEMPERATURES OF SiO_2 AND Mg_2SiO_4: EXPERIMENTAL RESULTS AND GEOPHYSICAL IMPLICATIONS

Introduction

The properties of silica and its high-pressure polymorphs have long been of interest because of their bearing on problems of the physical and compositional states of planetary interiors. Models of the high-pressure equation of state and phase diagram of SiO_2 may provide direct information about candidate mantle mineral assemblages, because SiO_2 readily transforms to a rutile-like phase (stishovite) above 14 GPa (McQueen et al., [1]) in which Si^{+4} has octahedral oxygen coordination. It would therefore appear to be a good model of other lower mantle octahedrally coordinated silicates (Liu, [2]). Similarly, the study of forsterite (Mg_2SiO_4) and its high-pressure phases can provide valuable information about what may be the dominant lower mantle mineral assemblage (Jackson and Ahrens, [3]). Modern techniques for the dynamic compression of minerals (Ahrens, [4]) are providing such data at pressures near 100 GPa, which are appropriate to the state of the earth's lower mantle and core.

Shock wave compression of solids depends upon the generation and propagation of a planar, steady pressure step in the material of interest. As described previously, the time-independent profile of this pressure discontinuity or shock front in one-dimensional flow allows application

of the Rankine-Hugoniot conservation equations, which relate pressure, density, and energy of the compressed state to the shock and mass velocities of the flow. The Hugoniot curve or locus of (P, V, E) states accessible to a given material when shocked is thus measurable through observations of shock wave propagation. One technique for producing and characterizing such shocks is the method of flying plate impact, through the use of a two-stage gas gun (Chapter 2). This apparatus accelerates projectiles bearing metallic flyer plates to speeds of up to 7 km/sec, which upon impact induce shock pressures in silicate specimens in excess of 150 GPa.

For silicates and oxides of geophysical interest, data for the Hugoniot shock state are of considerable interest. It is demonstrated below that Hugoniot temperature measurements can provide an important source of data specifying the thermal pressure component of the equation of state, which is not explicitly obtainable from the R-H conservation equations. The present optical pyrometry method for shock temperature measurement, developed jointly with Lawrence Livermore Laboratory, is applicable to transparent materials and has been used to demonstrate how the thermal behavior and energy associated with phase changes in forsterite and silica may be constrained. The new data and analysis of measured shock temperatures in SiO_2, when taken with the independent work of McQueen et al. [6] provide important new information about the high-pressure phases of SiO_2, which may be applied directly in placing an absolute upper limit on the temperature in the earth's mantle, and indirectly, in providing the basis for estimation of the melting point of the lower mantle, and thus its viscosity. Furthermore, evidence in the present work for shock-induced transformation of forsterite to a high-pressure polymorph contributes to

an understanding of the behavior of this mineral at depth in the earth.

SiO_2 Experimental

Samples of single crystal and fused quartz were driven to shock pressures in the range from 60 to 140 GPa via impact of 2 mm thick flyer plates accelerated to speeds of from 4.5 to 6.7 km/sec using the two-stage light gas gun facility at Lawrence Livermore Laboratory. Thermal radiation emitted by the shocked samples during the period (approximately 300 to 400 ns) of shock wave transit were measured by the pyrometer, at each of six visible wavelengths simultaneously. Briefly, the technique utilizes the thermal radiation emitted from the high-pressure shocked portion of the sample, viewed through the unshocked sample. The intensity is detected via six similar optical paths and detected by an array of PIN silicon photodiodes whose output is recorded by an oscilloscope, with a time resolution of typically 5 ns.

The emitted light radiation (Figure 4-1) rises to nearly full intensity very rapidly (within ~5 ns) upon the shock arrival in the sample. The recorded signal then remains nearly constant approaching what appears to be an asymptotic value until shock arrival at the free surface, when the light is immediately extinguished, presumably by free-surface break-up. It is apparent from data presented below that the radiation detected originates in the shock front or a very narrow region near the front, in order to account for the very rapid rise times, which are less than or equal to the instrumental rise time.

As has been described previously (Chapter 2), a given experiment yields six values of the spectral radiance of the sample at different

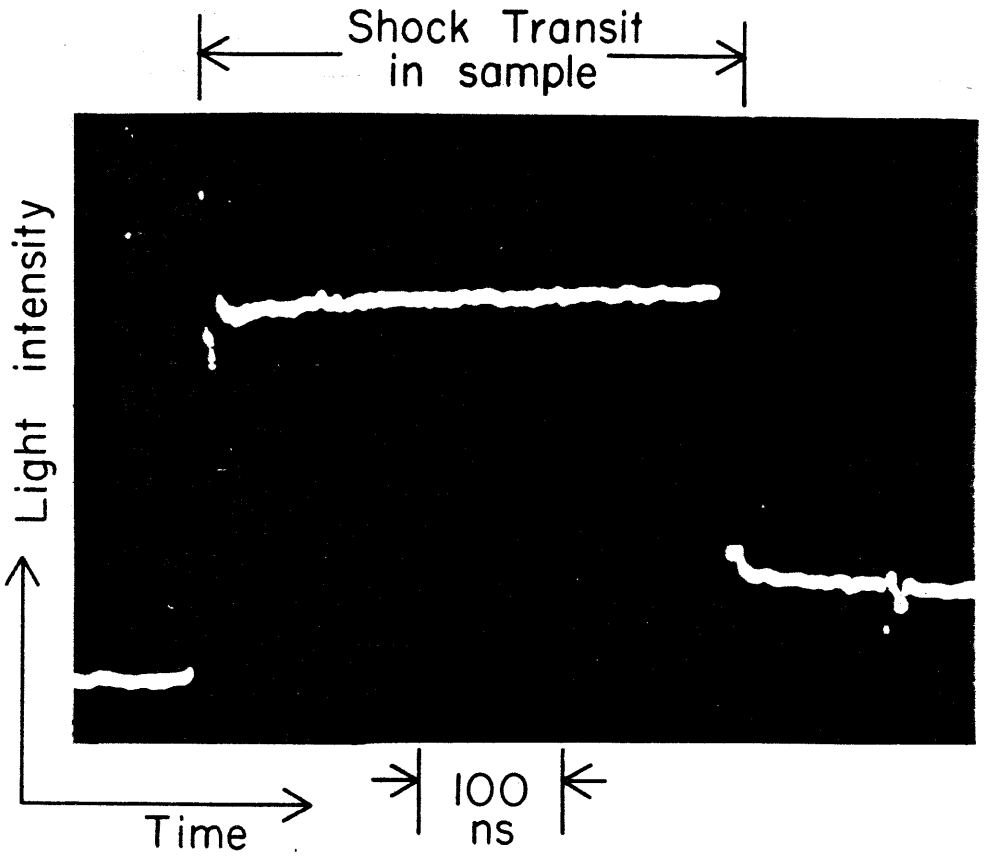

Figure 4-1. Oscilloscope record of shock-induced light intensity versus time. Record is taken through 650 nm wavelength interference filter from a fused quartz shot at 68.5 GPa pressure. Each shot results in six such records at wavelengths of 450, 500, 550, 600, 650, and 800 nm. The spectral radiance calibration for this channel is approximately 3.9×10^3 W/m^2/sr/nm per division.

wavelengths, which may be inverted to determine the temperature and emissivity of the sample during the flat "plateau" region of the record. In all results reported here, the data have been inverted under the assumption that the measured radiation spectrum is given by a Planck blackbody profile, modified by an emissivity factor independent of wavelength. Thus, each shot inversion represents a two-parameter fit to the data. In addition to obtaining temperature information from the oscilloscope records, conventional Hugoniot pressure measurements may be obtained from the sample shock velocity and flyer plate speed using the impedance match technique from Al'tshuler [7]. The shock velocity measurement depends upon the very abrupt onset and the decline of shock-induced radiance. Shock-transit times and shock velocities can with this technique be determined with a precision of about 1%. Factors limiting the precision of this technique appear to be the electronics rise time, and the degree of "tilt" of the shock front from ideal coplanarity with the sample interfaces.

The results of nine shots on single crystal α-quartz are summarized in Table 4-1. The samples used in this series of experiments were synthetic quartz crystals with an initial density of 2.648 g/cm^3, supplied by the Adolf Meller Co. The prepared samples were discs approximately 3 mm in thickness by 17 mm in diameter, polished to optical smoothness. Shots were carried out on crystals oriented with the (0001) axis oriented both parallel and perpendicular to the direction of shock propagation, as noted in Table 4-1. The α-quartz experiments were carried out at pressures between approximately 75 and 140 GPa, in a range where stishovite is assumed to be the stable solid phase of SiO_2 (McQueen, et al. [1]). As is discussed below, the shock temperature data show that a temperature

Table 4-1

α-quartz Hugoniot Temperatures

Shock Pressure (GPa)	Temperature (K)	Emissivity
75.9 ± 0.8[a]	4600 ± 150	.70 ± .05
85.9 ± 1.0[b]	4860 ± 150	.90 ± .07
92.5 ± 1.0[a]	5400 ± 150	.87 ± .07
99.3 ± 1.0[a]	5470 ± 150	.97 ± .07
107.8 ± 1.0[b]	5820 ± 150	.97 ± .07
109.7 ± 1.0[a]	5700 ± 150[c]	.96 ± .07
116.5 ± 1.0[b]	4880 ± 150	.88 ± .07
126.6 ± 1.0[a]	5390 ± 150	.80 ± .07
137.0 ± 1.0[b]	5990 ± 200	.72 ± .07

[a] Shock propagation perpendicular to (0001) axis.

[b] Shock propagation parallel to (0001) axis.

[c] Temperature based upon only two wavelength radiance measurements instead of six.

decline in excess of 1000 K occurs between pressures of 107 and 117 GPa. This temperature drop is illustrated graphically in Figure 4-2 and is taken as evidence of a shock-induced phase transition in stishovite.

Table 4-2 summarizes the results of seven shots carried out with samples of fused silica. The polished discs had an initial density of 2.204 g/cm^3 and were supplied by Amersil Corp. The pressure range studied was 58 to 108 GPa. As in the case of α-quartz, the fused quartz temperature data show evidence for a phase change in stishovite. A similar temperature drop is observed to occur, although at a lower pressure than in the α-quartz experiments.

As seen in the plot of Figure 4-3, the behavior in the region of temperature decline in fused quartz near 65-70 GPa pressure appears similar to that in α-quartz. The two anomalous temperature segments, however, do not connect to form a continuous curve as would be expected if they delineate an equilibrium phase boundary. In such a case, the Hugoniot would coincide with the phase line through the region of mixed phases, moving into the high-pressure phase region at higher shock pressures (Duvall and Graham, [8]). In any case, it is assumed here that all differences between the Hugoniot curves for α-quartz and fused silica result from the different initial densities and consequently different internal energies of SiO_2 shocked from the two different starting phases. Also plotted in Figures 4-2 and 4-3 are the calculated Hugoniot temperature curves for SiO_2 in the crystalline stishovite phase. The details of this calculation have been discussed earlier (Chapter 1). The calculated curves are sensitive to the assumed values of E_{tr} for stishovite from the initial phases. The values assumed here are 0.822 MJ/kg and 0.697 MJ/kg

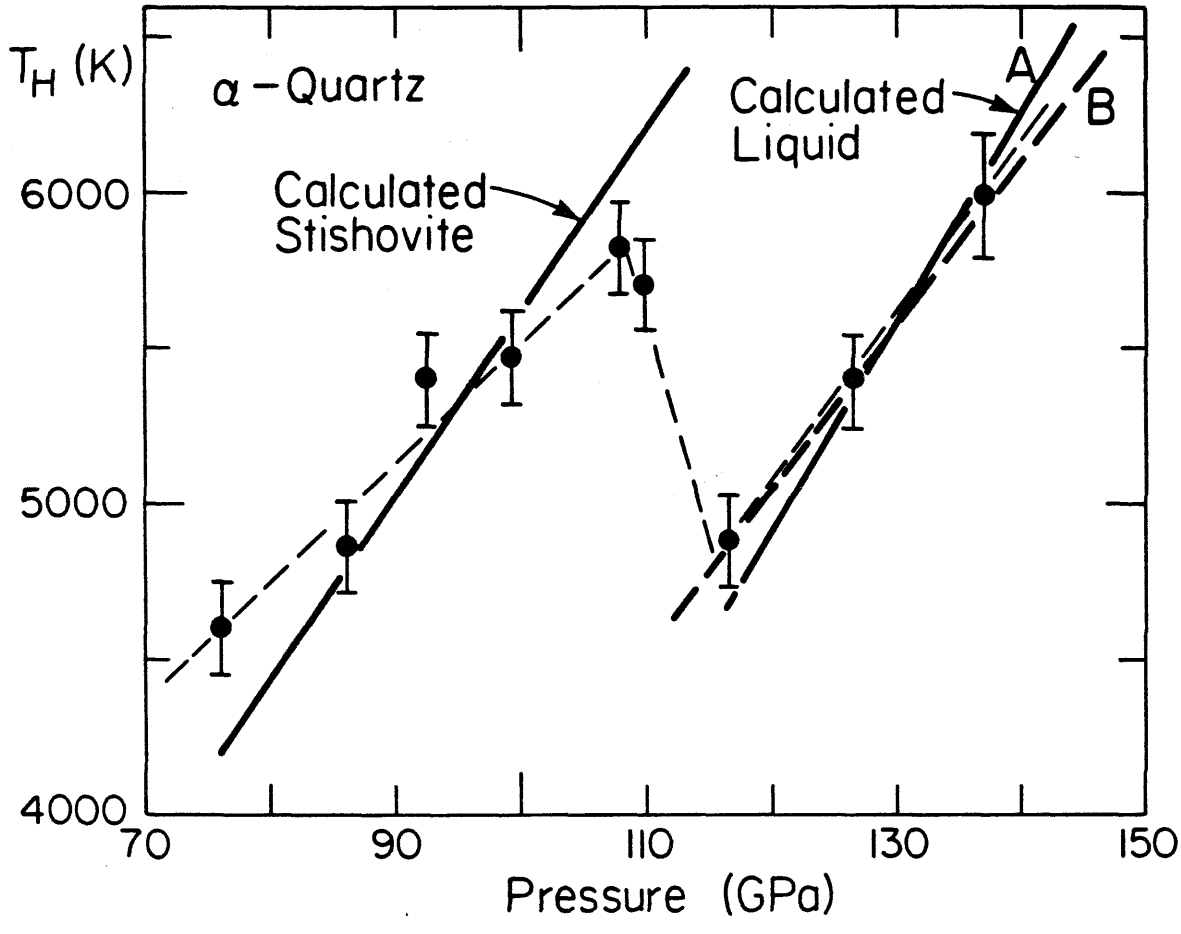

Figure 4-2. Measured shock temperatures versus pressure from experiments on single crystal α-quartz. Heavy solid and dashed lines are calculated Hugoniot temperatures assuming SiO_2 in solid stishovite phase, and in a liquid phase. Curve labelled A is calculated assuming a monatomic metal specific heat and 3.4 MJ/kg transition energy at standard conditions. Fit B assumes a large specific heat of ~4.2 R per mole of atoms, and a metastable standard state energy 0.5 MJ/kg above fused silica reference state.

Table 4-2

Fused Quartz Hugoniot Temperatures

Shock Pressure (GPa)	Temperature (K)	Emissivity
58.9 ± 1.0	4980 ± 150	.85 ± .05
68.5 ± 1.0	5130 ± 150	.85 ± .05
73.3 ± 1.0	4700 ± 150	.79 ± .05
81.2 ± 1.0	5360 ± 150	.75 ± .05
93.2 ± 1.5	5800 ± 200	.84 ± .05
104.2 ± 2.0	6500 ± 300	.90 ± .10
109.9 ± 2.0	6800 ± 300	~1.0

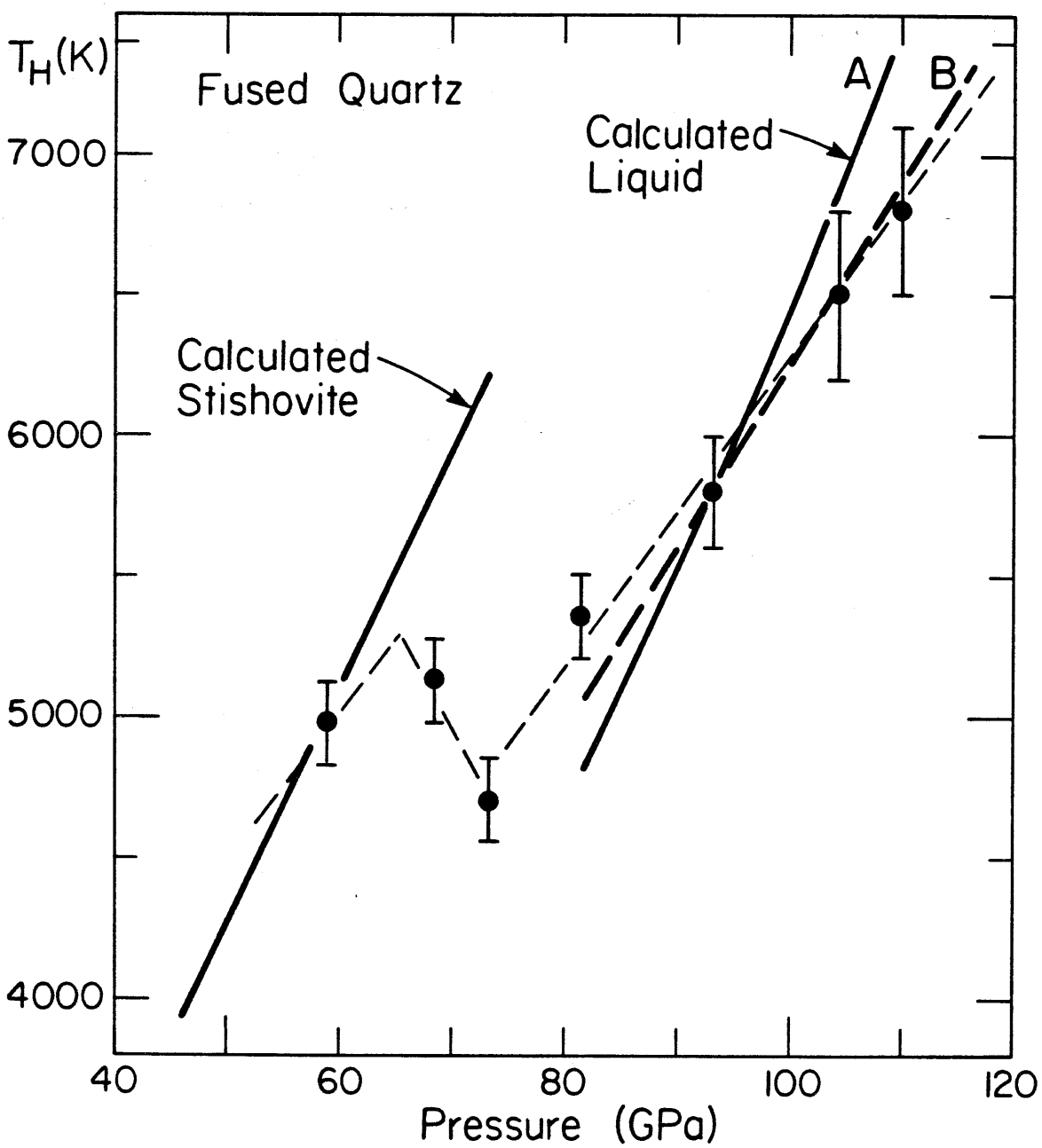

Figure 4-3. Measured shock temperatures as a function of pressure in experiments with fused quartz. Calculated stishovite and liquid Hugoniot temperatures are shown as in Figure 4-2.

for α-quartz and fused silica respectively, as measured calorimetrically (Robie, et al. [9]). The Grüneisen parameter $\gamma(V)$ was estimated prior to this work using the results of Jeanloz and Richter [5], and stishovite calculations were made for a constant $\gamma = 0.9$. It is notable that in both materials, the measured Hugoniot temperature curves show reasonable agreement with the stishovite calculations at pressures below the observed transitions, and that above the transitions, both Hugoniots lie well below the predicted temperatures. These observations lend support to the view that the peculiar temperature behavior seen in both materials signals the same phase transition from stishovite to a new phase, even though the transition is apparently not accomplished under equilibrium conditions.

As is discussed extensively in McQueen et al. [6], a shock wave which decreases in amplitude with time may be used to investigate the anomalous region of decreasing temperature. Those investigators have observed the radiation from a decaying shock front in fused quartz and have noted the expected temperature reversal, among other interesting results. Their results are confirmed by a single experiment from this work, in which a thin flying impactor plate was employed to generate a decaying shock front (Fowles, [10]) in the fused quartz sample. As seen in Figure 4-4(a), the radiation intensity from the sample initially falls and then rises before extinguishing as the shock pressure falls in amplitude. The thermodynamic path traced out by the radiating shock front is along the Hugoniot rather than along a release adiabat, since at a given instant the material being viewed by the pyrometer is new material which is immediately behind the front and has been just shocked up to the amplitude of the decaying wave at that instant. In the illustrated experiment, the initial shock pressure

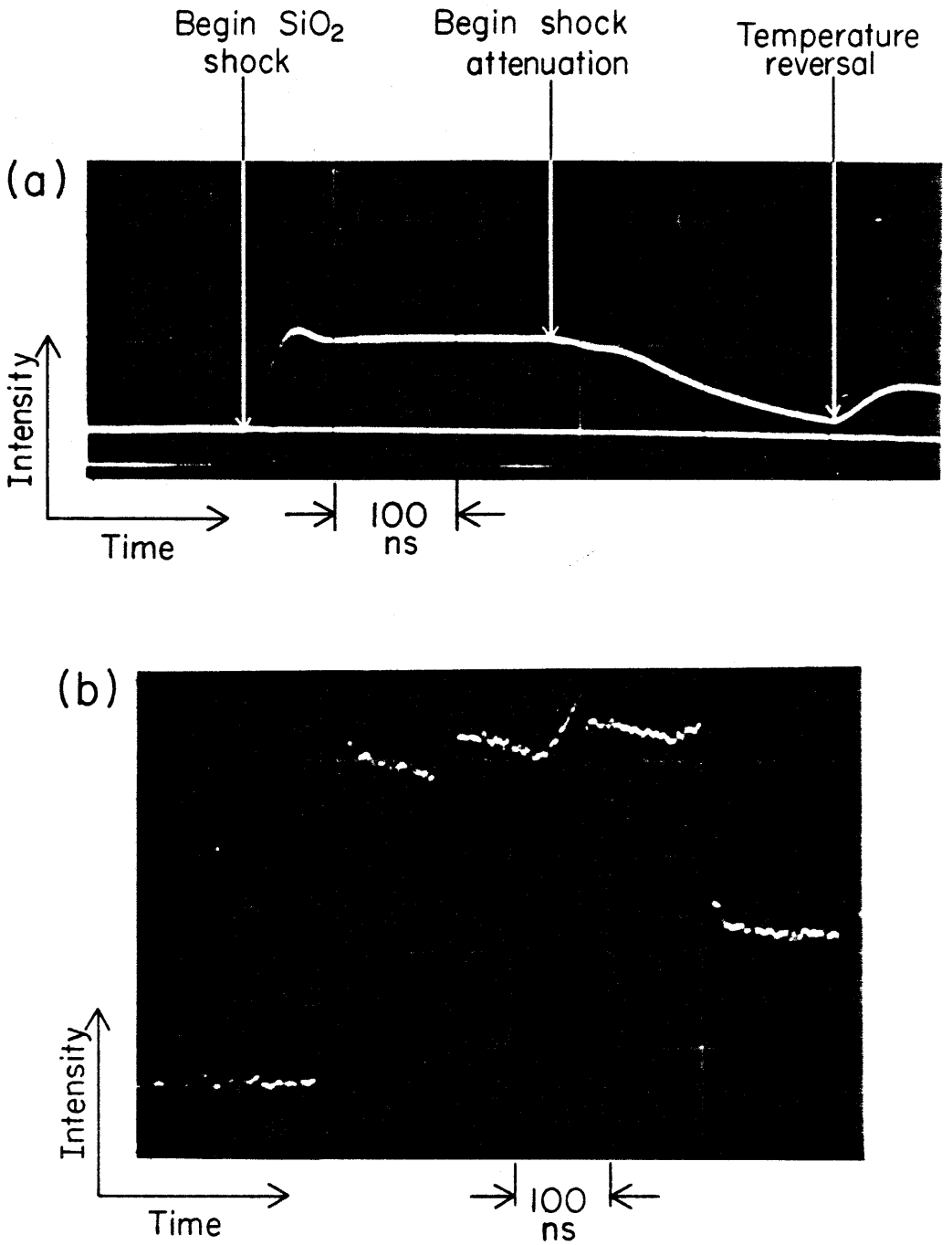

Figure 4-4. (a) Light intensity versus time record for fused quartz experiment with decaying shock amplitude. Peak shock pressure is 97.5 GPa. Temperature increase is observed as shock pressure decreases. Wavelength 500 nm. (b) Intensity record for fused quartz shot at 73.3 GPa pressure. Light intensity fluctuations are observed at this pressure near the shock temperature minimum. Calibration for this 650 nm wavelength record is ~2.2 × 10^3 $W/m^2/sr/nm$ per division.

is 97.5 GPa, and as the pressure falls, the material passes continuously through states on the Hugoniot including the phase transition.

According to the data in Figure 4-3 the temperature reversal is expected at a pressure of ~73 GPa. Figure 4-4(b) shows the intensity record from another fused quartz shot, in this case with constant shock amplitude. At the pressure of this shot, ~73 GPa, the material is evidently at or near the temperature minimum which signals the switch from the anomalous transition region to the higher pressure phase. Unusual quasi-periodic small jumps in intensity are observed during the shock-wave transit. This behavior was not observed in identical experimental configurations at different pressures and could not be otherwise reproduced with the electronics and cabling of the experiment, thus apparently ruling it out as an instrumental effect other than random noise. This behavior is analogous to the oscillating optical signal reported by McQueen et al. [6] in the same pressure range and may be related to rate effects and lower phase metastability near the phase transition pressure.

The existence of such a shock-induced phase transition immediately suggests the possibility of finding evidence for it in other shock wave data. α-quartz is the best candidate for such a study, since its higher initial density makes the shock heating and masking effect of thermal pressure less than in the case of fused silica. The previously published Hugoniot data for α-quartz consist of points obtained at pressures below approximately 100 GPa (Wackerle [11] and McQueen et al. [6], Podurets et al. [12]), and a few high-pressure points obtained near 200 GPa and above (Trunin et al. [13]). These data do not overlap the region of the inferred phase change, so in the present study we have used shock transit

times from temperature experiments in addition to more conventional streak camera experiments to obtain additional points between 90 and 140 GPa. These data are listed in Table 4-3, and a summary of all α-quartz data above the stishovite transition (~40 GPa) is presented in a plot of shock velocity versus particle velocity in Figure 4-5. The improved Hugoniot data obtained for both α-quartz and fused silica have resulted in small corrections to the pressures in the temperature experiments, thus accounting for differences between the pressures reported here and those in Lyzenga and Ahrens [14].

The data for experiments below the 117 GPa completion pressure of the transition seen in the temperature data are well fitted by a linear u_s-u_p relation, with a least squares best fit given by

$$u_s = 1.822\ u_p + 1.370 \text{ km/s}. \qquad (1)$$

This agrees with the fit assigned by McQueen et al. [6] of

$$u_s = 1.850\ (\pm\ .045)\ u_p + 1.241\ (\pm\ .16) \text{ km/s}. \qquad (2)$$

In contrast, the Hugoniot points from experiments at pressures higher than the new transition do not fall on this extrapolated linear fit. While the limited data available do not absolutely exclude the possibility of fitting the Hugoniot data with a single smooth curve, the higher pressure points have here been fit with another linear segment of shallower slope. The fit line shown in Figure 4-5 is given by

$$u_s = 1.619\ u_p + 2.049 \text{ km/s}\ . \qquad (3)$$

Besides the shallower slope on the high-pressure branch, this two-segment fit evidently requires a discontinuity between the two branches rather than a smooth joining of the two where the break in slope occurs.

Table 4-3

Supplemental SiO_2 Hugoniot Data

Studied Sample	Tantalum Impactor Velocity W (km/s)	Sample Shock Velocity (measured) U_s (km/s)	Sample Particle Velocity (calculated) U_p (km/s)	Pressure (calculated) P (GPa)
α-quartz	5.172 ± .007	8.64 ± .06	4.02 ± .01	92.0 ± 0.7
α-quartz[a]	5.62 ± .01	9.27 ± .16	4.34 ± .02	106.5 ± 1.9
α-quartz[a]	5.871 ± .010	9.73 ± .06	4.51 ± .01	116.0 ± 1.4
α-quartz	5.926 ± .011	9.70 ± .12	4.55 ± .01	116.9 ± 1.4
α-quartz	6.297 ± .012	9.82 ± .10	4.84 ± .01	126.0 ± 1.5
α-quartz	6.600 ± .012	10.30 ± .10	5.05 ± .01	137.7 ± 1.5
fused	5.134 ± .007	7.98 ± .14	4.17 ± .01	73.3 ± 1.3
fused	5.445 ± .009	8.42 ± .11	4.397 ± .012	81.6 ± 1.1
fused	5.888 ± .011	9.08 ± .10	4.716 ± .013	94.4 ± 1.0
fused	6.285 ± .007	9.40 ± .10	5.023 ± .008	104.1 ± 1.1
fused	6.499 ± .010	9.73 ± .09	5.175 ± .011	111.0 ± 1.0

[a] Data obtained from streak camera records. All others obtained from duration of shock-induced luminescence in temperature shots.

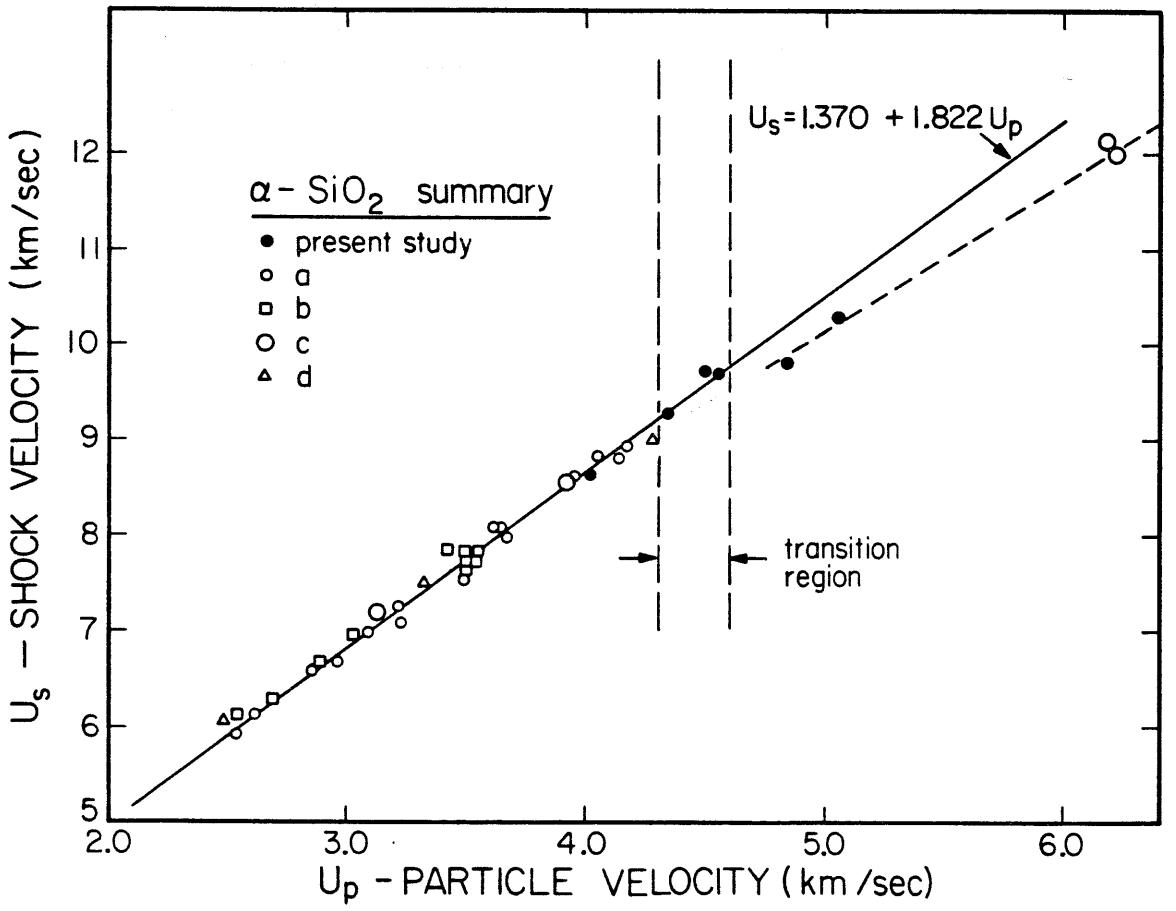

Figure 4-5. Summary of α-quartz Hugoniot data plotted in the particle velocity-shock velocity plane. Solid points are results from the present investigation. Separate linear fits are given for SiO_2 in the stishovite regime and for points above newly observed phase transition. Sources of data are [11]a, [6]b, [13]c, and [12]d.

This break corresponds to an approximately 2% discontinuous increase in density if it is real. It is of interest to note that if extrapolated back into the low-pressure region, the high-pressure fit would intersect the steeper low-pressure fit in the neighborhood of u_p = 3.5 km/s, corresponding to a shock pressure of about 70 GPa. This will be of interest later in considering the apparent nonequilibrium nature of the phase transition reported here.

Mg_2SiO_4 Experimental

Shock temperature experiments were carried out in the same manner as described above, using crystalline forsterite (Mg_2SiO_4) samples. Forsterite samples were cut from a single crystal boule grown by the Czochralski technique, and this material was the same as that used by Jackson and Ahrens [3]. Sample densities were measured by the Archimedean method to be 3.222 g/cm^3.

In the experiments carried out on Mg_2SiO_4 (Table 4-4), the samples used were approximately 3 mm in thickness and the shock was propagated along the (001) direction (parallel to the C-axis). The temperature uncertainties reflect the errors of measurement and errors in the least-squares fitting of the six spectral radiance values to mean values of emissivity and temperature, just as in the case of SiO_2. The pressure and temperature range of the data for forsterite (Figure 4-6), although relatively narrow, is in general agreement with the expected Hugoniot temperature on the basis of calculations (Ahrens *et al.* [15]).

As discussed in the following section, these temperature data, when compared with theoretical calculations, provide evidence that transformation

Table 4-4

Mg_2SiO_4 Shock Temperatures

Pressure (GPa)	Temperature (K)	Emissivity
153 ± 3	4490 ± 100	.66 ± .08
166 ± 3	4690 ± 100	.60 ± .06[a]
175 ± 4	4950 ± 100	.53 ± .03

[a] interpolated value

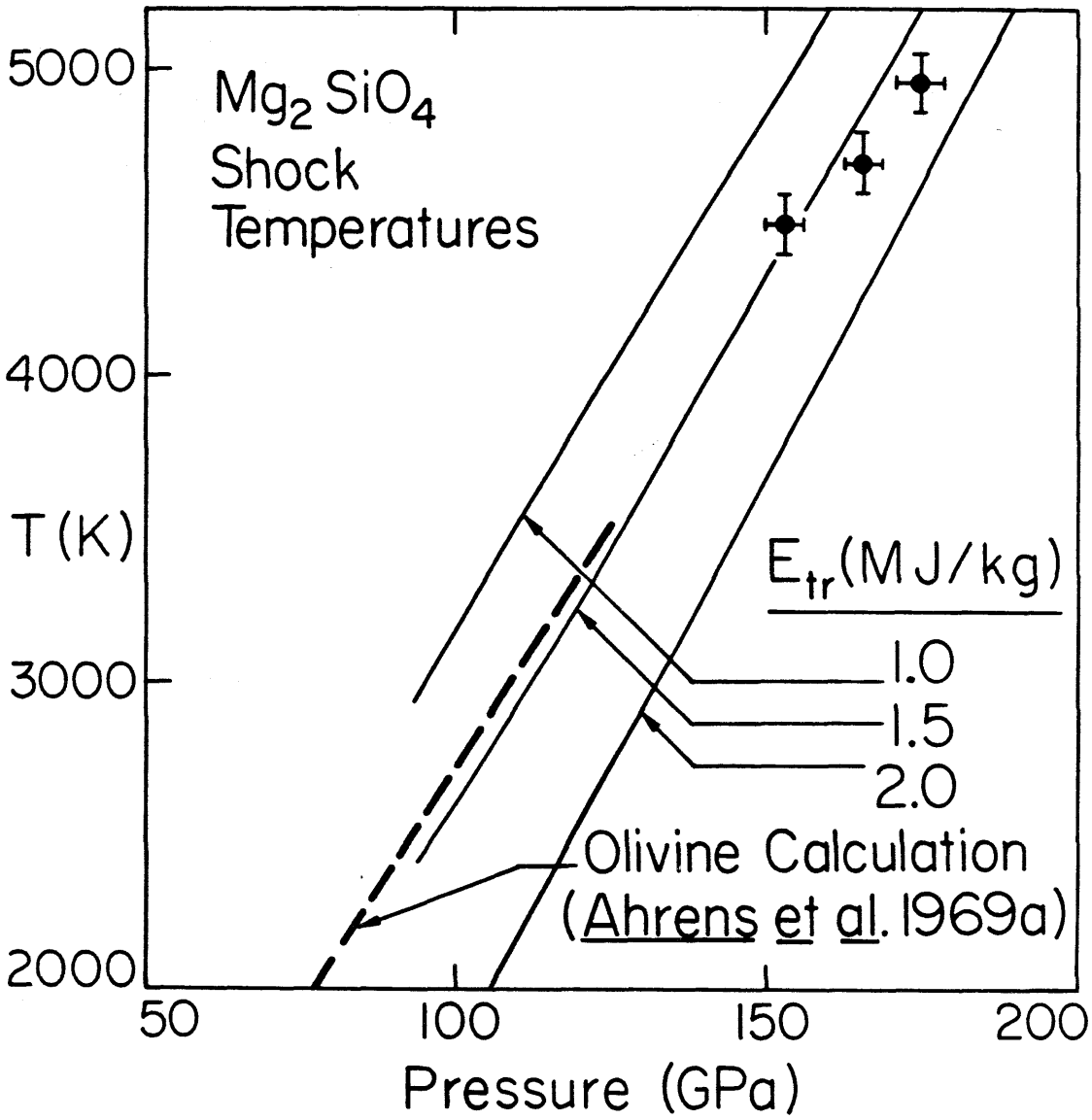

Figure 4-6. Measured and calculated shock temperatures versus pressure for forsterite. Calculations for three assumed values of the transition energy, E_{tr}, are shown.

to a dense polymorph or mineral assemblage does occur during the exceedingly short duration of the shock-wave experiment.

Interpretations

The present set of experiments suggest that the high-pressure phase of SiO_2, presumably stishovite, undergoes a shock-induced phase transition which is apparent in shock temperature data for both α-quartz and fused quartz Hugoniot states. Both sets of data display steep temperature declines with increasing pressure. Since the two negative sloping segments do not form a continuous curve, they probably do not represent an equilibrium phase boundary with a negative Clapeyron slope. The preferred interpretation is that the abrupt temperature drop is observed because the stishovite phase is metastable, at least on the time scale of the shock rise time, throughout what would otherwise be the mixed phase region of the Hugoniot curve. Finally, at the pressure of completion of the phase change, the material abruptly absorbs the latent heat of transition, entering the high-pressure phase all at once. This interpretation allows the phase line to be drawn by connecting the temperature minima in the two data sets, as has been shown in Figure 4-7. This phase boundary appears to have a small but positive slope, and this, taken with a positive entropy change estimated from the temperature drops to be of order R per mole of atoms, implies that the transition is accompanied by a modest volume increase.

This observation is not inconsistent with the apparent volume decrease seen in the Hugoniot pressure-volume data above 117 GPa. This is because the volume decrease corresponds to the sudden change from the relatively incompressible metastable stishovite to the more compressible stable phase.

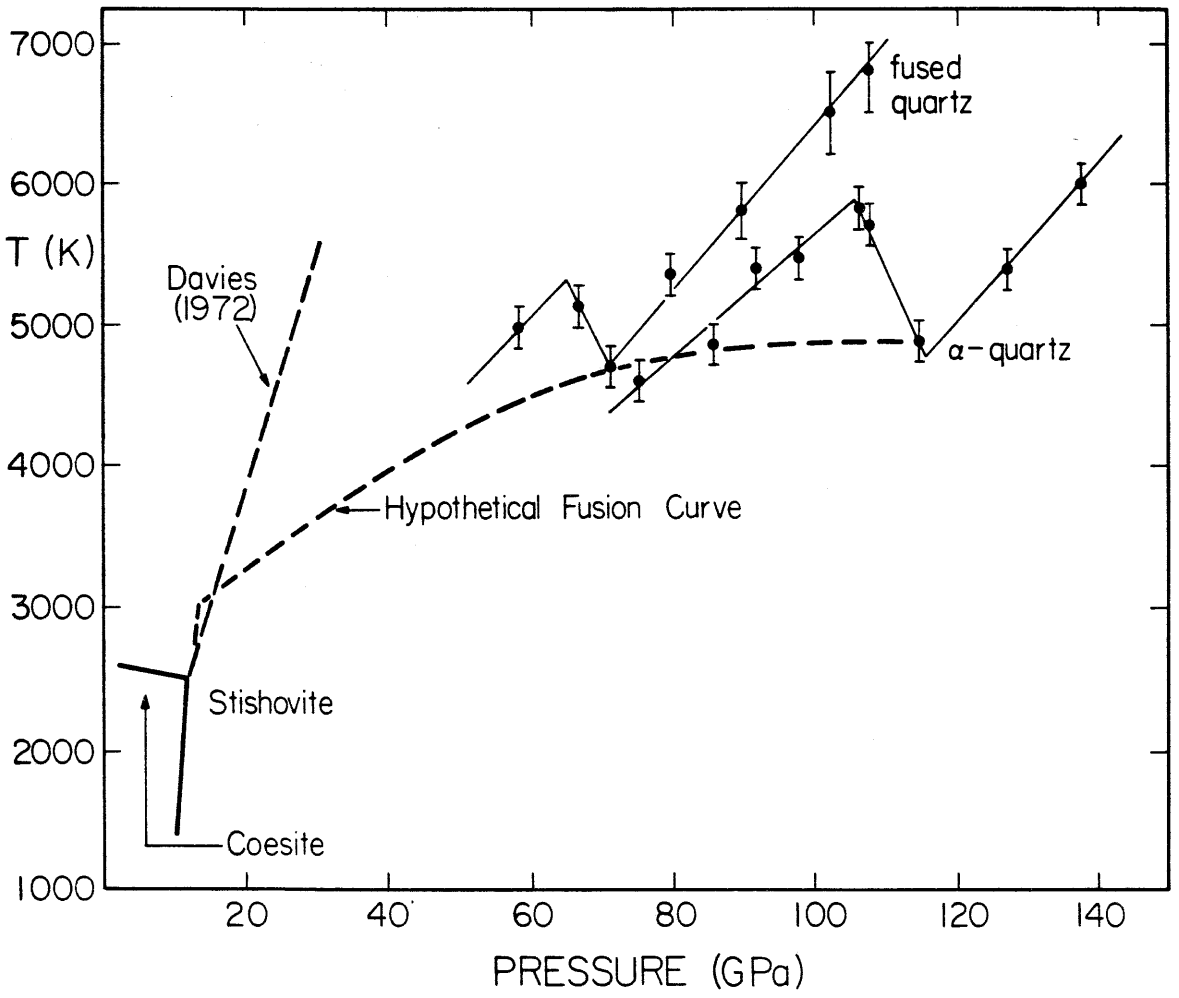

Figure 4-7. SiO_2 Hugoniot temperatures and pressures and the SiO_2 phase diagram. Proposed phase boundary between stishovite and liquid phase is drawn through temperature minima, assuming that superheating of the solid occurs in the shock wave. The coesite-stishovite-liquid triple point is estimated from Jackson [33]. Stishovite melting line of Davies [32] also shown.

Indeed, as pointed out earlier, if the transition were not overdriven, but occurred in equilibrium at all pressures, the extrapolated upper branch of the $u_s - u_p$ Hugoniot in Figure 4-5 would join the stishovite branch continuously at about 70 GPa pressure, which is approximately the pressure at which the observed Hugoniot temperatures first cross the proposed phase boundary.

To summarize the characteristics of the transition seen here, it is apparently accompanied by a small decrease in density, a fairly large positive latent heat, and an apparent increase in the compressibility along the Hugoniot upon completion of the transition. These results are all consistent with the identification of the transition with melting. Stishov [16] has shown that, for simple solids, the entropy of fusion is expected to be of order R per mole of atoms in the limit of high temperature and pressure. Furthermore, it has been well established, for example by Duvall and Graham [8], that equilibrium shock-induced melting should appear in the Hugoniot data only as a change in slope similar to that seen in the SiO_2 data interpolated for equilibrium transition conditions. The parameters of the melting transition may be estimated by computing theoretical Hugoniot temperature curves for the liquid phase and comparing them to the experimental results for α-quartz and fused silica.

The calculations of Hugoniot temperatures in this work were performed using the following method. The adiabat of isentropic compression $P_s(V)$ of the phase of interest is obtained through numerical solution of the equation,

$$\frac{dP_s}{dV} = \frac{dP'_H}{dV} + \frac{\gamma}{V}\frac{d}{dV}\left(\frac{V}{\gamma}\right)(P'_H - P_s) + \frac{\gamma}{2V}\left[(V_0 - V)\frac{dP'_H}{dV} - P'_H - 2P_s\right]. \qquad (4)$$

Here, P'_H and V_0 refer to the "metastable Hugoniot" of the phase in question (solid or liquid stishovite) centered at S.T.P. conditions. This metastable Hugoniot is derivable from the principal Hugoniot as described by McQueen et al. [17] and depends upon the magnitude of the transition energy E_{tr} at standard conditions.

In the present work, an interpolation formula was fit to the metastable Hugoniot, and (4) was solved for $P_s(V)$, the isentrope. Given $P_s(V)$, the shock temperature T_H was found at various values of V through solution of

$$\int_{T_s}^{T_H} C_v dT = \frac{V}{\gamma} (P_H - P_s) \qquad (5)$$

where now P_H is the principal Hugoniot pressure, and T_s is the temperature on the isentrope at specific volume V.

Unfortunately, the computed shock temperatures of the liquid (stishovite) prove to be insensitive to the assumed value of the Grüneisen parameter, $\gamma = V\,(\partial P/\partial E)_v$ because of the lack of a constraint for a liquid isotherm. For the liquid state, a nominal value of $\gamma = 0.6$ was used.

The computed temperatures are sensitive to the assumed model for the specific heat, C_v. In the case of the solid phase calculations shown in Figures 4-2 and 4-3, the results were obtained using a specific heat model which has the classical 3R value at low temperatures and rises due to anharmonicity as the melting temperature is approached. The 3R value is exceeded by 10% at the melting temperature of 4800 K in this model. Specifically, the solid heat capacity, adapted from the data collected by Grover [18] is

$$C_v = 3R[1 + 0.1(T/T_m)^2], \quad (6)$$

where T_m is the melting temperature.

Figures 4-2 and 4-3 also include calculated Hugoniot temperatures for the liquid phase regions. The heavy curves labeled "A" employ a liquid specific heat model of the type also formulated by Grover for monatomic liquid metals. The specific heat formula used for curve "A" is

$$C_v = 3R[1 - .083(T/T_m - 1)], \quad (7)$$

and this curve fit requires a larger enthalpy for the metastable liquid than stishovite at standard conditions by an amount ~2.7 MJ/kg.

For both α-quartz and fused quartz, the slopes of the "A" Hugoniot temperature curves are not an optimum fit to the data. The calculated slopes are strongly influenced by the value of C_v. A larger value of C_v with a smaller energy difference at standard conditions gives a better fit. It must be noted, however, that the lower-than-expected temperature rise observed in the liquid may not be real. Kormer [19] showed that in ionic materials, as shock temperatures exceed 7000-8000 K, the measured brightness temperature of the shock front saturates, presumably due to shielding by electrons not in thermal equilibrium. Such problems are discussed below in connection with the time-dependence of these temperature records obtained at high pressure and should be kept in mind in the interpretation of these data.

The curves labeled "B" in Figures 4-2 and 4-3 were calculated using $C_v = 4.2$ R, and the standard energy of metastable 6-fold coordinated liquid was 0.5 MJ/kg higher than that of 4-coordinated amorphous silica. This value is much more in line with the energy difference between α-quartz and stishovite (0.8 MJ/kg), but the anomalously high specific heat is difficult

to explain on physical grounds. In the discussions that follow, models A and B will be referred to in calculations assuming these two possible behaviors of the liquid stishovite phase.

The Lindemann melting criterion is a semi-empirical theory of melting which predicts the volume dependence of the melting temperature on the basis of the amplitudes of atomic lattice vibrations. It can be used, with some qualifications, to estimate the trajectory of the melting line of a solid if the volume dependence of its vibrational spectrum is known. Grover [18] has shown that, for metals, the Grüneisen parameter γ for the solid phase adequately describes this dependence, and the Lindemann law in this formulation becomes

$$-(d \ln T_m / d \ln V) = 2\gamma - 2/3. \qquad (8)$$

This equation has been integrated for 3 values of γ, assuming the melting temperature T_m is known to be 4800 K at the volume corresponding to 117 GPa pressure in α-quartz. These computed melting curves are shown in Figure 4-8, along with the observed Hugoniot temperatures translated into the V-T plane. The α-quartz curve was obtained through the two-segment Hugoniot described above, and the density jump encountered in going from metastable solid to liquid accounts for the observed gap in the V-T plot. The fused quartz data, when viewed in such a plot, are much more compressed along the volume axis, presumably because of the greater thermal energy and the smaller contrast between the compressibilities of the liquid and solid phases in silica shocked from the low initial density of fused quartz. A fused quartz Hugoniot fit was derived from the work of McQueen et al. [6], Wackerle [11], Jones et al. [20] and the new points obtained from this study, given in Table 4-3. A two-segment linear fit was again used,

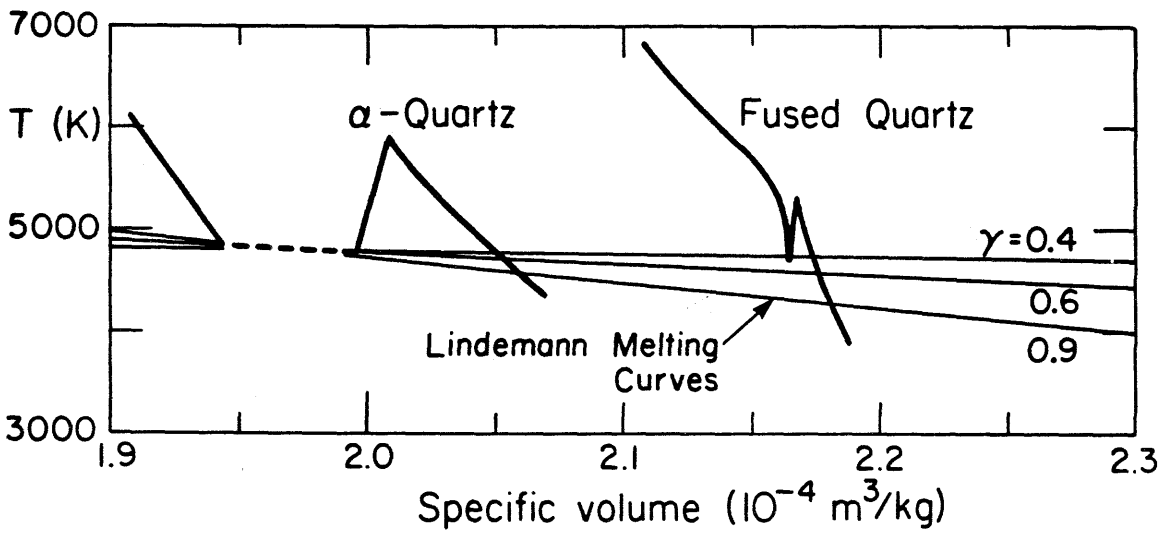

Figure 4-8. SiO_2 shock temperatures as a function of specific volume and theoretical melting curves calculated from the Lindemann criterion (Eq. 8). Hugoniot temperatures are transformed into the V-T plane using experimental P-V Hugoniot data. Discontinuities in the P-V data give rise to breaks in the temperature plot. Melting line calculations are based on assumed value of T_m = 4800 K along α-quartz Hugoniot.

but the quality of the data and the magnitude of the observed kink was not sufficient to make any definitive statement about density jumps or discontinuities due to transition overdriving. In the present work, McQueen's fit of

$$u_s = 1.861\ u_p + 0.211 \text{ km/s} \tag{9}$$

has been adopted below 86 GPa pressure, joining smoothly with a fit of

$$u_s = 1.568\ u_p + 1.538 \text{ km/s} \tag{10}$$

at high pressures.

It is apparent from Figure 4-8 that calculated Lindemann melting curves are in fairly good agreement with the observations, for values of γ in the expected range. The slope of the V-T melting line can be translated into the Clapeyron slope of the P-T phase line if we know the compressibility of the material along the equilibrium phase line. The equilibrium Hugoniot should coincide with the phase line in the mixed phase region, so that $(dP/dV)_H$ along the Hugoniot should approximate (dP/dV) along the melting line in the equilibrium case.

We can approximate this equilibrium Hugoniot in the case of α-quartz, by using the linear extrapolation of the liquid $u_s - u_p$ Hugoniot branch as discussed earlier. If the $u_s - u_p$ relation is given by

$$u_s = S\ u_p + C_0, \tag{11}$$

then the pressure-volume Hugoniot is

$$P = C_0^2 \frac{(V_0 - V)}{(V_0 - S(V_0 - V))^2} . \tag{12}$$

Differentiating this gives approximately the compressibility of α-quartz along the equilibrium melting line. Using $\gamma = 0.6$ in the Lindemann law, this gives a melting line slope of $dT_m/dP \approx 10$ K/GPa. If $\gamma = 0.9$ for solid stishovite, the slope is ~20 K/GPa. This result is in good agreement

with the estimated phase line in Figure 4-7.

Both the volume change and the latent heat of melting of stishovite at high pressures may be estimated using the present data. Figure 4-9 is a pressure-volume plot of the Hugoniot fits for α-quartz and fused silica, with their relations to the solid and liquid phase fields. In the case of α-quartz, the region of superheated solid is graphically illustrated adjacent to the dashed equilibrium Hugoniot, which spans the region of mixed phases. The mixed phase "band" is constructed by connecting the corresponding pressures of melting onset and completion along the two Hugoniot curves, as inferred from the shock temperature data. At 70 GPa pressure on the fused quartz Hugoniot where the melting point is first reached, the labeled quantity ΔV is the high-pressure volume change upon melting at constant T and P. The volume jump estimated in this way is approximately 0.08×10^{-4} m^3/Kg or 3.9%.

Next, the latent heat of melting may be estimated by comparing the energies of the solid on the melting line and liquid on the fused quartz Hugoniot at a pressure higher by amount ΔP. The latent heat is given by the difference between the Hugoniot energies E_H on the two curves, less the thermal energy corresponding to the pressure offset ΔP, and plus the $P\Delta V$ work done by the sample in melting at constant pressure. The latent heat is

$$\Delta H_m = (E_{Hf} - E_{H\alpha}) - \int_{T_\alpha}^{T_f} C_v \, dT + P_\alpha \Delta V, \qquad (13)$$

where subscripts f and α denote states on the fused quartz and α-quartz Hugoniots respectively. The results obtained here are $\Delta H_m \approx 3.8$ MJ/kg and 3.3 MJ/kg, assuming the above liquid models A and B respectively.

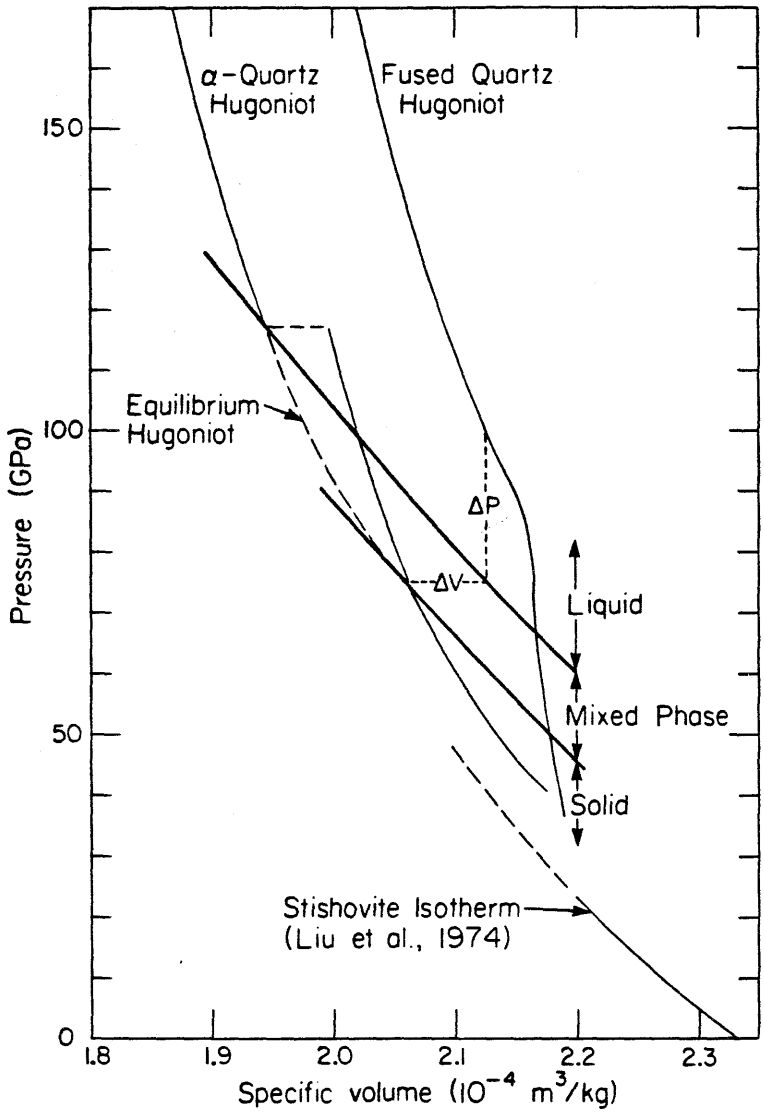

Figure 4-9. Pressure-volume Hugoniot curves for α-quartz and fused silica. Relation to liquid and solid stishovite phases is indicated by the heavy lines. ΔP is pressure offset between SiO_2 melted from α-quartz Hugoniot and fused quartz at same density. Liquid Grüneisen parameter γ is determined from this offset. Stishovite static compression data (Liu et al. [24]) are also plotted.

The calculated Clapeyron slopes are $(dT/dP)_m \approx 9$ K/GPa and 11 K/GPa, in agreement with the predictions of the Lindemann law as well as the experimental data. This latent heat corresponds to an entropy change of 1.8-2.0 R in general agreement with the systematics of Stishov [16].

While the Grüneisen parameter γ is not strongly constrained by the shock temperature data alone, an analysis of other available equation of state data yields considerable information about the thermal EOS dependence. γ is obtained by determining the finite difference approximation, $V(\Delta P/\Delta V)$ to the definition of $\gamma = V(dP/dE)_V$, between states in the same solid or liquid phase. Unfortunately, the regions of pure liquid or pure solid phase along the measured Hugoniot curves for α-quartz and fused silica do not overlap in volume, with the fused quartz Hugoniot lying everywhere at lower densities than the corresponding phase α-quartz Hugoniot. This makes it impossible to determine γ immediately from a comparison of the two Hugoniots, since as shown in Figure 4-9, in the region where they overlap, the fused quartz Hugoniot is in the liquid field, while the α-quartz Hugoniot at the same volume is in the solid stishovite field.

The Grüneisen γ for the liquid phase can be determined, however, from the magnitude of the pressure offset ΔP between the fused silica Hugoniot and the liquid state obtained by melting from the α-quartz Hugoniot, assuming ΔV is known. At a liquid specific volume of 2.155×10^{-4} m^3/kg, we find $\Delta P = 17.8$ GPa while the internal energy difference given by $\int C_V dT$ is 1.4 MJ/kg for model A and 1.9 MJ/kg for model B. Substituting into the Mie-Grüneisen equation, this gives

$$\gamma = V \frac{\Delta P}{\Delta E} \quad 2.0 \text{ (model B)} - 2.8 \text{ (model A)} \qquad (14)$$

for the liquid SiO_2 phase. This determination of γ is very strongly

dependent upon the assumed value of ΔV, and so has a large uncertainty (± 25% or more).

An independent check of this value for γ of the liquid phase may be obtained from an analysis of the decaying shock fused quartz experiment illustrated in Figure 4-4(a). As stated by McQueen et al. [17], the sound speed in states on the Hugoniot is

$$C_H = V \left\{ \left.\frac{dP}{dV}\right|_H \left[(V_0 - V) \frac{\gamma}{2V} - 1 \right] + P_H \frac{\gamma}{2V} \right\}^{1/2} . \qquad (15)$$

The subscript H denotes quantities evaluated on the Hugoniot at volume V. Since C_H is the velocity with which a rarefaction wave propagates with respect to the shocked material, knowledge of the time required for an overtaking rarefaction to reach the shock front allows a calculation of C_H and γ for the shocked state.

Figure 4-10 is an X-t diagram in which time increases vertically downward, and the horizontal direction represents the positions of target and impactor during the collision process. The trajectories of the shock waves and overtaking release waves may be seen schematically, and for the present case, the shock attenuation in the SiO_2 layer begins at a time dependent upon the SiO_2 rarefaction speed. The experimentally observed time of this event is approximately 250 ns after the shock enters the SiO_2, which requires the rarefaction to propagate at 19.2 km/s, or 14.4 km/s with respect to the material which is moving with particle velocity 4.8 km/s. Applying equation (15) to this result, $\gamma \approx 1.6 \pm 0.2$ for liquid SiO_2 at 97.5 GPa on the fused quartz Hugoniot. This general agreement with the previous determination of γ at a similar volume is reassuring for considering both the γ measurement, and the melting interpretation used above.

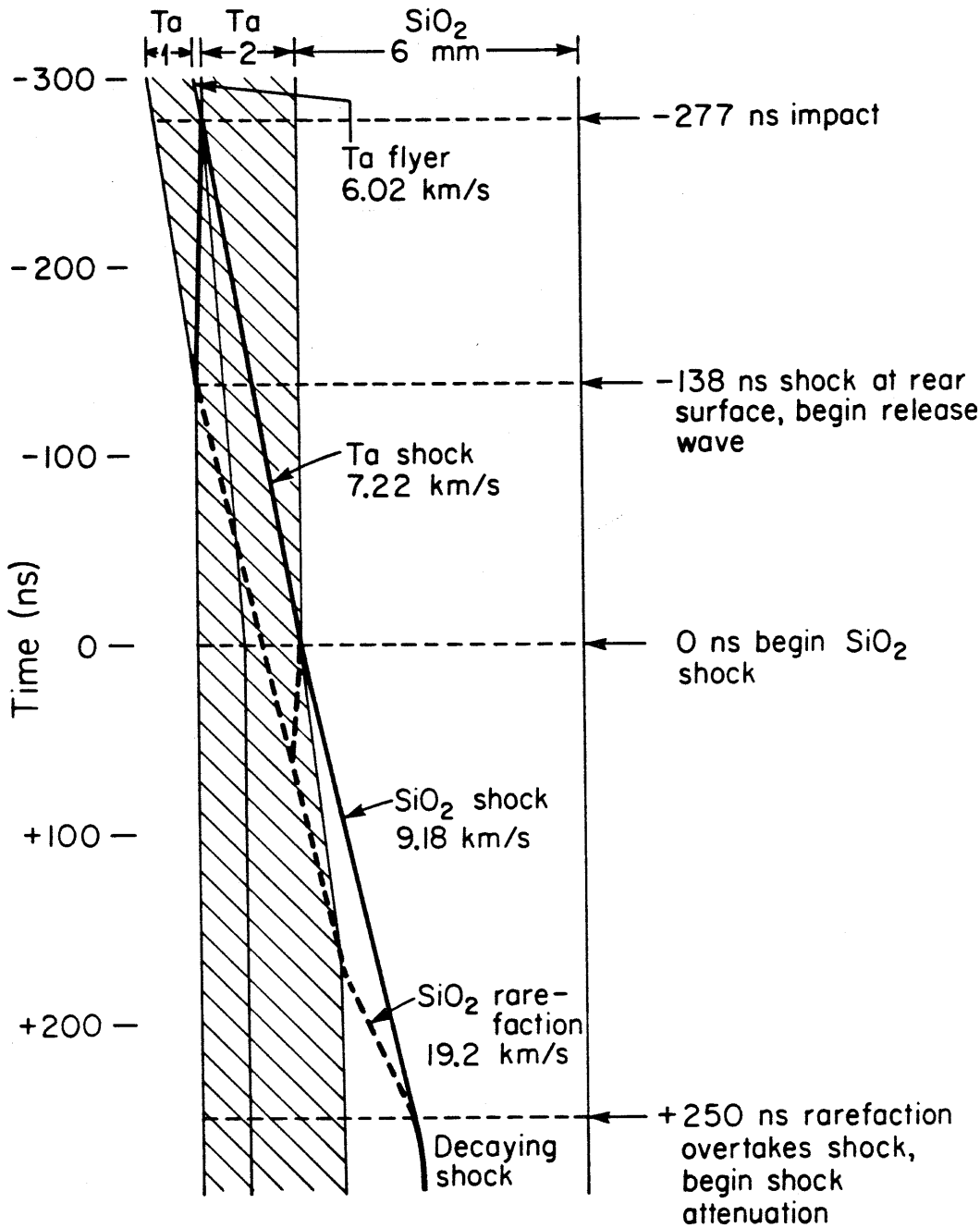

Figure 4-10. Graphical position-time representation of the decaying shock experiment shown in Figure 4-4(a). Determination of rarefaction wave velocity allows calculation of the Grüneisen parameter γ. Heavy lines are trajectories of shock waves in the tantalum driver and fused quartz sample. Dashed lines are release waves propagating at longitudinal sound speed.

The above calculations depend upon knowledge of the equation-of-state parameters of the tantalum flyer plate and base plate. Tantalum (density 16.66 g/cm^3) shock and sound velocities used here were calculated from the fit to the Hugoniot data

$$u_s = (1.298 \pm 0.012)u_p + (3.13 \pm 0.025) \text{ km/s} \qquad (16)$$

of Mitchell et al. [21], and assuming that the Grüneisen γ varies in direct proportion to V/V_0, with a zero-pressure value of 1.69 (Walsh et al. [22]). Uncertainties in these quantities affect the calculated value of γ for SiO_2.

The situation concerning the Grüneisen γ for solid stishovite is somewhat more difficult. The zero pressure thermodynamic Grüneisen parameter, given by thermodynamic identities as

$$\gamma_{th} = \alpha K_s/\rho C_p \qquad (17)$$

has been measured by Ito et al. [23] to be ~1.5. Above, α, K_s, and C_p are the volume coefficient of thermal expansion, adiabatic bulk modulus, and specific heat at constant pressure respectively. Liu et al. [24] have measured the isothermal compression of stishovite up to pressures of 23 GPa. While this range of compressions does not quite overlap the densities on the α-quartz Hugoniot in the stishovite regime, as seen in Figure 4-9, these data may be extrapolated a short distance (dashed curve) to obtain overlap with the α-quartz data near 40-50 GPa. The second-order Birch-Murnaghan fit obtained by Liu has been used for the fit, with bulk modulus and its pressure derivative equal to $K_0 = 335$ GPa and $K_0' = 5.7$ respectively. Using the pressure-energy offset between the Hugoniot and extrapolated static compression data, we find $\gamma \approx 0.9 \pm 0.1$ for stishovite

near a relative compression of 0.92. This value is in fairly good agreement with previous estimates of γ for stishovite, but difficulty is encountered in trying to check this against the α-quartz versus fused quartz offset, as done above for the liquid phase. This method is not applicable because uncertainties in the density on the fused quartz Hugoniot and the extreme steepness of the Hugoniot at lower pressures make estimates of pressure and energy offsets highly uncertain. Also, as noted for Figure 4-8, the melting transition along the fused quartz Hugoniot in this region may be less well defined than along the α-quartz curve. The calculation of γ for the liquid phase is not so adversely affected, since it makes use of the α-quartz and fused quartz Hugoniot curves where they are in well-defined single phases of relatively shallow slope, and where the magnitude of the measured offsets are large compared with their uncertainties.

The properties of the newly observed liquid phase of SiO_2, which presumably preserves approximately the six-fold coordinated nearest neighbor distribution of stishovite, can be summarized in order to characterize its complete equation of state. If the liquid γ and zero pressure volume V_0 are assumed known, the Hugoniot curve of "liquid stishovite" shocked from a hypothetical metastable S.T.P. state may be calculated after the manner of McQueen et al. [17]. By drawing analogy with the density difference between 4-coordinated and 6-coordinated crystalline SiO_2, we estimate the six-fold coordinated glass to have a zero-pressure density ~60% greater than fused quartz, corresponding to a specific volume of 2.8×10^{-4} m^3/kg. Performing the metastable Hugoniot calculations, a considerable volume dependence for γ is apparently required to obtain physically reasonable results. Using

a value of γ proportional to the square of relative compression or $\gamma \approx 3.0\ (V/V_0)^2$ yields a metastable Hugoniot with an extrapolated zero-pressure bulk sound speed of roughly 3-4 km/s and a bulk modulus of 6-coordinated glass in the neighborhood of 50 GPa. These values are clearly dependent upon the assumed zero-pressure specific volume and therefore are considerably uncertain.

These results characterize the properties of the high-pressure SiO_2 liquid phase and the melting of stishovite to this six-fold coordinated phase. It is interesting to note that studies of coordination in the silica analog system, GeO_2 (Sharma et al. [25]), indicate that the liquid in equilibrium with the 6-coordinated rutile phase is in four-fold coordination up to pressures of at least 1.8 GPa, well into the rutile stability field. While we find no clear evidence here for persistence of 4-coordination in liquid SiO_2 at stishovite pressures, this should be considered a possibility. It is interesting to note that the difficulty in recovering crystalline stishovite from shock compression of fused quartz is explained by the fact that the Hugoniot curve chiefly occupies the liquid field. The observed permanent densification of fused silica in such experiments (Wackerle [11]) may be related to a coordination increase in the liquid, although densification has not been seen at pressures higher than ~50 GPa.

Table 4-5 summarizes the results which have been obtained or which are consistent with the present data pertaining to stishovite and its six-fold coordinated liquid analog. It should be noted that the properties of the liquid phase at metastable S.T.P. conditions are rough estimates, intended to give agreement with the experiments, but are by no means uniquely determined.

It is appropriate at this point to discuss some of the limitations of

Table 4-5

SiO_2 High-Pressure Properties

Solid Stishovite	
α-quartz centered Hugoniot:	$u_s = 1.822\ u_p + 1.370$ km/s (±2%)
Metastable zero-pressure volume:	$V_0 = 2.333 \times 10^{-4}$ m^3/kg
Bulk modulus:	$K_0 = 335$ GPa
Grüneisen parameter:	$\gamma \approx 0.9$
Liquid Phase (6-coordinated)	
α-quartz centered Hugoniot:	$u_s = 1.619\ u_p + 2.049$ km/s (±1.5%)
Metastable volume:	$V_0 \approx 2.8 \times 10^{-4}$ m^3/kg
Bulk modulus:	$K_0 \approx 50$ GPa
Grüneisen parameter:	$\gamma \approx 3.0\ (V/V_0)^2$
Specific heat:	$C_v \leq 3R$ (model A) (eqn. 7)
	$C_v \approx 4.2$ R (model B)
Melting Transition (at 70 GPa pressure)	
Melting temperature	$T_m = 4400$ K ± 5%
Melting line slope:	$dT_m/dP = 10$ K/GPa ± 5
Volume change on fusion:	$\Delta V/V \approx 0.04$
Latent heat of fusion:	$\Delta H_m = 3.5$ MJ/kg ±15%

the current experimental technique and the assumptions which are implicit in the interpretations discussed here. Perhaps the most crucial issue in this regard is the question of the source of the observed blackbody radiation and whether that source is truly representative of the Hugoniot state as claimed. Experimental evidence suggests that the light observed in these experiments originates in a thin layer near or coincident with the shock front. The chief evidence for this is the extremely rapid (<5 ns) rise and fall times observed for the radiation, which would not be observed if the light source were distributed throughout a larger volume of the sample. These observations are in apparent conflict with those of Kormer [19] in which substantially longer rise times were seen in shocked alkali halides. Those earlier observations were done, however, at lower pressures and with less time resolution than the current studies, so that the disagreement may not be significant. Subsequent experiments using the present apparatus with NaCl samples have produced signals qualitatively identical with the SiO_2 results reported here (Chapter 3).

In addition to the very shallow (<50 μm) depth of the light-emitting region, the mechanism for light emission is unusual as well. Shock temperature measurements in forsterite indicate that below a sharp threshold pressure or temperature (in that case $T \sim 4000$ K) the efficiency of the radiating mechanism decreases sharply and the material behaves as a transparent dielectric with insignificant emissivity. This suggests that the source of radiation may have a thermal activation threshold. The source may be in the region of intense lattice deformation and defect generation within the shock front, and the high metal-like emissivity would be ascribable only to this narrow zone of material with disturbed

electronic states, while material some distance behind the front relaxes to a "normal" electronic state.

If the radiation originates in the shock front, immediate doubt is raised concerning the degree of thermal equilibrium between the light source and the bulk material of interest behind the shock. Electronic temperature equilibrium in the presence of defect states is expected to be achieved on a quite short time scale (10^{-9} s). As long as the thermal equilibrium between the material in the final compressed state and the radiating region is maintained, the observed radiation temperatures are reliable. Since the rise time of pressures and lattice deformation on the shock front is probably a few orders of magnitude shorter than the 1 ns temperature equilibration time, we may infer that the observed temperatures correspond to lattice temperature for the final states achieved in times shorter than 1 ns. If the final state takes longer than this to equilibrate, the observed temperature may not follow the final Hugoniot state. This may be the explanation for the observed superheating of SiO_2 above the melting temperature. It is reasonable to conclude that shock compressed silica required longer than 1 ns to form a mixed phase assemblage of solid and partial melt.

The foregoing discussion assumes that the properties of the radiating shock front are constant in time. While this is nearly true in most experiments, some notable exceptions occur. Figure 4-4(b) and the results of McQueen *et al.* [6] illustrate that near the pressure of transition from solid temperatures to liquid temperatures, the radiation region may "oscillate" between the two phases, and a complicated transition between purely solid temperatures and purely liquid temperatures may occur.

Furthermore, at the highest pressures (and temperatures) observed in fused quartz and to some degree in α-quartz, the nearly constant intensity during shock transit is replaced by signals, which still begin abruptly but then rise more slowly, apparently approaching an asymptotic value several percent higher, on a time scale of a few hundred nanoseconds. This time-dependent evolution of the shock structure suggests that care must be taken in using those temperatures, and while an effort has been made to determine the final asymptotic temperature, large uncertainties for the high-pressure fused quartz data have been quoted to reflect this problem. Kormer [19] pointed out in his study of shock temperatures in alkali halides that at the highest investigated pressures, corresponding to Hugoniot temperatures $\gtrsim$ 7000 K, the measured brightness temperatures fail to rise as rapidly as expected with increasing pressure, eventually "saturating" at some value. Kormer ascribed this behavior to high concentrations of shock-produced free electrons which form an opaque screening layer in a time shorter than that required for thermal equilibration with the ions. Subsequent experiments on NaCl using the present pyrometer (Chapter 3) suggest an association between this screening effect and the onset of the time-dependent "ramp" effect in the luminescence records. This may indicate that the observed small rate of shock temperature increase with pressure, which is particularly evident in the liquid data at the highest temperatures, may be an effect of radiation screening, rather than the true Hugoniot temperature. If this is the case, liquid model A should more accurately describe the true behavior than model B with its large specific heat, required to explain the low temperature slopes.

One final issue regarding the source of the shock-induced radiation

has to do with the question of heterogeneous yielding and temperature deposition in quartz. Several investigators (e.g., Neilson et al. [26]; Grady [27]) have discussed the localized heating and luminescence which occurs in narrow "shear bands" when α-quartz is shock loaded at relatively low pressures. This behavior is observed at pressures well below the stishovite pressure regime, but not in the presently investigated range. If heterogeneous heating occurs in a sample, optical pyrometry will generally yield an erroneous temperature, characteristic only of the localized "hot spots" and not the bulk sample.

While this behavior is not expected to persist through the extremely high pressures and phase transitions of these experiments, an effort has been made to search for this effect. Figure 4-11 is a reproduction of a streak camera record from an α-quartz equation-of-state experiment at 106.5 GPa pressure. The record presents a time history of the light emerging (or reflected) from a strip across the back surface of the target. As the image of this slit is swept down across the cathode ray tube recording screen, the onset and termination of shock luminescence is clearly seen during shock wave transit through the SiO_2 sample. The inclination of the observed shock arrivals is due to tilt of the impacting flyer plate with respect to the target. Within the resolution of the photographic record, the light intensity is spatially uniform and constant throughout the record. The faint dark vertical lines are scan line artifacts from the image converter tube face. If temperature inhomogeneities exist at all, they must be on a scale of microns or smaller.

Discussion of the shock temperature results from Mg_2SiO_4 experiments centers on the apparent transformation under dynamic compression to a

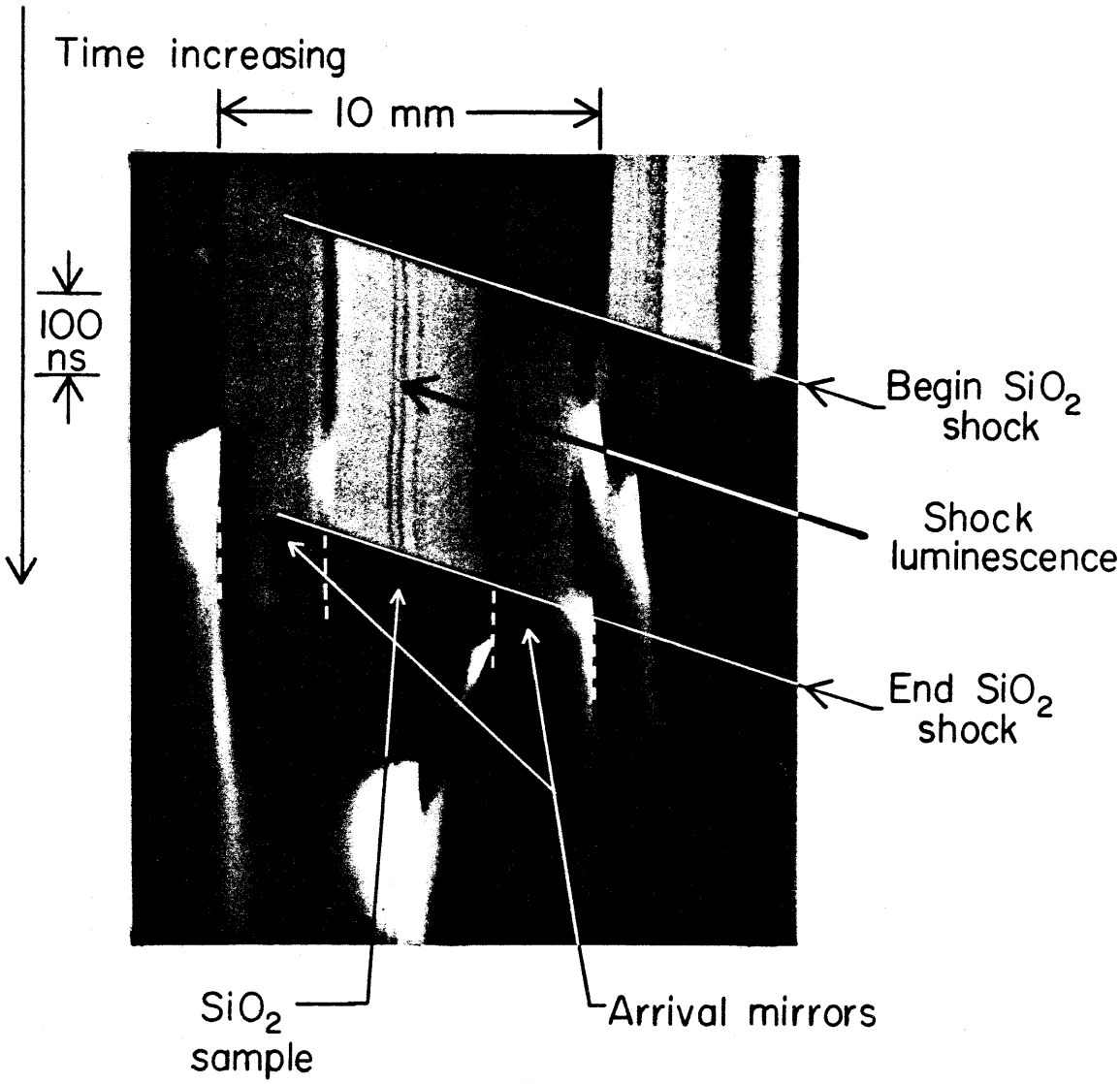

Figure 4-11. Image converter streak camera record of shock luminescence in α-quartz shock to 106.5 GPa pressure. Horizontal dimension is lateral distance across the sample face. In addition to determining shock velocity in sample, this photograph was intended to record any spatial or time variation in light intensity arising from local temperature inhomogeneities. No evidence of heterogeneous thermal distribution is detected.

denser polymorph, with an accompanying absorption of energy. The effect of this transition energy should be evident in the Hugoniot temperatures.

Shock experiments on single crystal forsterite carried out by Jackson and Ahrens [3] support the existence of shock-induced transformation to a high-pressure assemblage with a zero-pressure density of approximately 3.9 g/cm^3. Jackson and Ahrens could fit their data by assuming the olivine crystal structure changed to $MgSiO_3$ (perovskite) and MgO (periclase) or alternatively, mixed oxides, $2MgO + SiO_2$. They made estimates of $E_{tr} = 1.0 \pm 0.5$ MJ/kg and $\gamma = (1.5 \pm 0.5)\ \sigma^{1.5 \pm .5}$ where $\sigma = V/V_0^{hpp}$ is the compression relative to the hpp volume. Those values were used as starting models in fitting the forsterite data. The measured temperatures are consistent with theoretical calculations using $E_{tr} = 1.5 \pm 0.3$ MJ/kg. As in the case of SiO_2, the data do not constrain γ, but the above range of values are consistent with the measured temperatures, with the central value of the range $\gamma = 1.5\ \sigma^{1.5}$ giving the best agreement. Varying the volume dependence of γ through the volume exponent weakly varies the pressure-temperature slope, but does not strongly change the fit to the data. There appears to be some problem in exactly fitting the observed temperature-pressure slope, and further data will be required to determine whether this discrepancy is real. The slope centered on a pressure of 170 GPa is $(dT/dP)_H = 23$ K/GPa $\pm$ 7. In contrast, the range of values calculated by varying the volume exponent between zero and 2.0 is 34 K/GPa $^{+12}_{-1}$.

Conclusions and Implications

The observation of melting in stishovite at pressures near 1 megabar

(100 GPa), and the estimation of the latent heat of fusion have significant implications for the state of this mineral under conditions existing in the earth's lower mantle. Knowledge of the melting temperatures of candidate constituents of the mantle allow constraints to be placed on the geotherm in the solid mantle and further allow the estimation of such quantities as creep viscosity which may have a temperature dependence which scales with the melting point.

Kennedy and Higgins [28] have made arguments concerning the melting temperature of mantle material using a simplified model of this material as a binary eutectic system with MgO and SiO_2 as end members. If the melting temperature of the pure substances is known at the pressure of interest, the liquidus temperature of the idealized mantle material should lie at lower temperatures. Kennedy and Higgins further argue that the depth of the eutectic minimum at low pressures should be a lower limit to the depth of the trough at high pressures. Applying this reasoning to SiO_2, with a melting temperature of 4800 K, the solidus temperature of the hypothetical binary system should be no higher than about 3500 K. This estimate is based upon the 1305 K difference between the lowest observed melting temperature in the SiO_2 (quartz)-MgO(periclase) system (1820 K) and that of periclase (3125 K) the estimated low-pressure melting point of stishovite, following the reasoning of Weertman [29].

Another estimate of the mantle melting temperature may be made using the SiO_2 high-pressure latent heat of fusion in an elementary melting point depression calculation (Slater, [30]). In the approximation that mole fractions X of MgO solute in SiO_2 form an ideal noninteracting dilute liquid solution, then the depression of the SiO_2 melting temperature

is given by

$$T_m(0) - T_m(X) = \frac{RT_m^2(0)}{L_m} X \qquad (18)$$

for small values of X. L_m is the latent heat. The coefficient of X in the case of high-pressure SiO_2 is approximately 3500 K. This defines the initial slope of the liquidus curve and independently suggests that the depth of the eutectic trough should be at least ~1600 K, again placing a limit to the solidus temperature in the neighborhood of 3000 K to 3500 K.

These results indicate that in order for a silica-bearing mantle to be solid at pressures near the core-mantle boundary, the temperature must be at or below ~3500 K. A final issue in the discussion of these SiO_2 results and their geophysical importance pertains to the creep viscosity of mantle minerals. A separate paper [31] discusses the impact the present SiO_2 melting curve estimate has upon estimates of creep viscosity, based upon melting point systematics. In general, the melting temperatures obtained in the present work imply that this viscosity is probably not a barrier to thermal convection in silica-bearing mineral assemblages, under the conditions of pressure, temperature, and strain rate prevailing in the earth's mantle.

Finally, the new Mg_2SiO_4 shock temperature data are in good agreement with previous calculations which assume a shock-produced phase with a zero pressure density of ~3.9 g/cm^3 and a heat of transformation of 1.5 ± 0.3 MJ/kg at standard conditions. This result indicates that such polymorphic transitions can occur in silicates on the time scale of shock experiments, although the possibility exists that the shock-synthesized high-pressure phase may retain only short-range order in a crystalline lattice.

REFERENCES

1. McQueen, R. G., J. N. Fritz and S. P. Marsh, On the equation of state of stishovite, J. Geophys. Res., 68, 2319-2322 (1963).

2. Liu, L., A fluorite isotype of SnO_2 and a new modification of TiO_2: Implications for the earth's lower mantle, Science, 199, 422-425 (1978).

3. Jackson, I., and T. J. Ahrens, Shock-wave compression of single-crystal forsterite, J. Geophys. Res., 84, 3039-3048 (1979).

4. Ahrens, T. J., Dynamic compression of earth materials, Science, 207, 1035-1041 (1980).

5. Jeanloz, R., and F. M. Richter, Convection, composition and thermal state of the lower mantle, J. Geophys. Res., 84, 5497-5504 (1979).

6. McQueen, R. G., J. N. Fritz and J. W. Hopson, High-pressure equation of state of SiO_2 (to be published) (1980).

7. Al'tshuler, L. V., Use of shock waves in high-pressure physics, Sov. Phys. Usp., 8, 52-91 (1965).

8. Duvall, G. E., and R. A. Graham, Phase transitions under shock-wave loading, Rev. Mod. Phys., 49, 523-579 (1977).

9. Robie, R. A., B. S. Hemingway and J. R. Fisher, Thermodynamic Properties of Minerals and Related Substances at 298.15 K and 1 Bar (10^5 Pascals) Pressure and at Higher Temperatures, 216-221, Government Printing Office, Washington, D.C. (1978).

10. Fowles, G. R., Attenuation of the shock wave produced in a solid by a flying plate, J. Appl. Phys., 31, 655-661 (1960).

11. Wackerle, J., Shock-wave compression of quartz, J. Appl. Phys., 33, 922-937 (1962).

12. Podurets, M. A., L. V. Popov, A. G. Sevast'yanova, G. V. Simakov and R. F. Trunin, On the relation between the size of studied specimens and the position of the silica shock adiabat, Izv. Acad. Sci. USSR Phys. Solid Earth, No. 11, 59-60 (1976).

13. Trunin, R. F., G. V. Simakov, M. A. Podurets, B. N. Moiseyev and L. V. Popov, Dynamic compressibility of quartz and quartzite at high pressure, Izv. Acad. Sci. USSR Phys. Solid Earth, No. 1, 13-20 (1971).

14. Lyzenga, G. A., and T. J. Ahrens, Shock temperature measurements in Mg_2SiO_4 and SiO_2 at high pressures, Geophys. Res. Lett., 7, 141 (1980).

15. Ahrens, T. J., D. L. Anderson and A. E. Ringwood, Equations of state and crystal structures of high-pressure phases of shocked silicates and oxides, Rev. Geophys., 7, 667-707 (1969).

16. Stishov, S. M., The thermodynamics of melting of simple substances, Sov. Phys. Usp., 17, 625-643 (1975).

17. McQueen, R. G., S. P. Marsh and J. N. Fritz, Hugoniot equation of state of twelve rocks, J. Geophys. Res., 72, 4999-5036 (1967).

18. Grover, R., Liquid metal equation of state based on scaling, J. Chem. Phys., 55, 3435-3441 (1971).

19. Kormer, S. B., Optical study of the characteristics of shock-compressed condensed dielectrics, Sov. Phys. Usp., 11, 229-254 (1968).

20. Jones, A. H., W. M. Isbell, F. H. Shipman, R. D. Perkins, S. J. Green and C. J. Maiden, Material property measurements for selected materials, Report NAS 2-3427, 56 pp., General Motors Material and Structures Laboratory, Warren, Michigan (1968).

21. Mitchell, A. C., W. J. Nellis and B. L. Hord, Tantalum Hugoniot measurements to 430 GPa (4.3 Mbar) (abstract), Bull. Am. Phys. Soc., 24, 719 (1979).

22. Walsh, J. M., M. H. Rice, R. G. McQueen and F. L. Yarger, Shock-wave compressions of twenty-seven metals. Equations of state of metals, Phys. Rev., 108, 196-216 (1957).

23. Ito, H., K. Kawada, and S. Akimoto, Thermal expansion of stishovite, Phys. Earth Plan. Int., 8, 277-281 (1974).

24. Liu, L., W. A. Basset and T. Takahashi, Effect of pressure on the lattice parameters of stishovite, J. Geophys. Res., 79, 1160-1164 (1974).

25. Sharma, S. K., D. Virgo and I. Kushiro, The coordination of Ge in crystals and melt of GeO_2 composition at low and high pressures by Raman spectroscopy, Annual Report of the Director, Geophysical Laboratory 1977-1978, 665-672, Carnegie Institution, Washington, D.C. (1978).

26. Neilson, F. W., W. B. Benedick, W. P. Brooks, R. A. Graham and G. W. Anderson, Les Ondes de Detonation, edited by G. Ribaud, Editions du Centre National de la Recherche Scientifique, Paris (1962).

27. Grady, D. E., High Pressure Research: Applications to Geophysics, edited by M. Manghnani and S. Akimoto, 389-438, Academic Press, New York (1977).

28. Kennedy, G. C. and G. H. Higgins, Melting temperatures in the earth's mantle, Tectonophysics, 13, 221-232 (1972).

29. Weertman, J., The creep strength of the earth's mantle, Rev. Geophys., 8, 145-168 (1970).

30. Slater, J. C., Introduction to Chemical Physics, p. 289, McGraw-Hill, New York (1939).

31. Lyzenga, G. A., and T. J. Ahrens, Shock temperatures in SiO_2 and high-pressure equations of state (unpublished manuscript) (1980).

32. Davies, G. F., Equations of state and phase equilibria of stishovite and a coesitelike phase from shock-wave and other data, J. Geophys. Res., 77, 4920-4933 (1972).

33. Jackson, I., Melting of the silica isotypes SiO_2, BeF_2 and GeO_2 at elevated pressures, Phys. Earth Plan. Int., 13, 218-231 (1976).

Chapter 5

SHOCK TEMPERATURE MEASUREMENTS IN H_2O

Introduction

Water (H_2O) has been the subject of various dynamic compression studies extending continuously to pressures over 100 GPa, and in a few experiments (Podurets *et al.* [1]) to pressures of ~1.4 TPa. The equation of state of water at high pressures and temperatures is of interest in a wide variety of technological applications, in addition to its importance to geophysical problems such as the interiors of the major planets and satellites. Shock wave studies of various molecular fluids including H_2O have been undertaken at Lawrence Livermore Laboratory [2] in an effort to characterize the thermal equation of state and its dependence upon the microscopic states of the constituent molecules. That work on H_2O enlarged upon earlier results [3,4] obtained in high-explosives experiments at different pressures.

In the current investigation, the newly developed six-wavelength shock pyrometry technique has been employed to determine Hugoniot temperatures in water in the range of pressures accessible to light-gas gun experiments. Shock temperature experiments carried out jointly with Lawrence Livermore Laboratory have explored pressures between approximately 50 and 80 GPa. The results presented here allow an evaluation of the Mie-Grüneisen equation of state for liquid H_2O, consistent with the results of previous experiments in H_2O states off the Hugoniot. As with

experimental results presented elsewhere in this thesis, a more detailed compilation of measured spectral radiance data appear in Appendix II.

Experiments

The present series of H_2O shock temperature experiments was carried out through the incorporation of a few modifications of the technique described in Chapter 2. Most of these modifications were those required to accommodate and contain a liquid sample. Figure 5-1 shows the liquid target assembly. A transparent rear window of single crystal sapphire (Al_2O_3) allowed thermal radiation to escape from the shocked water sample, while the remaining optical path was identical to the other experiments. The metallic base plate in each shot was composed of high purity aluminum (alloy 1100), with a thickness of 2 mm. The water sample chamber, incorporating a 3-4 mm shock propagation distance, was filled with high purity deionized water through the indicated fill tubing. A bubble-free sample was obtained by evacuating and repeatedly flushing the chamber with pure water. The target assemblies were impacted by gun-launched tantalum flyer plates at impact velocities between 4.9 and 6.7 km/s. A copper-constantan thermocouple was attached to the aluminum body of each shot target, in order to provide a measurement of the water sample temperature and thus, an accurate determination of the initial state density.

Figure 5-2 illustrates a typical experimental record of emitted thermal radiation, as shown previously for other sample materials. The initial portion of the intensity record is qualitatively similar to the results obtained with solid samples, with a nearly constant "plateau" of sample radiance during the period of shock wave transit. Unique to this experimental configuration is the terminal portion of the record, as the

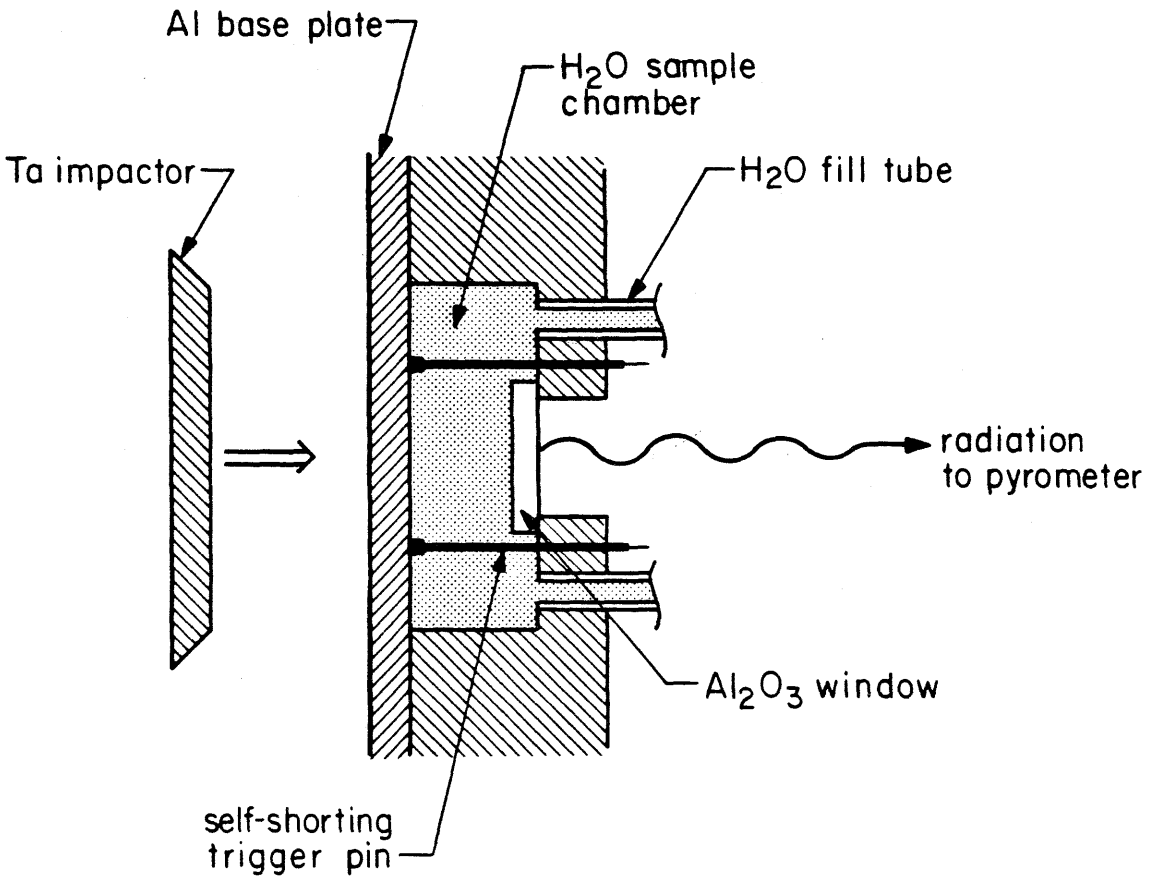

Figure 5-1. Schematic cross section of the liquid water target assembly. Impact driven shock is transmitted to water sample through aluminum base plate. Sapphire (Al_2O_3) crystal radiation window forms rear wall of H_2O chamber. Shorting pins provide trigger pulses for pyrometer diagnostics upon shock arrival in H_2O layer. Shock travel in water is 3-4 mm during ~400 ns.

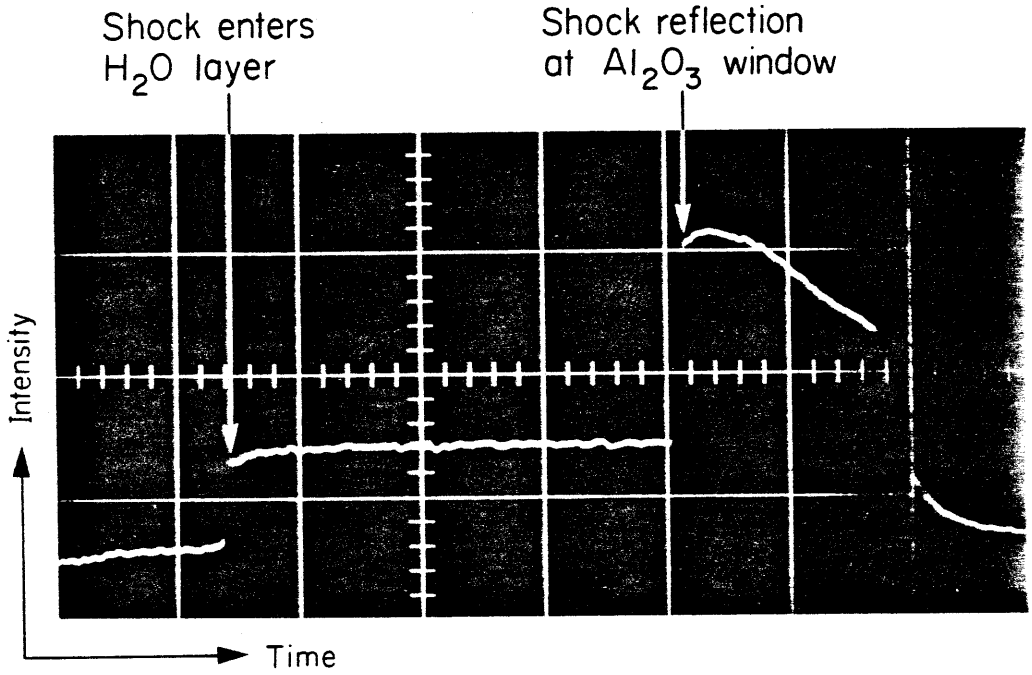

Figure 5-2. Typical light intensity record from H_2O shock temperature experiment. Shock transit through water layer displays constant thermal radiation output. Shock reflection from Al_2O_3 window is accompanied by abrupt brightness increase. Record is for H_2O shock pressure of 61 GPa. Horizontal time base scale is 100 ns per division.

shock wave encounters the Al_2O_3 window. Since Al_2O_3 is a material with a higher shock impedance than water, a second shock of higher amplitude is reflected back into the sample, so that an increase in light intensity rather than a decrease is observed at the end of shock transit in the water. The reported values of shock temperature are obtained from the plateau intensity. The measured intensities in the doubly shocked state are not, however, constant in time; therefore, no attempt is made here to derive temperatures for the second shock. This time-dependent behavior may be due to heat diffusion at the sample/window interface, rarefaction wave interactions, relaxation in the H_2O emissivity, or a combination of these. While double shock temperatures have not been obtained, these records can provide a supplementary measurement of shock velocity in the sapphire anvil and thus, as described below, an approximate determination of pressure and density in the doubly shocked state.

Table 5-1 summarizes the results of four successful shock temperature shots in H_2O, listing the temperatures and emissivities for each value of Hugoniot pressure. As in the investigations of other materials, the Hugoniot pressure-volume states were determined from a measurement of the impactor velocity and previous knowledge of the Hugoniot curves of the target and projectile materials. For the present investigation, linear fits to the shock velocity-particle velocity Hugoniots for these materials were used, as computed from the Livermore data by W. J. Nellis [private communication]. The Hugoniot for H_2O is given by

$$u_s = 1.332\ u_p + 2.396 \text{ km/s}; \quad \rho_0 = 0.998 \text{ g/cm}^3. \tag{1}$$

This description is assumed valid for $2.5 \text{ km/s} \leq u_p \leq 7.0 \text{ km/s}$. In calculations for states with $u_p < 2.5$ km/s, a second linear fit was

Table 5-1

H_2O Experimental Results

H_2O shock pressure(GPa)	Shock density (g/cm^3)	Temperature T_H (K)	Emissivity ε (±.07)	H_2O reflected shock state: Pressure (GPa)	H_2O reflected shock state: Density (g/cm^3)
49.0	2.262 ± .012	3510 ± 150	0.44	59 ± 6	3.40±1.0
61.0	2.354 ± .015	4190 ± 150	0.67	127 ± 8	3.70±.26
70±1	2.38 ± .05	4780 ± 150	0.52	---	---
78.5	2.462 ± .019	5390 ± 150	0.71	172 ± 8	3.47±.15

used, joining continuously with (1) at $u_p = 2.5$ km/s, and with a zero-intercept equal to the sound speed in H_2O of $u_s(0) = 1.483$ km/s.

Similarly, the aluminum Hugoniot is assumed given by

$$u_s = 1.300\ u_p + 5.530 \text{ km/s}; \quad \rho_0 = 2.715 \text{ g/cm}^3. \tag{2}$$

Here, the linear fit is valid for $1.9 \leq u_p \leq 5.0$ km/s. Finally the tantalum Hugoniot describing the impactor shock state is that of Mitchell et al. [5],

$$u_s = 1.298\ u_p + 3.313 \text{ km/s}; \quad \rho_0 = 16.66 \text{ g/cm}^3. \tag{3}$$

Each of the above Hugoniot fits is based upon measurements with approximately 0.5% absolute uncertainty in u_s.

Figure 5-3 illustrates graphically the impedance match method which has been employed to determine the water Hugoniot states. Since pressure and particle velocity are continuous across material interfaces in a shocked configuration, the P-u_p plane gives a convenient representation of shock wave interactions, with the common states between material layers in contact given by the intersection points of their P-u_p adiabats. As illustrated schematically, the Hugoniot locus of a tantalum flyer moving with initial velocity W crosses the Hugoniot of the aluminum base plate (at rest) at a common pressure and particle velocity of P_1 and u_1. As the aluminum shock reaches the H_2O layer, which is of lower impedance, the aluminum undergoes partial release along the path shown, reaching a pressure and velocity (P_2 and u_2) corresponding to the transmitted shock on the H_2O Hugoniot. A common approximation, which in the present case of aluminum has been justified to an accuracy of a few tenths of one percent [2], is the representation of the release adiabat in the P-u_p plane by the mirror-reflection of the Hugoniot curve through the line $u_p = u_1$. Under

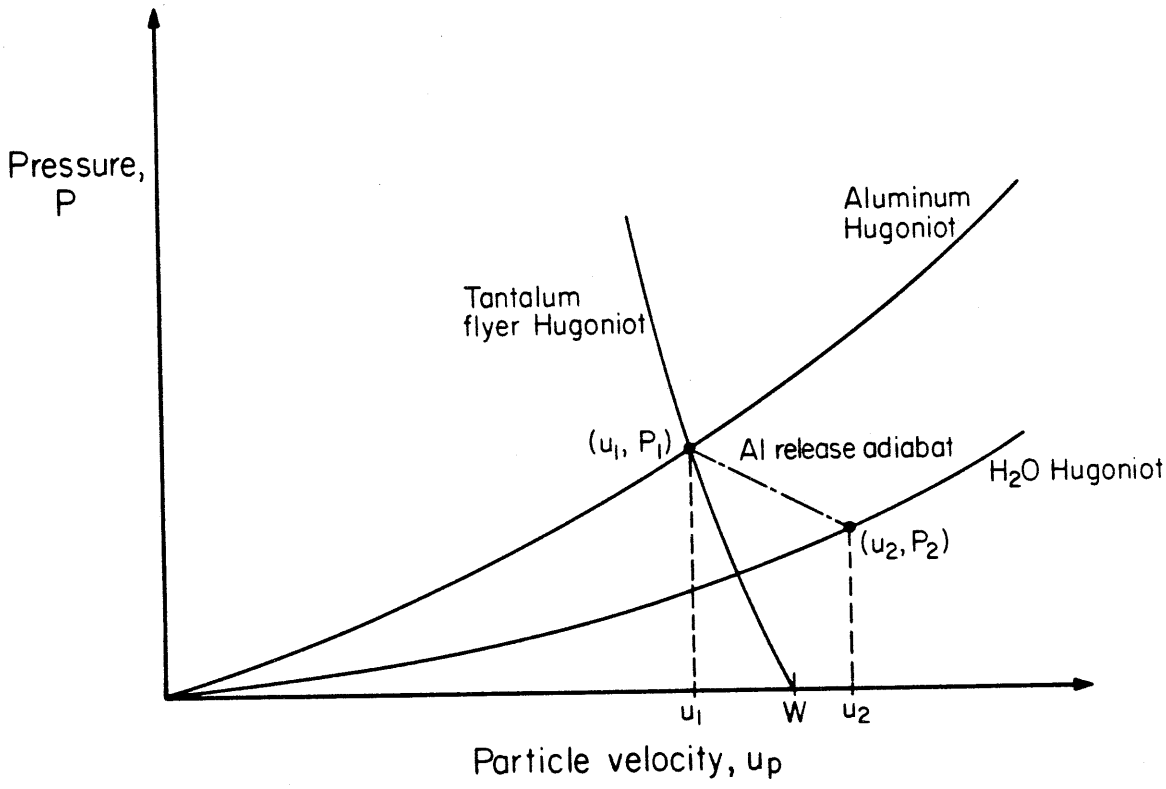

Figure 5-3. The shock impedance match construction in the pressure-particle velocity plane. The locus of P-u_p shock states in a tantalum flyer decelerated from initial velocity W is shown intersecting the aluminum Hugoniot (at rest) in the state (u_1,P_1). The aluminum release curve is constructed by reflecting the Hugoniot in $u_p = u_1$. The aluminum release curve intersects the water Hugoniot in the H_2O shock state (u_2,P_2).

this assumption, it is seen from Figure 5-3 that knowledge of the three pertinent Hugoniot curves allows P_2 and u_2 to be calculated from a measurement of W alone. Density and the other parameters of the shock-compressed H_2O state are then directly obtainable from the Rankine-Hugoniot equations (Chapter 1).

Similarly, the reported double shock states in Table 5-1 have been obtained from an impedance match solution with the Al_2O_3 anvil. The P-u_p state of the second shocked state is identical with the single shock state of the sapphire. This state is obtained from the known sapphire Hugoniot,

$$u_s = 0.934\ u_p + 9.075\ \text{km/s};\quad \rho_0 = 3.98\ \text{g/cm}^3, \tag{4}$$

fitted to the Livermore data compilation [6], and from the experimental measurement of u_s in the sapphire. Since errors in the determinations of density and particle velocity accumulate from the first shock state in the second shock state determination, the reported uncertainties are necessarily much larger in the latter.

As described elsewhere in this thesis, the reported values of Hugoniot temperature, T_H and emissivity have been calculated from the six independent spectral radiance measurements at different visible wavelengths for each shot. The relatively constant time history of radiation emitted from the sample is taken as evidence of its equilibrium character, in addition to the Planck distribution of its wavelength dependence. Table 5-1 shows monotonically increasing temperature with increasing shock pressure and, taking these values as the true shock temperatures, comparison may be made with the predictions of H_2O equation of state models.

Interpretations

Figure 5-4 shows the measured H_2O shock temperatures as a function of pressure, along with the results and calculations of earlier investigations. As indicated, a few lower pressure points were reported by Kormer [7], using the two-wavelength method described in the discussion of NaCl results (Chapter 3). A theoretical calculation of T_H was given by Rice and Walsh [3], based upon an assumed constant specific heat and a thermal equation of state derived from double shock experiments.

It is apparent that the results of the current investigation are in generally good agreement with the expectations for shock-compressed water, with no sign of the temperature anomalies which have been associated in shocked solids with first-order phase transitions to the liquid or denser solid phases. In detail, however, it is apparent that the measured values fall slightly below the trend of earlier calculations, based upon equation-of-state estimates made at substantially lower pressures.

The dashed curves of Figure 5-4 indicate the results of temperature calculations performed in the current investigation. The calculations followed the method outlined in Chapter 1 by computing the liquid water compression isentrope and then finding T_H from the pressure (and energy) offset between the isentrope and observed P-V Hugoniot. The input parameters for this calculation are the principal Hugoniot, the Grüneisen parameter $\gamma(V)$, and the specific heat at constant volume C_v. The Hugoniot used was the two-segment linear u_s-u_p fit discussed above. It should be mentioned that the actual isentropic compression process carried out on H_2O from S.T.P. conditions eventually carries it into one or more of the high-pressure solid ice polymorphs (see, for example, Kamb [8])

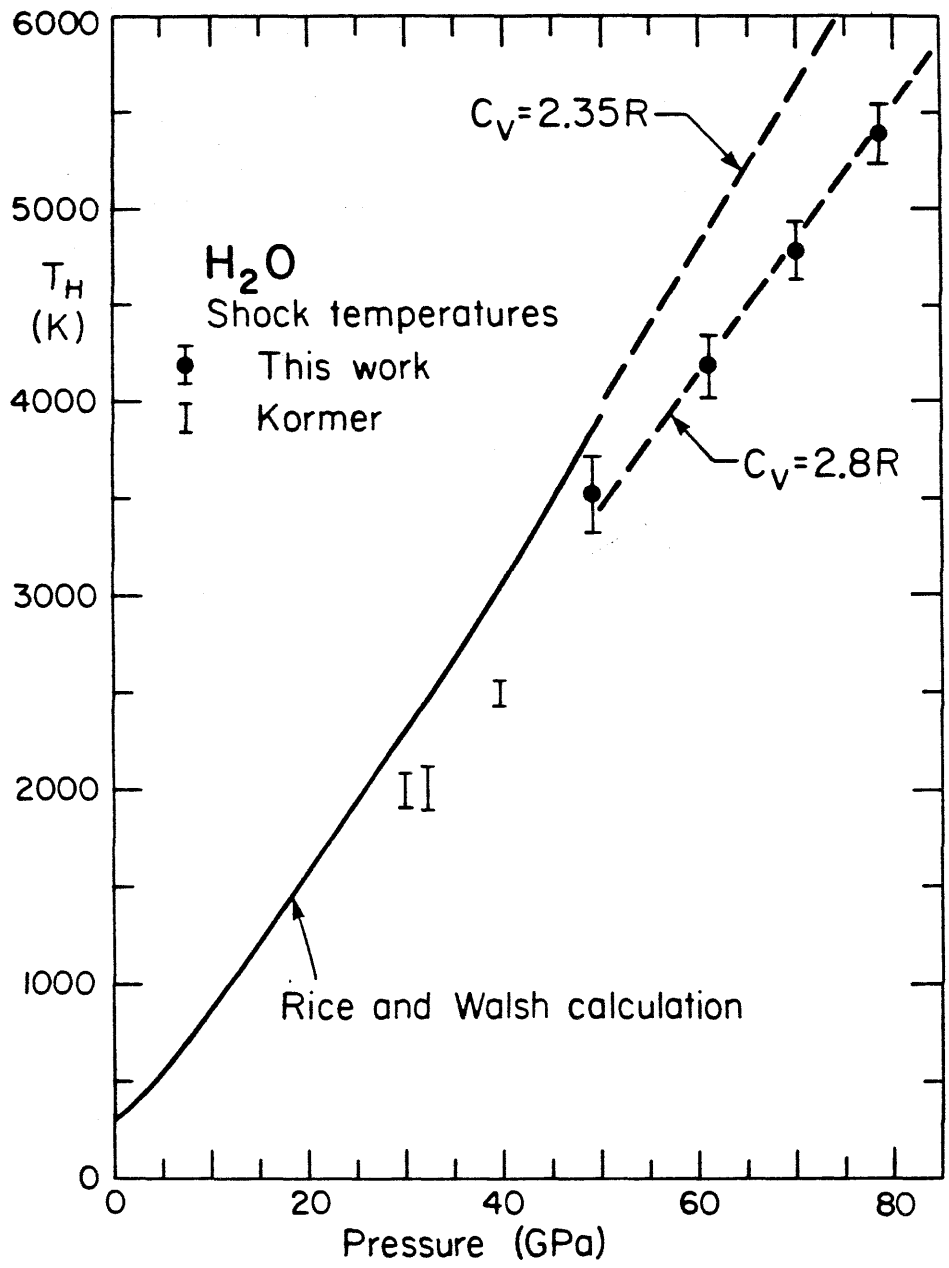

Figure 5-4. H_2O shock temperature data plotted as a function of pressure. Results of the current investigation are shown with those of Kormer [7]. Calculated Hugoniot temperatures are indicated for different specific heat models.

and that in fact the solid phase, ice VII has been observed upon doubly shocking liquid H_2O (Kormer [7]). Therefore, the liquid isentrope referred to here in theoretical calculations is a metastable curve, characteristic of the same liquid phase as seen along the principal Hugoniot, compressed in a hypothetical supercooled condition.

Another input parameter which has been taken from earlier work is $\gamma(V)$. The combined results of Gurtman et al. [9], Rice and Walsh [3], and Mitchell and Nellis [2] have been used to formulate a working Grüneisen γ. Where double-shock and other non-Hugoniot pressure-volume measurements exist at densities overlapping the measured Hugoniot, the pressure-energy offsets between these two data sets have been used to calculate γ from the Mie-Grüneisen definition,

$$\gamma = V\left(\frac{\partial P}{\partial E}\right)_V = V\,\frac{\Delta P}{\Delta E}\,, \tag{5}$$

where the second equality holds when the Mie-Grüneisen equation is valid. These results show γ to increase from a zero-pressure value of 0.5, passing through a maximum of ~1.5 near a compression $(V/V_0) = 0.6$. Thereafter, γ is observed to decrease rapidly with increasing density, dropping below 0.5 again at $(V/V_0) \approx .45$. The present calculations have used the approximate fit,

$$\gamma = 0.5(1 + 21.0\eta - 37.9\eta^2), \tag{6}$$

where $\eta = (1 - V/V_0)$.

As discussed in Chapter 4 in the cases of SiO_2 and Mg_2SiO_4, when the isentrope is not independently constrained in the theoretical temperature calculation, large variations in the assumed γ have very little effect on the computed temperatures. In the present case, temperature calculations using a constant $\gamma = 0.9$ yielded shock temperatures

essentially indistinguishable from the case of equation (6). While shock temperature measurements alone do not constrain γ effectively, experimental measurements can determine whether the Mie-Grüneisen model is generally a valid description of the material. Mitchell et al. [10] have observed the electrical conductivity of shock compressed water and have detected a plateau in the rapidly increasing trend of conductivity with rising shock pressure. This "saturation" of the electrical conductivity is coincident with the observed decrease in γ. In [10] speculation is raised that the ionization mechanism presumed responsible for the conductivity increase may also act as a sink of thermal energy, thus reducing available thermal pressure and the inferred value of γ. Such behavior would be expected to introduce a strong non-Grüneisen dependence (temperature dependent γ) in the thermal equation of state, in addition to a relative "softening" of the P-V Hugoniot. As shown below, evidence for these effects are lacking in the present data.

In Figure 5-4, the uppermost dashed curve is computed, assuming the same constant specific heat used in [9]. In that work, a value of $C_v \approx 3300$ J/kg-K was derived for liquid H_2O near a pressure of 2.5 GPa and assumed valid throughout the investigated range. This calculation gives excellent agreement with the calculation of Rice and Walsh, but gives temperatures everywhere several hundred degrees higher than the measured values. Several explanations for this deviation may be offered.

The first possible conclusion is that the specific heat C_v is underestimated in the calculation. At the temperatures considered here, electrons cannot play an important role in the heat capacity, so it is difficult to admit a specific heat larger than ~3R, the classical solid

value. Some value between this and the monatomic ideal gas value of 1.5R is more likely. The above assumed C_v is equivalent to ~2.35R, so that some room for increase in C_v is admissible. The lower dashed curve in Figure 5-4 shows that a very good agreement with experiment is obtained by simply assuming a constant $C_v = 2.8R$ (per mole of atoms). Such a modest change in the value of the specific heat of liquid water at high pressure appears quite reasonable and is presently favored as the simplest hypothesis required to explain all the present data.

Alternatively, the observation of shock temperatures somewhat lower than a priori calculations may be an indication of departure from ideal Mie-Grüneisen thermal behavior, in which thermal pressure at a fixed volume varies linearly with internal energy. This departure would presumably coincide with the hypothesized "ionization softening" proposed in [10].

In the case that γ is a function only of volume, the temperature difference ΔT between the Hugoniot and the isentrope at volume V is given by Mie-Grüneisen as

$$\Delta T = \frac{\Delta E}{C_v} = \frac{V\Delta P}{\gamma(V)C_v} , \tag{7}$$

where ΔP is the pressure difference between these states. If the Mie-Grüneisen assumption is not valid, this fact may be expressed by allowing a temperature dependence in γ. If this is the case, then (7) must be replaced by the equation

$$\int_{T_S}^{T_H} \gamma(V,T)dT = \frac{V\Delta P}{C_v} . \tag{8}$$

Temperature variations along the isentrope are, in general, small compared with those along the Hugoniot so that we may assume the hypothetical temperature dependence of γ to take the form,

$$\gamma(V,T) = \gamma_1(V) + \gamma_2(V,T), \tag{9}$$

where γ_1 describes the temperature independent behavior along the isentrope and γ_2 is zero on the isentrope and increasing in absolute value with distance from the isentrope as T increases.

In this case, (8) becomes

$$\gamma_1 \Delta T + \int_{T_S}^{T_H} \gamma_2 dT = \frac{V\Delta P}{C_v} \tag{10}$$

or equivalently,

$$\frac{V\Delta P}{C_v} = \Delta T(\gamma_1 + \frac{1}{\Delta T}\int_{T_S}^{T_H} \gamma_2 dT) = \Delta T(\gamma_1 + \bar{\gamma}_2). \tag{11}$$

Here, $\bar{\gamma}_2$ is the average value of the temperature dependent component of γ, over the temperature interval between T_S on the isentrope and T_H on the Hugoniot. It is interesting to note that if the temperature dependence of γ is completely separable from the volume dependence, as in

$$\gamma(V,T) = \gamma_1(V)[1 + \gamma_3(T)], \tag{12}$$

then the effect of $\bar{\gamma}_2$ in the temperatures predicted from (11) would be indistinguishable from a simple increase in C_v as proposed above.

This model of the observed shock temperatures in H_2O is not favored for a few reasons. First, the observed excursions in γ through the suspected range suggest that $|\bar{\gamma}_2/\gamma_1|$ should be large, of the order of unity. Since changes in the product γC_v of only ~20% are required to obtain agreement with experiment, invoking this effect may be unwarranted. Furthermore, the sign of the change in γ with increasing temperature that is required in (11) to explain the low temperatures is the opposite of that indicated by the drop in γ estimated from double shock experiments.

These observations, combined with the lack of evidence of any anomalous change in compressibility along the Hugoniot in the region of interest argue against the importance of temperature variations in γ. Of course, more complicated or subtle departures from the Mie-Grüneisen assumption cannot be precluded, but in light of the present data, invoking such behavior is evidently not required.

Finally, the possibility exists that temperature "saturation" analogous to the high-pressure effect seen by Kormer [7] in NaCl (Chapter 3) accounts for the slightly low observed temperatures and gradients. This explanation may be largely discounted on two grounds. First, the work done in the present research program on NaCl and SiO_2 has indicated that this radiation screening effect due to copious free electrons on the shock front is accompanied by a considerable time dependence in the observed radiation. The current H_2O experimental records, such as that reproduced in Figure 5-2, have displayed rather constant intensity during each experiment in the investigated pressure range, indicating that this effect has not yet become important. Secondly, in both the observations of Kormer and the present study, it appears that for a wide range of materials, the temperature threshold for onset of this screening effect is 7000-8000 K, well above the investigated range for H_2O.

In conclusion, the present experimental shock temperature measurements in liquid H_2O have provided a check on the thermal equation of state models determined for this material in previous dynamic compression experiments. The current results are consistent with the Mie-Grüneisen equation of state, requiring only modest changes in the specific heat of water from that observed at lower pressures, in the regime of static compression experiments.

These Hugoniot temperature data could provide even more rigorous constraints on γ and other parameters of thermal pressure variation in the presence of independent measurements of the water isentrope (or isotherm) at large compressions. While such measurements often present formidable problems for the presently available techniques of static compression, progress is currently being made in the development of dynamic methods to achieve isentropic compressions in low-density condensed materials like water, to pressures comparable with those achieved in Hugoniot experiments. The final chapter describes the results of an ongoing study of the feasibility of one such technique for isentropic compression.

REFERENCES

1. Podurets, M. A., G. V. Simakov, R. F. Trunin, L. V. Popov, and B. N. Moiseev, Compression of water by strong shock waves, Sov. Phys. JETP, 35, 375-376 (1972).

2. Mitchell, A. C., and W. J. Nellis, Water Hugoniot measurements in the range of 30 to 220 GPa, in High-Pressure Science and Technology, 1, 428-434, edited by K. D. Timmerhaus and M. S. Barber, Plenum, New York (1979).

3. Rice, M. H., and J. M. Walsh, Equation of state of water to 250 kilobars, J. Chem. Phys., 26, 824-830 (1957).

4. Skidmore, I. C., and E. Morris, in Thermodynamics of Nuclear Materials, p. 173, Intern. Atomic Energy Agency, Vienna, Austria (1962).

5. Mitchell, A. C., W. J. Nellis and B. L. Hord, Tantalum Hugoniot measurements to 430 GPa (4.3 Mbar) (abstract), Bull. Am. Phys. Soc., 24, 719 (1979).

6. Van Thiel, M., editor, Compendium of Shock Wave Data, Report UCRL-50108, Lawrence Livermore Laboratory, Livermore, California (1977).

7. Kormer, S. B., Optical study of the characteristics of shock-compressed condensed dielectrics, Sov. Phys. Usp., 11, 229-254 (1968).

8. Kamb, B., Structure of ice VI, Science, 150, 205-209 (1965).

9. Gurtman, G. A., J. W. Kirsch and C. R. Hastings, Analytical equation of state for water compressed to 300 kbar, J. Appl. Phys., 42, 851-857 (1971).

10. Mitchell, A. C., M. I. Kovel, W. J. Nellis and R. N. Keeler, Electrical conductivity of shocked water and ammonia, preprint UCRL-82126, Lawrence Livermore Laboratory, Livermore, California (1979).

Chapter 6

ISENTROPIC COMPRESSION FROM SHOCKS IN CONDENSED MATTER

Introduction

The earlier chapters have discussed the high-pressure equations of state of solids and liquids, focusing in particular upon those states on or near the Hugoniot, the locus of P-V-E states achieved through a single shock transition from standard conditions. While the examination of Hugoniot shock states offers considerable advantages in experimental measurements and in the range of accessible pressures (in some experiments, such as those of Ragan [1], as high as several tens of megabars), restriction of experiments to only these states neglects regions of potentially great interest in high-pressure research.

Shock waves of sufficiently large amplitude are expected finally to carry the investigated material into the region of high temperature and pressure in which the material is a high-density plasma, well described by the Thomas-Fermi statistical model (see, for example [2]). Such calculations become valid as the electronic shell structure of atoms becomes "smeared out" and the mean field description of T-F theory becomes accurate. Along the Hugoniot of most condensed materials, these conditions are satisfied when the pressure reaches ~50 Mbar and $T > 10$ eV. While equation-of-state information in this high-temperature regime finds direct application in astrophysical problems, as well as in

those natural and man-made processes which generate shocks of very large amplitude, the condensed phases of matter undoubtedly display a rich variety of phase relations and interesting properties at large compressions but low temperatures. While Hugoniot experiments are capable of producing extreme pressures, the accompanying strong irreversible shock heating effect prevents the desired high densities from being achieved.

This effect of shock-generated thermal pressure is most pronounced in materials of low initial density, since the degree of shock heating manifested in the Hugoniot internal energy, E_H is greater as the initial volume V_0 is larger. An extreme illustration of this fact is afforded by Hugoniot measurements on initially porous media. As discussed in the review of Al'tshuler [3], in such cases the density in shocked states on the Hugoniot can actually decrease with increasing pressure.

Unfortunately, many of the materials whose behavior in dense high-pressure phases are of most interest are those molecular crystals and fluids whose low densities at standard conditions make these interesting regions inaccessible to shock experiments. Liquid hydrogen is an example of such a substance. While shock compression data for H_2 exist [4], they provide only indirect information concerning the transition to denser phases such as the hypothesized metallic state transition. Hydrogen in solid or liquid metallic phases occurs along the compression isotherm and isentrope in the pressure range of several megabars, so that these phases assume great importance in the interior of Jupiter and the major planets. Additionally, such high-pressure transitions potentially have importance in technological applications. While the ultimate fate of all elements and compounds compressed at low temperature may be

metallization due to the pressure-induced closure of electron band gaps, the approach and accomplishment of this transition is an important aspect of solid state physics, whose observation at high pressure largely eludes present experimental techniques. While some observations may have recorded such transitions [5], refinement and development of new techniques to achieve large compressions at moderate temperatures are desired.

Experimental techniques which afford compression of specimens along their isentropes or isotherms generally require a longer time to achieve the final state than the quasi-discontinuous pressure jump of the shock front. Static isothermal compression experiments, employing diamond anvil presses have recently succeeded in reaching pressures in the range near 100 GPa (1 megabar), but accurate determinations of pressure and density are difficult to obtain. Pressure calibration standards for use in the rather small sample volume of uniform pressure present a significant problem, and density determinations via x-ray diffraction are generally restricted to high-Z materials with strong x-ray scattering ability.

Isentropic compression to megabar pressures has been the goal of investigations [6,7] using magnetic implosion apparatus. In these experiments, the magnetohydrodynamic pressure of an intense pulsed magnetic field is transmitted by a conducting shield to the investigated sample in a cylindrical geometry. The rise time of the pressure in a sample of a few centimeters dimension is many microseconds. This is a sufficiently long time that shock steepening does not occur within the sample, and the adiabatic compression is essentially isentropic. In an example of the application of this technique, Pavlovskii *et al*. [7] have reported on the compression of quartz (SiO_2) to over 100 GPa. That work suggests

the occurrence of a major volume collapse in SiO_2 near 125 GPa pressure to a presumably new high-pressure phase of density ~10 g/cm^3.

This observation is of particular interest in light of suggestions of the metallization of SiO_2 in isothermal compression [5] in the same general pressure range. While such observations generate much interest in the high-pressure behavior of silica, considerable uncertainty remains with the interpretation of pressure, density, and even electrical conductivity measurements in these experiments. Indeed, double shock experiments on SiO_2 performed in the course of the present research (Lyzenga and Ahrens, unpublished data) have failed to detect any major density changes in the indicated pressure range. Clearly, the large compressions achieved in isentropic experiments are necessary for the solution of this and similar problems, but improved techniques for the characterization of the high-pressure, high-density state are desirable.

Many of the experimental advantages of shock wave experiments result from their simple one-dimensional geometry. For this reason, the possibility of the conversion from plane-wave shock compression to isentropic compression is attractive. In principle, this conversion may be accomplished by one of two experimental strategies. As discussed in some theoretical treatments [8,9], in a medium whose initial density and acoustic properties vary continuously along the longitudinal direction, the shock wave amplitude may be observed to vanish, to be replaced by a more gradual (reversible) rise in pressure as the disturbance propagates along the gradient in material properties. Alternatively, isentropic compression may be approximated by the successive passage of multiple low-amplitude shocks through the sample. This technique may be thought

of as a generalization of the double shock experiment in which states of higher density than those on the Hugoniot are achieved by reflecting a first shock from a high impedance anvil. Multiple shock pressures at a given density approach the pressure on the isentrope as a limit when the final state is reached through an ever larger number of smaller individual shocks. Proof of this principle is straightforward, considering the graphical illustration of Figure 6-1.

As discussed in Chapter 1, the internal energy jump upon shock transition from a state (P_1,V_1) to (P_2,V_2) is given by

$$E_2 - E_1 = \frac{1}{2}(P_1+P_2)(V_1-V_2). \qquad (1)$$

This is just the area of the trapezoid in the P-V plane which is between the V-axis and the straight line segment connecting state 1 and state 2. As seen in Figure 6-1, the internal energy rise in a material which undergoes a series of successive shocks is given by the sum of the areas of the shaded trapezoids. In the limit of a large number of intermediate shocks, this sum approaches the integral, $\int PdV$. Since the internal energy of states on that locus is given by the external work integral, $\int PdV$ alone, that curve must be the isentrope (curve of constant entropy).

The current chapter is concerned with calculations which have been carried out to determine the degree of reversible compression that may be obtained in practically realizable experimental configurations, utilizing multiple shock interactions and material property gradients. These calculations have been carried out numerically, as increasing numbers of interacting waves rapidly make direct closed form shock propagation solutions impractical.

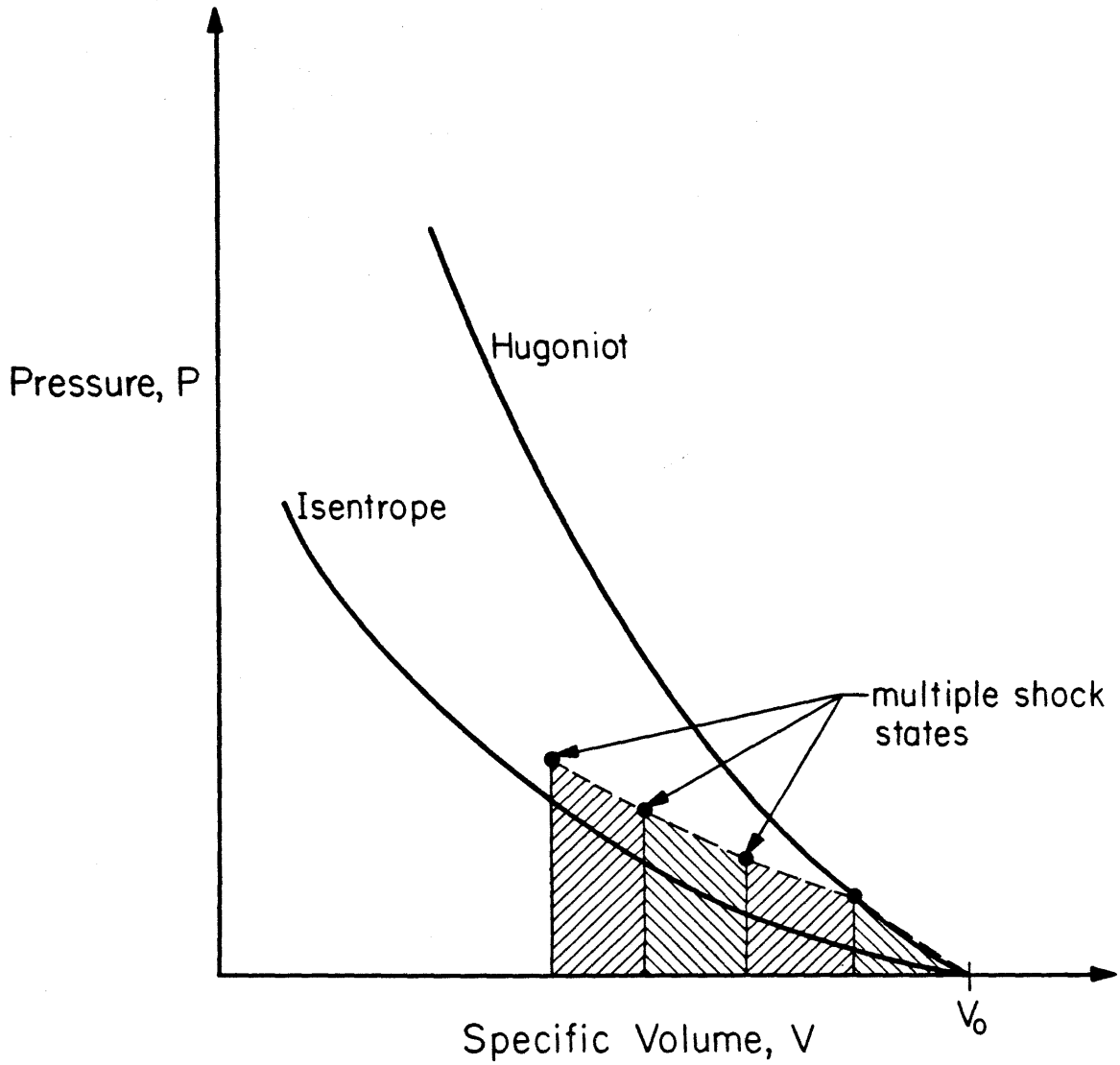

Figure 6-1. Multiple shock states in the P-V plane. As the number of successive shocks increases, the sample state approaches the isentrope. The internal energy increase in each shock is given graphically by the area of the shaded trapezoid.

Numerical Calculation Results

The current set of computer "experiments" investigating shock interactions and the approach to isentropic compression was carried out with the aid of a general purpose one-dimensional wave propagation simulation computer code. This code, WONDY IV, has been developed and documented by the Code Application Division of Sandia Laboratories, Albuquerque, New Mexico, and complete listings and instructions for the use of the program are given by Lawrence and Mason [10]. This program handles large amplitude (nonacoustic) wave propagation problems by solving the finite difference analogs to the Lagrangian equations of motion on a mesh of up to 1800 discrete mass elements in one spatial dimension. The steepening of shocks is stabilized through the use of an artificial viscosity term in the equations, which serves to spread the otherwise discontinuous shock front over several zones and retain the validity of the overall calculation.

While the program includes provisions for constitutive relations describing anistropic material strength effects, rate dependent and strain history dependent effects, as well as other specialized material properties, the current work has employed a strictly hydrodynamic description of the flow in the experiments described below. All the pressures of interest will be considerably above the yield strengths of the materials considered, and in the phenomena which are of interest in this investigation, the materials are subjected to compressive stress so that fracture and spall effects do not assume an important role.

Kompaneets et al. [8] showed that for a particular form of the Hugoniot equation of state, a gradient of initial density along the

propagation direction of a one-dimensional shock could effectively convert it into a wave of continuous isentropic compression. In that work, the density variation assumed is of the form

$$\rho_0 = \rho_{00}[1 - (m/m_0)^2]^{-1} . \qquad (2)$$

Here, m is a Lagrangian position coordinate, fixed in the moving mass of the medium and ρ_{00} is the reference initial density at $m = 0$. The results of Kompaneets show that while shock conversion is achieved with this gradient, full accomplishment of this desired state is not reached until a propagation distance of $\sim 0.7\, m_0$. Since $m = m_0$ represents a singularity in ρ_0, as m grows to the order of m_0, the initial density becomes a rapidly varying function of position.

This result is not unexpected, since large gradients in ρ_0 seem necessary to counteract the tendency for pressure pulses to steepen into shocks in materials of constant properties, after a propagation time of a few pulse rise times. Such a requirement however places heavy demands upon the experimental technique. Not only is it required that a sample be fabricated with as much as an order of magnitude variation in starting density over its width but diagnostic measurements of the state compressed at constant entropy can only be obtained during the final few percent of the wave propagation distance near the terminal free surface or interface, where reflected waves disrupt the measured state. Furthermore, diagnostic pressure and density measurements must be made in a region of large gradients in these quantities.

More varied behavior in the attenuation of the discontinuous shock front is reported by the same authors in [9]. By allowing both the initial

density ρ_0 and the sound speed C_0 to be functions of Lagrangian position m, a wide variety of shock behaviors is observed. By taking the assumed variations

$$\rho_0 = \rho_{00}[1 + \alpha m]^{-1} \tag{3}$$

and

$$C_0 = C_{00}[1 + \alpha m], \tag{4}$$

where α is a positive constant, a significant decrease in the degree of shock heating is observed after a propagation distance of approximately α^{-1}.

This observation formed the basis for the first exploratory computer experiments in the current program. Since the pre-existing WONDY code is designed to calculate flows in layers of constant initial properties, with the ability to accommodate up to 20 distinct layers or "plates," these calculations must approximate the continuous gradients discussed above with a series of constant "steps" through the medium.

Figure 6-2 shows the results of a calculation carried out for a stack of plates ~2 cm in thickness, in which the initial density of the hypothetical material varies monotonically from 3.5 g/cm^3 down to 1.3, while the sound speed C_0 increases from 5.0 to 13.5 km/s. The assumed reference Hugoniot equation of state was that given by Kompaneets et al. [8],

$$P_H = \left(\frac{C_0^2}{V_0}\right) \frac{(V_0 - V)}{(2V - V_0)} \tag{5}$$

while the thermal pressure variation was determined by a Grüneisen parameter taken to be $\gamma = 2$.

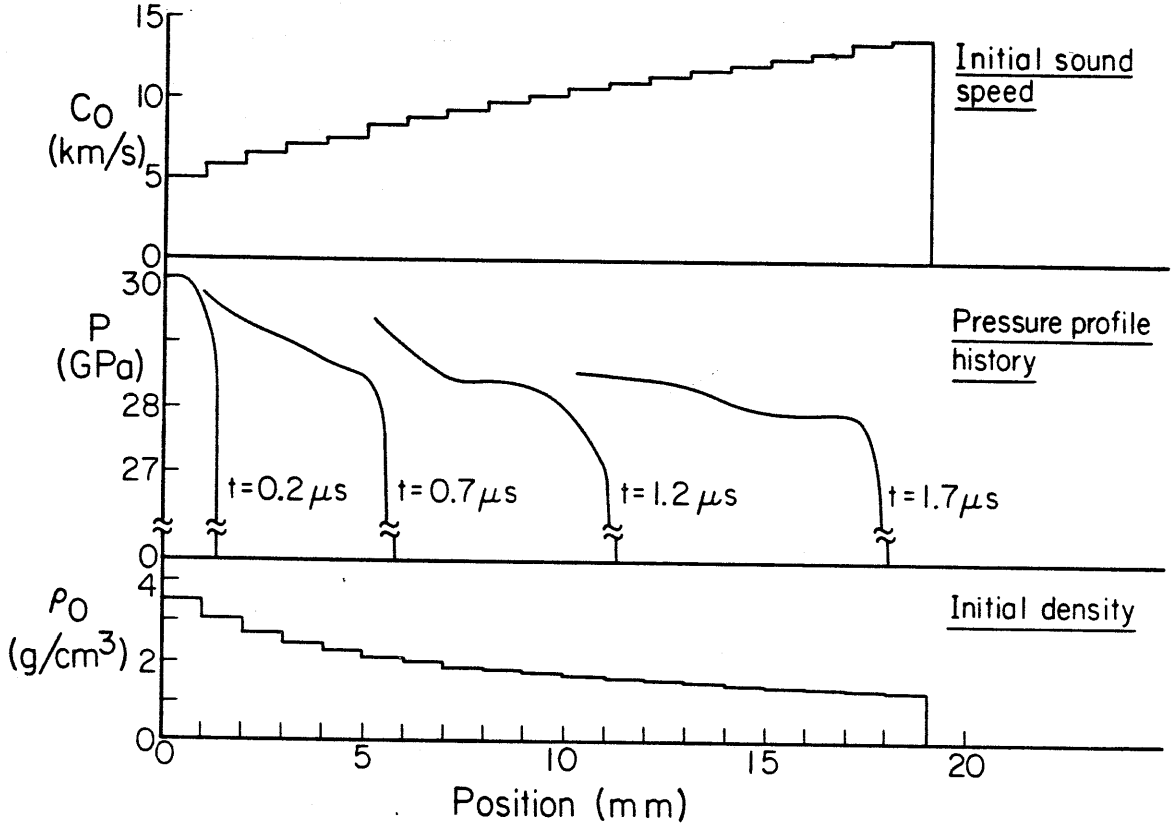

Figure 6-2. Shock wave conversion in a medium of variable acoustic properties. Decreasing density (bottom) and increasing sound speed (top) profiles are given. Wave pressure profile is illustrated at center as a function of position and time.

As Figure 6-2 illustrates, when a shock with an initial amplitude of 30 GPa enters the stack, the shoulder of the shock front becomes progressively smeared, as the magnitude of the discontinuous pressure jump drops. Toward the end of the shock travel, as the gradients in ρ_0 and C_0 begin to die out, evidence is seen for resteepening of the front as expected.

While in the illustrated case, scarcely a 10% reduction in the shock amplitude was achieved with initial property variations as big as 100%, the results are nevertheless encouraging and indicative of the direction in which progress might be made. It is possible, as will become apparent later in this chapter, that in many cases only a partial elimination of the shock transition in compression of condensed material can result in a proportionately much greater reduction in the net irreversible heating of the sample. With results such as those of Figure 6-2 in hand, it became apparent that additional progress might be made by considering experiments with large density and compressibility contrasts between layers, discarding the assumed connection with samples of smoothly varying density and of uniform composition.

Experimental precedent for this kind of approach already exists. Adadurov *et al.* [11] for example, have employed multiple shock reflections in layers surrounding an investigated sample of low shock impedance to elevate its pressure to ~50 GPa via approximately 10 successive small amplitude shocks, thus reducing the temperature rise upon compression from that of a single shock by a full order of magnitude.

The principle of this method can be illustrated in the simplified experiment of Figure 6-3. If a thin layer of investigated material is

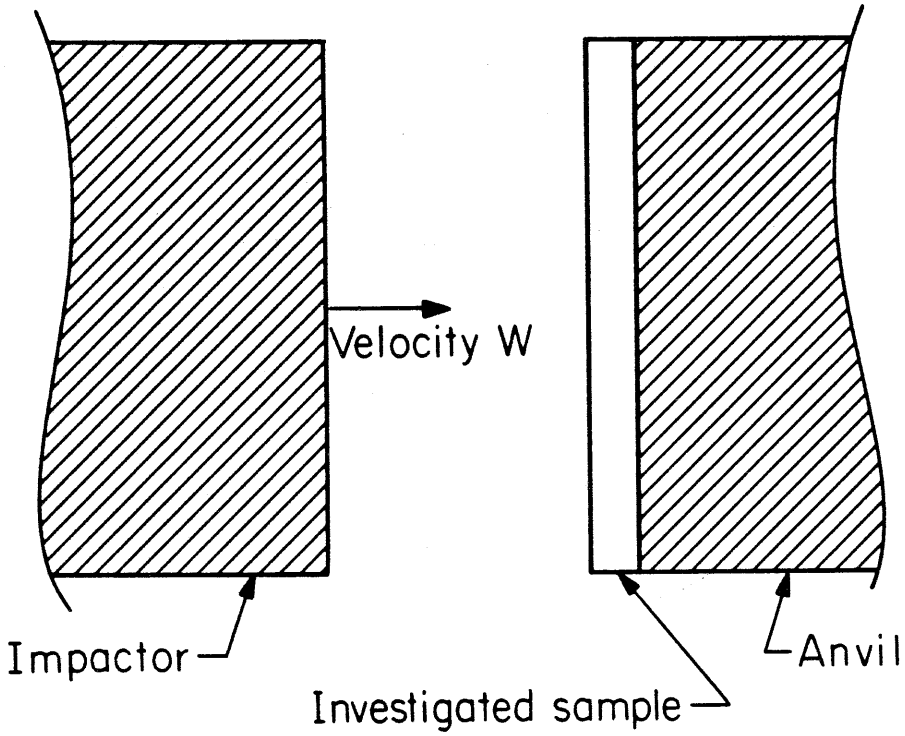

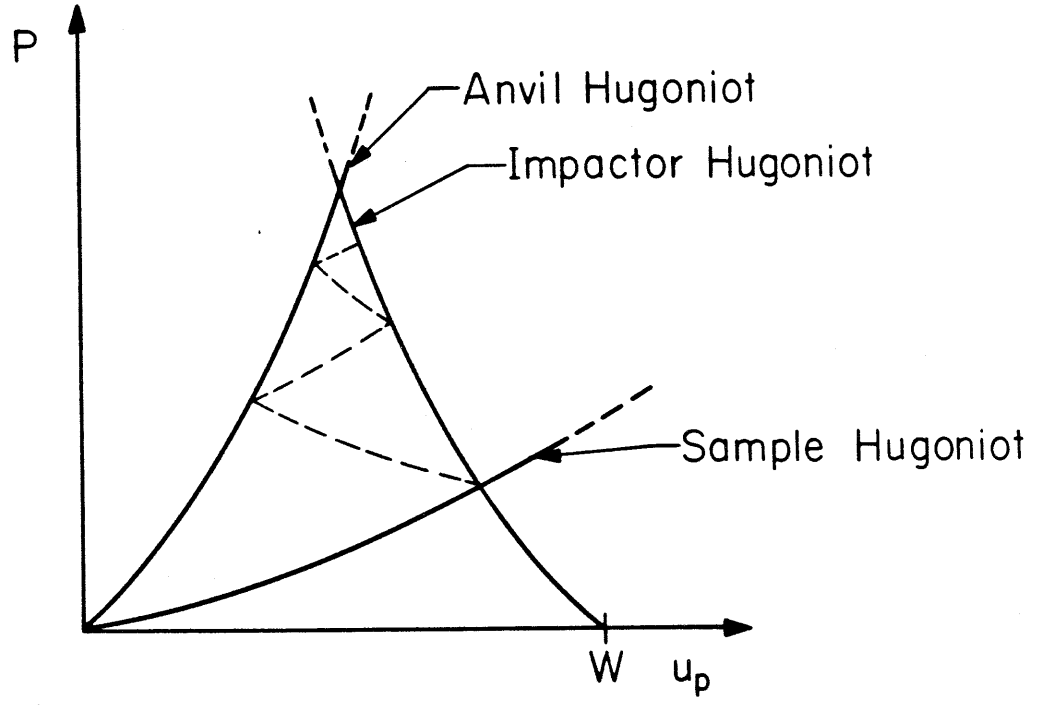

Figure 6-3. Shock reverberation experiment. Low-impedance investigated layer is multiply shocked by surrounding high-impedance flyer and anvil. Dashed curves indicate states of successive reflected shocks, approaching the intersection pressure of the high-impedance Hugoniots.

sandwiched between two thick layers of some standard substance of high shock impedance, the shock produced by the impact of one of the thick layers, acting as a flying impactor plate upon the intermediate layer will be multiply reflected from the two interfaces, gradually raising the pressure of the middle section. In the limit that the two outer plates are much thicker than the investigated layer, the ultimate pressure attained in the investigated region is equal to the Hugoniot pressure in the two surrounding plates if they were impacted at the same velocity with no intermediate layer. Furthermore, if the shock impedance of the investigated material is very small compared with the surrounding plates, the amplitude of the first shock in the sample is low compared with the ultimate pressure, and the degree of irreversible heating is consequently reduced. Even closer approximation of isentropic compression is achieved through the use of several material layers displaying a gradation in shock impedance properties, as in [11].

In that work, however, the ultimate goal of the experiment was the post-shot recovery of the compressed sample, with no attempt to determine the density state of the material at peak pressure. A set of computer experiments was carried out in the current investigation to examine possible experimental configurations which would be amenable to impact-driven experiments, with density measurements made using pulsed x-ray shadowgraph techniques.

The initial calculations were performed using water as the investigated sample. While it was desired to conduct these "experiments" under conditions which as closely as possible duplicated actual realizable experiments, some simplifying assumptions were made concerning the material

equations of state. All materials considered in these calculations were assumed to have their Hugoniot adiabats described by the linear $u_s - u_p$ relation,

$$u_s = su_p + C_0 \tag{6}$$

with the values of s and C_0 tabulated in Table 6-1. The data in this table have been derived, except as noted, from the Livermore shock wave data compendium [12]. Furthermore, the Grüneisen parameter was assumed given by the simple volume dependence,

$$\gamma = \gamma_0(V/V_0). \tag{7}$$

Assumed values of γ_0 are also tabulated. Throughout the discussion that follows in this chapter, when reference is made to the behavior of H_2O or other substances under isentropic compression, it is to be understood that this refers to the idealized material described above, without consideration of phase transitions or departures from the assumed equation of state which surely occur in the actual substance. With this in mind, the results of the numerical calculations should be considered as indicative of the general behavior of the investigated substances in actual experiments, even if not useful for precise predictions of their true outcomes.

Figure 6-4 shows the pressure-particle velocity Hugoniot curves of the six layer materials used in a set of symmetric impact calculations, in relation to that of H_2O. These materials comprise a sequence of materials whose impedances steadily increase from that of H_2O. The 13-layer impact configuration illustrated in Figure 6-5 was calculated for an impact velocity of 2.5 km/s.

Table 6-1

Assumed Hugoniot Parameters for Impact Calculations

Material	ρ_0 (g/cm^3)	C_0 (km/s)	s	γ_0
W	19.30	4.005	1.268	1.20
Ta	16.66	3.423	1.214	1.69
Fe	7.86	3.768	1.655	1.30
Al	2.70	5.355	1.345	2.13
Mg	1.78	4.650	1.200	1.46
Lexan	1.196	2.796	1.258	2.00
H_2O	1.00	3.111	1.160	2.00
CO_2	1.56	2.160	1.470	2.86
H_2	.0704	3.940	1.033	1.20

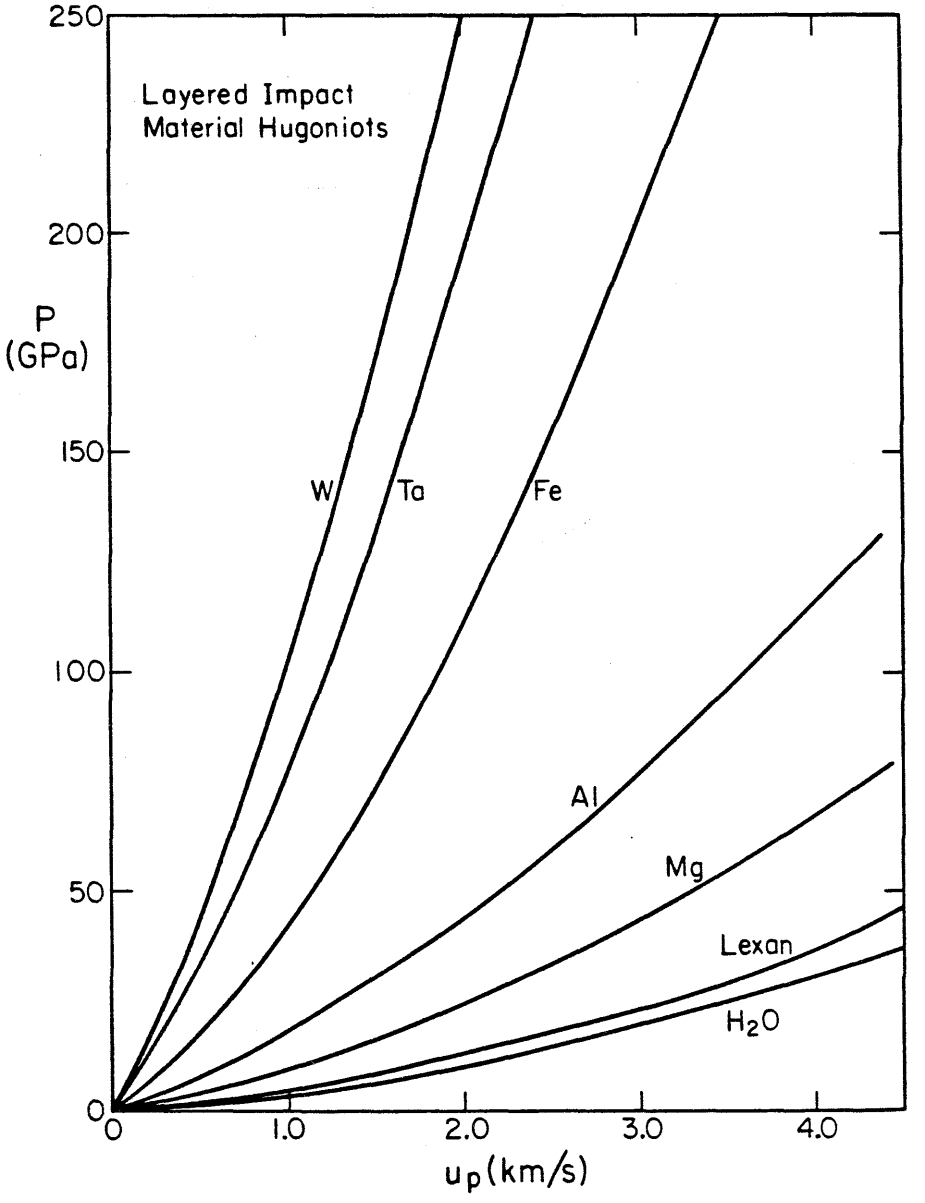

Figure 6-4. Pressure-particle velocity Hugoniot curves used for the six layer materials in symmetric impact calculations. The progressive increase in shock impedance from water (H_2O), through Lexan polycarbonate, magnesium, aluminum, iron, tantalum, and tungsten is illustrated.

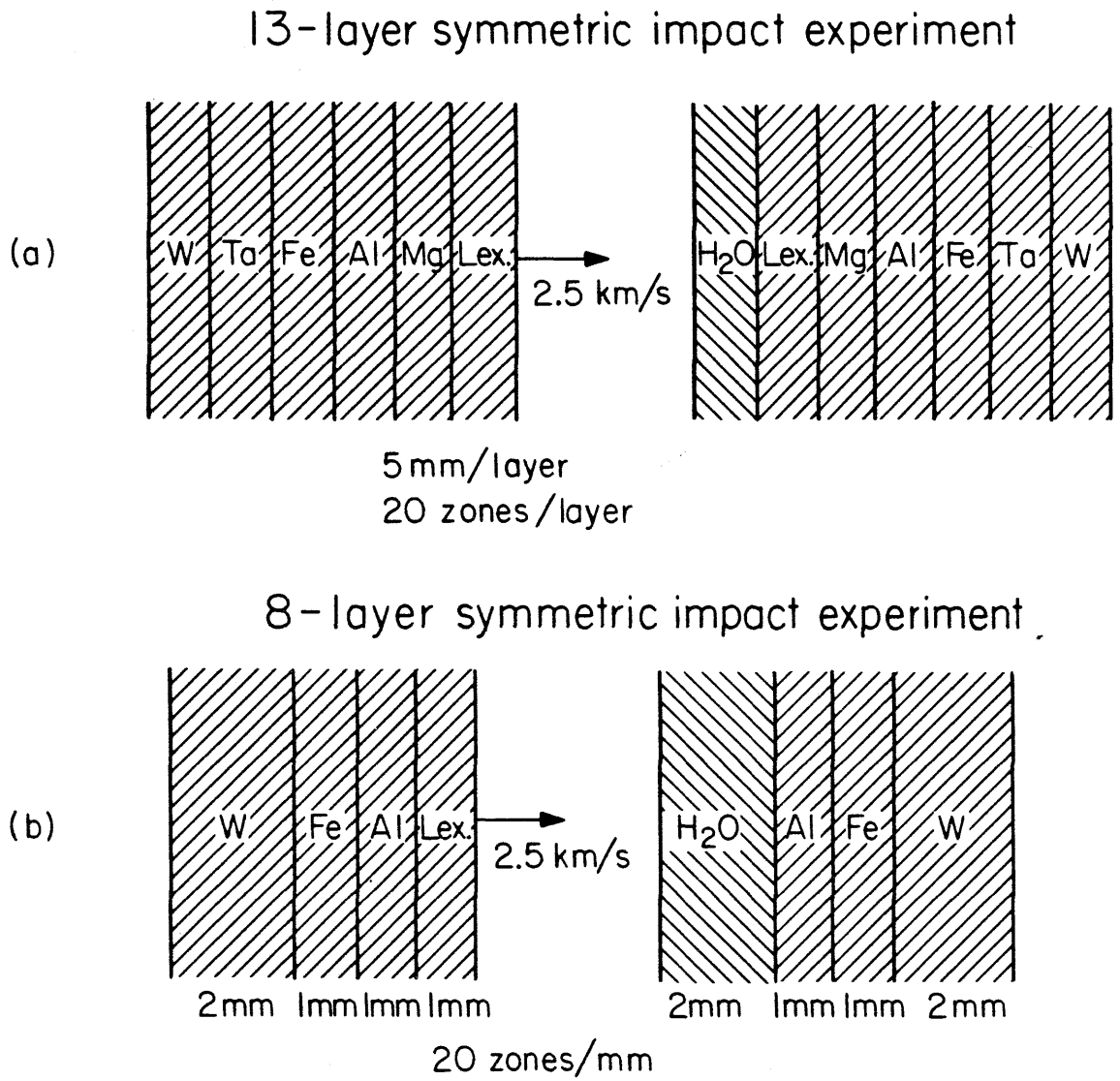

Figure 6-5. (a) 13-layer configuration used in computing symmetric impact experiment. (b) Simplified 8-layer impact configuration. Relative thicknesses of H_2O and W layers are increased. Both (a) and (b) assume 2.5 km/s impact velocity.

When H_2O is impacted by a composite flyer of the six materials, tungsten, tantalum, iron, aluminum, magnesium and Lexan (polycarbonate plastic) in the indicated sequence, a relatively smooth buildup of pressure in the central H_2O layer results. Figure 6-6 shows the computed pressure in a particular H_2O zone as a function of time from the impact. The time scale of the pressure rise is determined by the width of the material layers, which in this case were assumed to be 5 mm wide initially and divided into 20 discrete zones each.

In Figure 6-6 and succeeding plots of computed results, solid curves are used to show the theoretical Hugoniot curve and isentrope of H_2O, obtained from the assumed equation-of-state properties (Chapter 1). As seen in this graph, the H_2O pressure rises monotonically over a period of about 10 microseconds, tracing out a P-V path which is remarkably near to the isentrope. In terms of pressure, the deviation from the isentrope is negligible, although a measurable amount of shock heating is apparent in the energy and entropy results which are discussed below.

The peak observed H_2O pressure is ~70 GPa, which while being well below the 135 GPa limiting pressure possible with infinitely thick tungsten outer layers, is much higher than the 15 GPa maximum pressure attainable via a single shock with the same impact velocity. This result indicates that the method is generally feasible for producing isentropic compression in planar geometries. The described 13-layer impact demonstrates this in principle, but such an experiment could prove difficult in practice. In order to examine the validity of this approach in similar but more simple configurations, the 8-layer experiment illustrated schematically in Figure 6-5 was calculated. In this run,

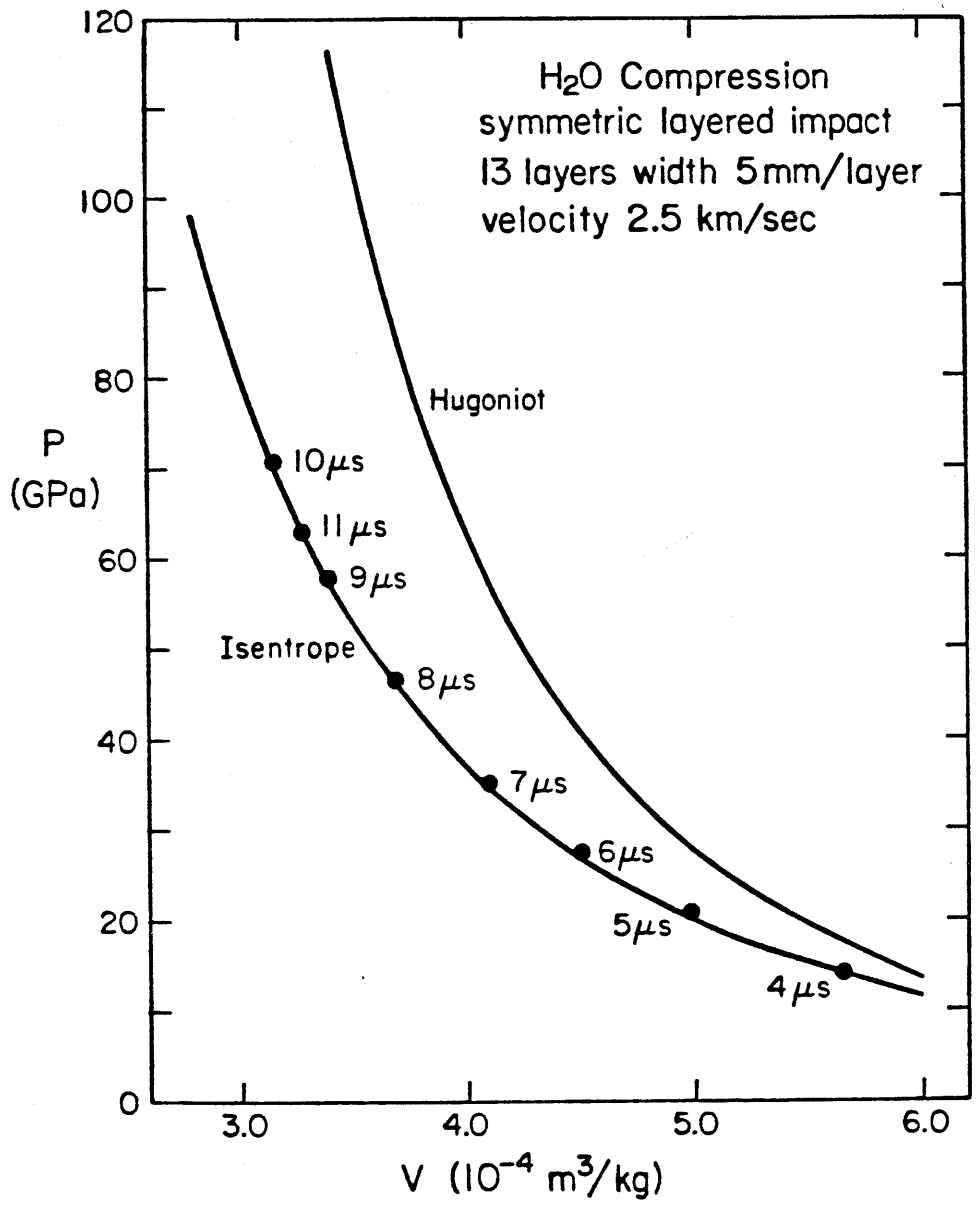

Figure 6-6. Computed results of 13-layer symmetric impact experiment. Points indicate computed pressure and specific volume within H_2O layer at the indicated times after impact. Theoretical Hugoniot and isentrope for H_2O are shown for comparison. Pressure in H_2O rises monotonically along a nearly isentropic path.

intermediate layers of tantalum and magnesium were omitted as well as one of the Lexan plates. The spatial scale of this experiment was reduced in order to check the invariance of the results with the sample size. In this case, the 2 mm H_2O layer was surrounded by 1 mm plates of Lexan, aluminum and iron, with final 2 mm tungsten plates whose increased thickness was intended to raise the final peak pressure.

As Figure 6-7 illustrates, even with the simplified 8-layer symmetric impact, compression very close to the isentrope is obtained. In just under 2 microseconds, the H_2O pressure rises to nearly 90 GPa, corresponding to a density increase on the isentrope of ~3.5 times. Such results are important since they demonstrate the possibility of achieving large isentropic compressions with experimental scales and impact velocities applicable to currently existing apparatus. Another important observation from these calculations is that in these cases, the pressure distribution with the investigated H_2O layer is uniform to within a few percent, thus suggesting the applicability of flash x-ray radiography as a density determination diagnostic technique.

While the symmetric impact approach discussed above shows considerable promise, it will be useful to consider an alternative approach which is more directly derived from the simple shock reverberation experiment of Figure 6-3. This alternative configuration, illustrated in Figure 6-8, offers some advantages from a standpoint of experimental simplicity. As the schematic illustration shows, a series of alternating plates of high and low shock impedance materials is impacted by a single thick flyer plate. In the present case, the flyer and high impedance layers are tungsten (W) while the investigated material comprising the low impedance

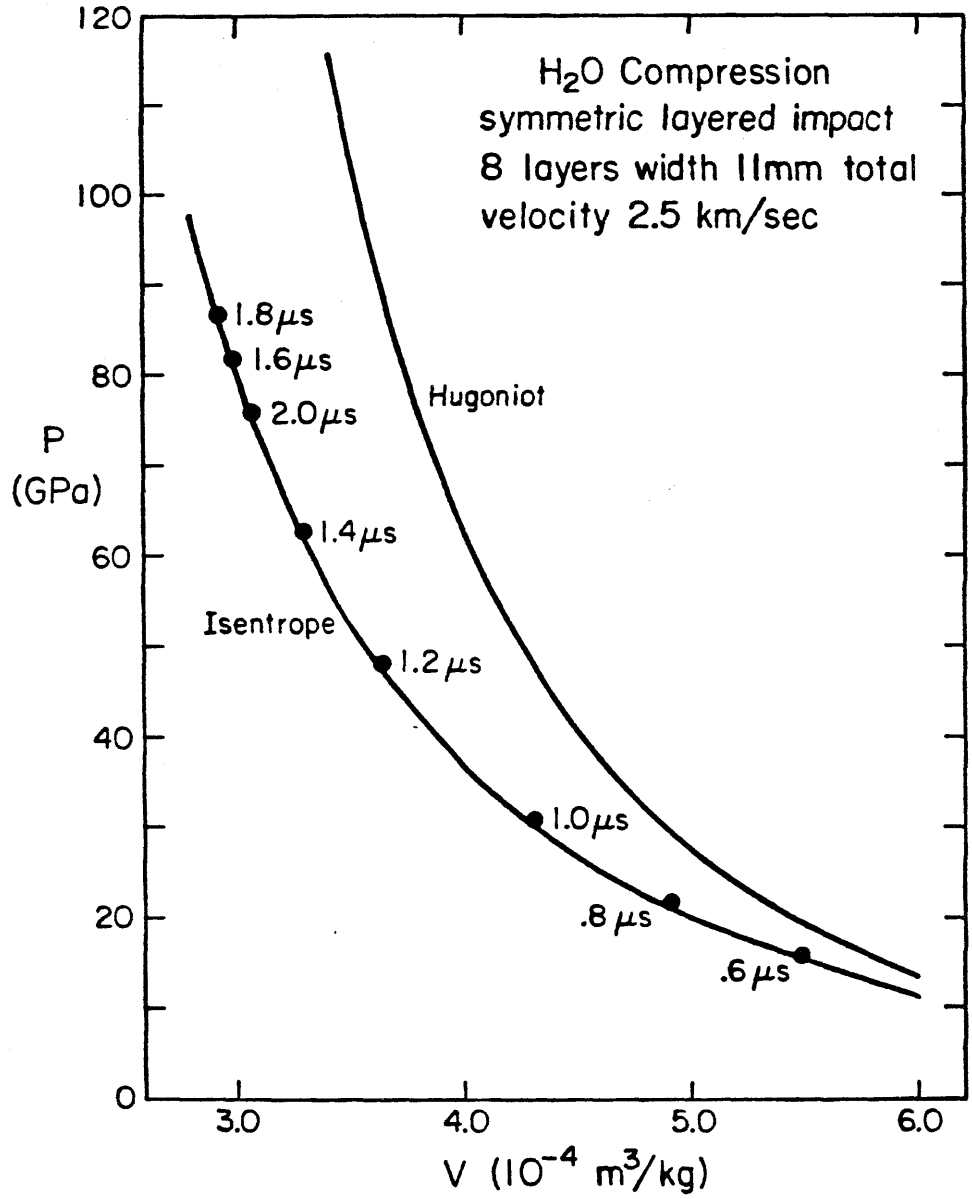

Figure 6-7. Results of 8-layer symmetric impact calculations. As in Figure 6-6, H_2O pressure path approximates isentropic compression.

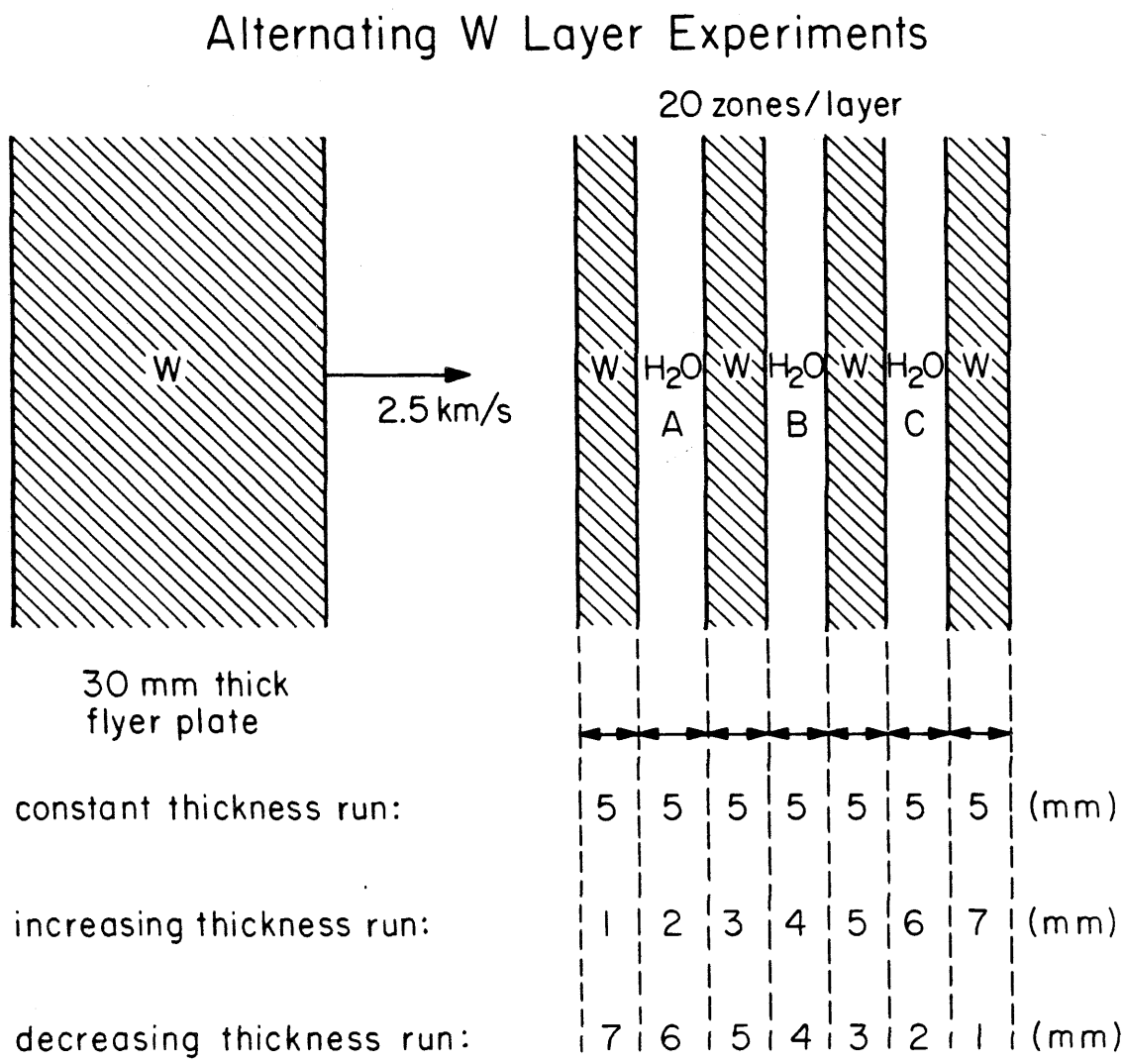

Figure 6-8. Configuration of alternating plate compression runs. Three cases are shown, with constant, increasing, and decreasing plate thickness along the propagation direction. H_2O layers labelled A, B, and C are monitored for pressure and density. Tungsten impactor velocity is 2.5 km/s.

layers is H_2O.

Three cases of this experiment are presented here. The first case considers the alternating layers to have all equal thicknesses of 5 mm. The remaining two cases have increasing and decreasing plate thickness along the propagation direction, as indicated in detail for each in Figure 6-8. Figure 6-9 displays the results of the constant layer thickness experiment, assuming the same 2.5 km/s impact velocity of the symmetric impact series. Two immediate differences from the result of the symmetric experiments are evident. The first is the expected observation that the pressure history in the sample is not monotonic, but oscillating in time. The sample pressures recorded in this figure and the succeeding alternating plate results are the pressures calculated in the second H_2O layer (labeled "B" in Figure 6-8). In addition to this fluctuating time dependence, the second difference from the earlier set of results is the relatively high peak pressure attained. In this case, the highest observed pressure along the quasi-isentropic compression path is actually somewhat higher than the 135 GPa tungsten reverberation pressure.

Figures 6-10 and 6-11 present the analogous results for layer "B" pressures in the increasing and decreasing plate thickness geometries, respectively. The qualitative nature of each of these calculations is the same, displaying pressure-volume states near or on the isentrope, corresponding to up to four-fold compression of H_2O from standard conditions. In order to obtain a more objective evaluation of the symmetric impact and alternating plate runs, a quantitative measure of the "quality" of the achieved state is sought. In addition to providing pressure-volume calculations during wave propagation, the WONDY program provides as a

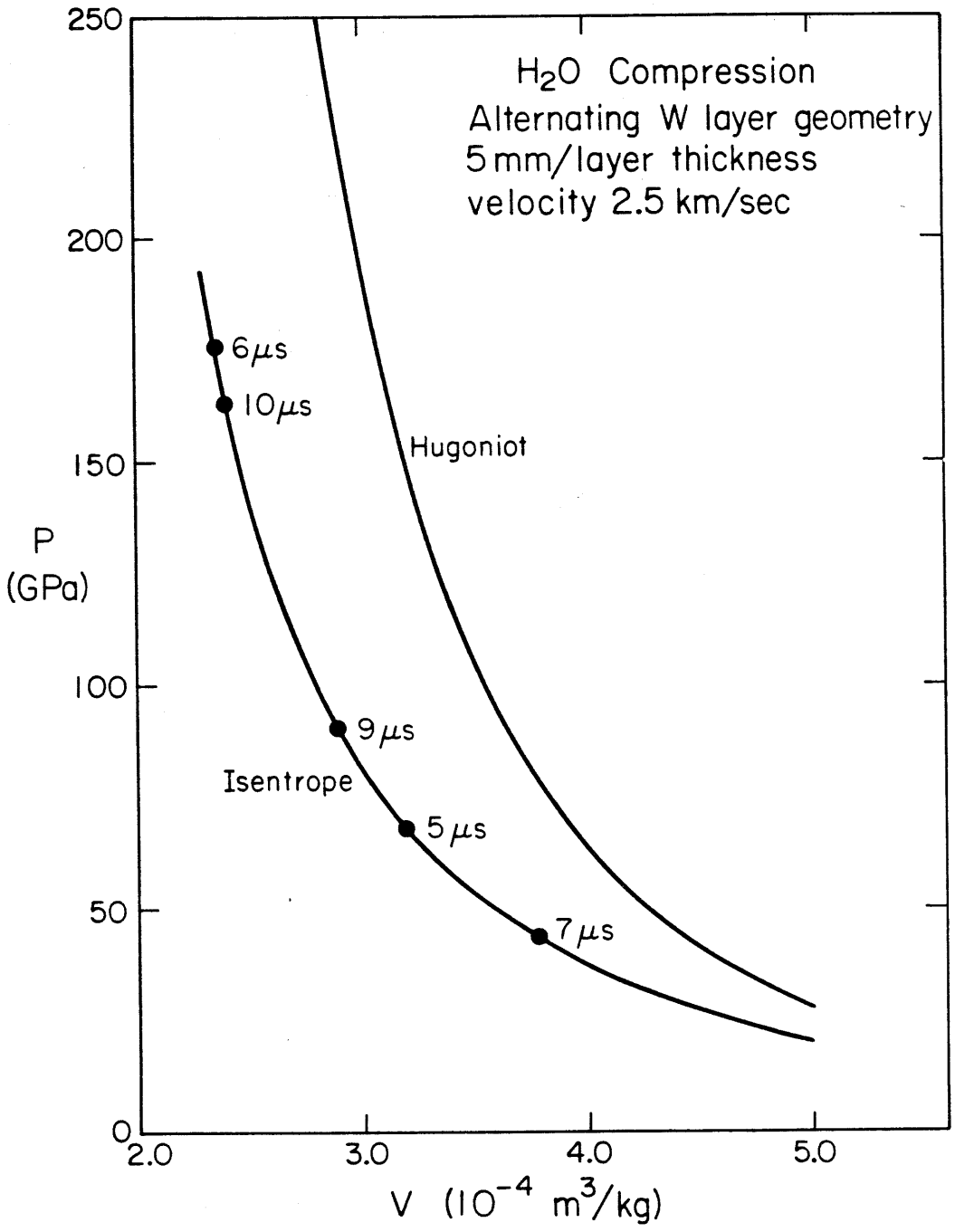

Figure 6-9. Computed results for H_2O in central layer B of alternating plate run with constant plate thickness. Indicated times show oscillatory pressure behavior. H_2O Hugoniot and isentrope again shown for comparison.

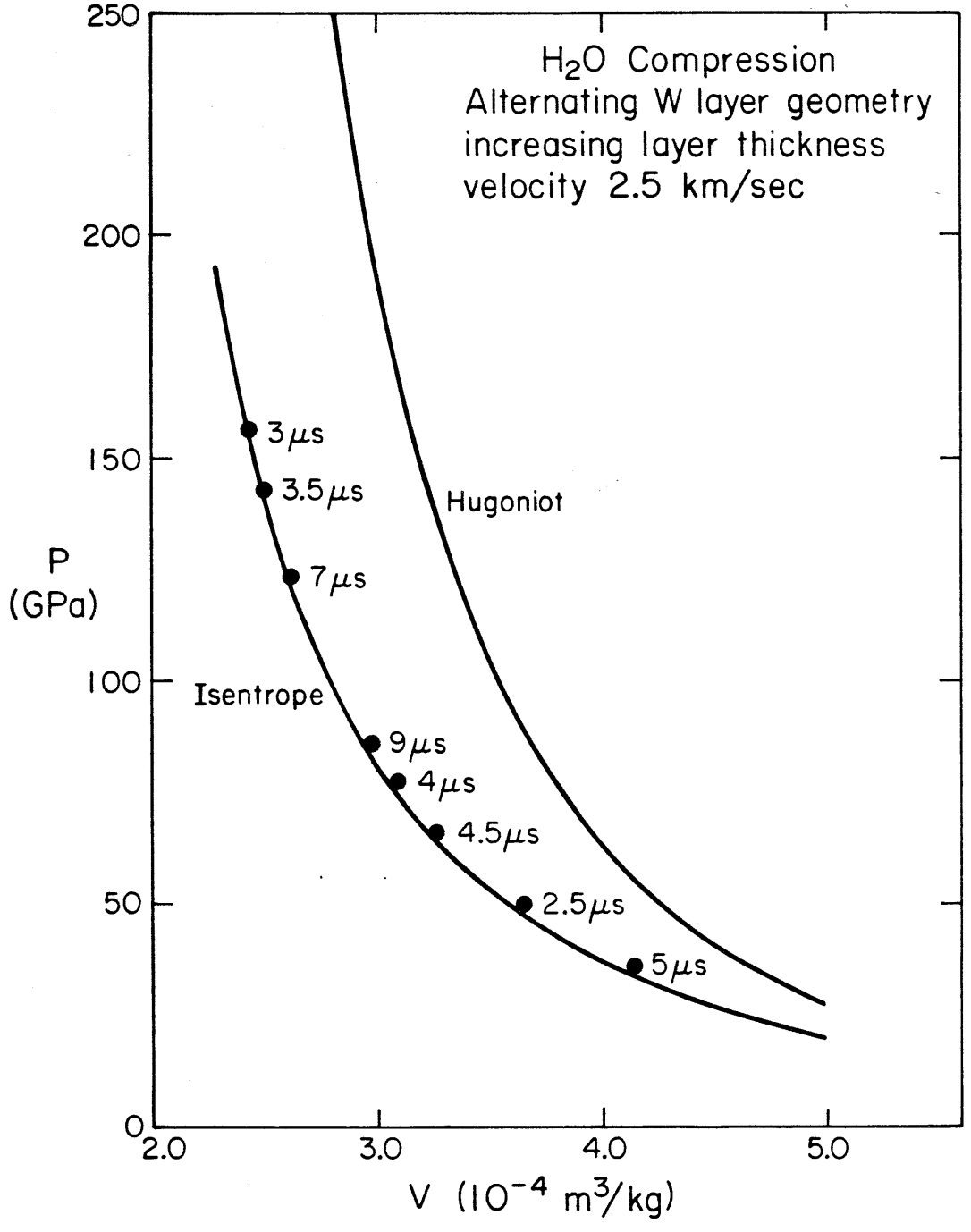

Figure 6-10. Results from H_2O alternating plate run with increasing plate thickness. Pressure is in central H_2O layer B.

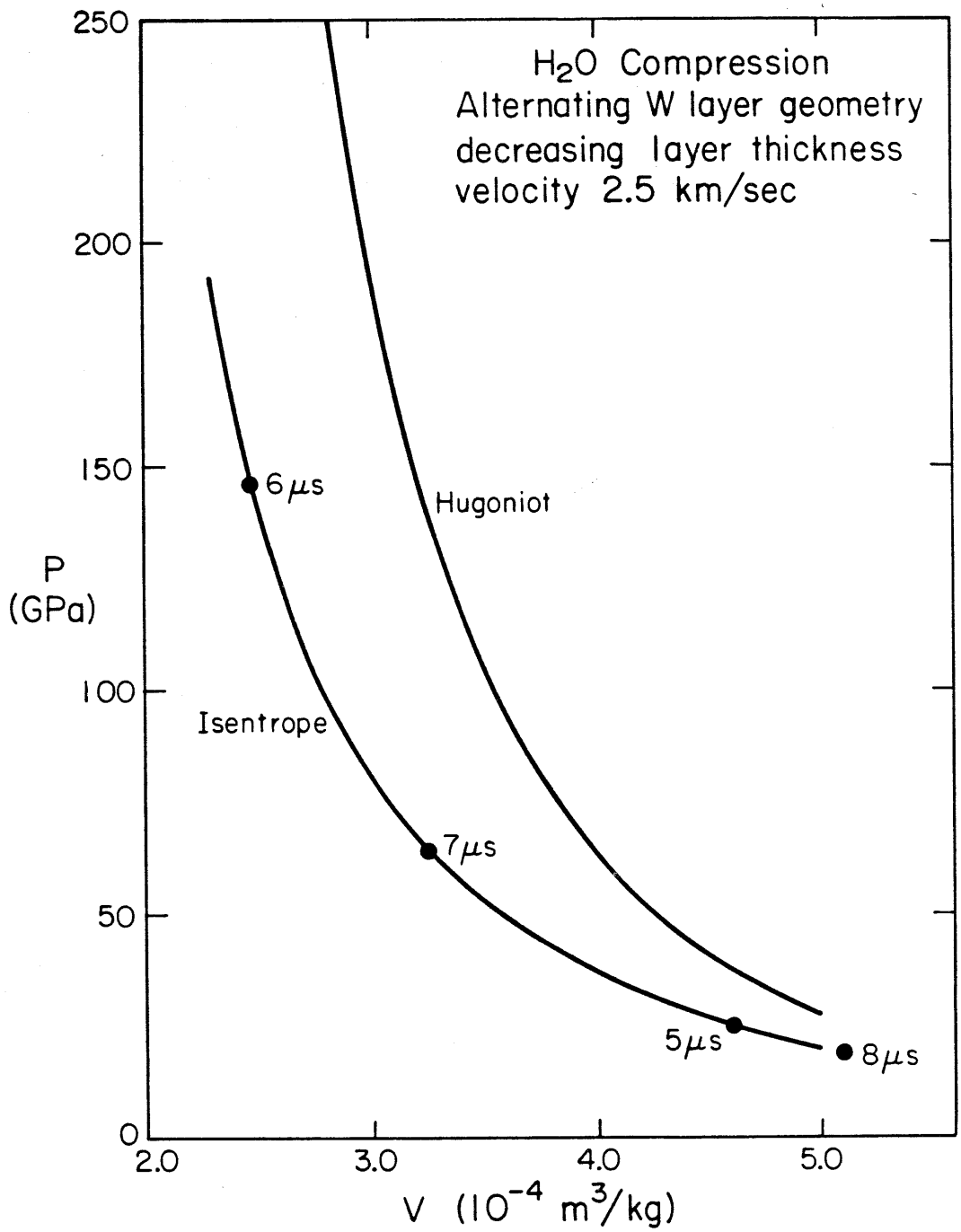

Figure 6-11. Results from H_2O alternating plate run with decreasing plate thickness. Pressure is in central H_2O layer B.

matter of course, the zone-by-zone specific internal energy of the investigated materials. By employing this quantity, along with some assumptions about the material properties, the entropy generation in each experiment may be calculated.

The entropy increase Δs from standard conditions in going to an arbitrary state (P_i, V_i, E_i) may be expressed in terms of the temperatures in state i and on the isentrope at the same volume. This may be written as

$$\Delta s = \int_{T_s}^{T_i} \frac{C_v dT}{T} . \tag{8}$$

Furthermore, the specific internal energy difference between these same states may be written,

$$\Delta E = E_i - E_s = \int_{T_s}^{T_i} C_v dT. \tag{9}$$

If we assume that C_v = constant, then the above integrals are immediately evaluated and

$$\Delta s = C_v \ln(T_i/T_s) = C_v \ln\left(\frac{\Delta E}{3RT_s} + 1\right). \tag{10}$$

Therefore, in the present calculations, ΔE is obtainable directly from the WONDY calculated state E_i and the known theoretical isentrope. T_s is calculated readily from Mie-Grüneisen theory (Chapter 1) and the entropy jump Δs is directly obtained. In the case of ideal isentropic compression, ΔE and Δs are both zero. Since in these computer "experiments" the correct isentrope is implicitly <u>assumed</u> known in the formulation of the computer code's equation of state, values of Δs calculated for various computed runs accurately reflect the relative degree

of irreversible heating due to each configuration, even though the absolute values of calculated entropy may not bear a strong resemblance to the reality of actual substances.

Figures 6-12 through 6-15 show the entropies calculated in this manner, for each of the experimental configurations. Entropy is plotted as a function of pressure, and the theoretical entropy along the Hugoniot is also shown for reference. Figure 6-12 illustrates the interesting result that the entropy production in the symmetric impact is small and relatively constant up to very high pressures. Additionally, this entropy production is apparently not strongly influenced by the number of stacked plates.

The magnitude of this "background" entropy level is evidently controlled by the amplitude of the first shock to traverse the investigated layer. In the symmetric impacts of Figure 6-12 (W = 2.5 km/s), the first shock in the H_2O layer is caused by the impacting Lexan layer and has an amplitude of ~5 GPa. Interestingly, the observed entropy production is very nearly the Hugoniot entropy at just this first shock pressure of 5 GPa. Evidently, the bulk of the entropy contribution comes from the initial shock, with essentially negligible contribution from succeeding disturbances which elevate the pressure to as high as 100 GPa or more.

Entropy calculations for the alternating plate experiments display the same behavior, with the chief determining factor in the entropy of each layer being the initial shock amplitude early in the compression history. Several general trends are evident in a comparison of the results in Figures 6-13, 6-14, and 6-15 for the various alternating plate geometries. In general, the rearward layers "B" and "C" display lower

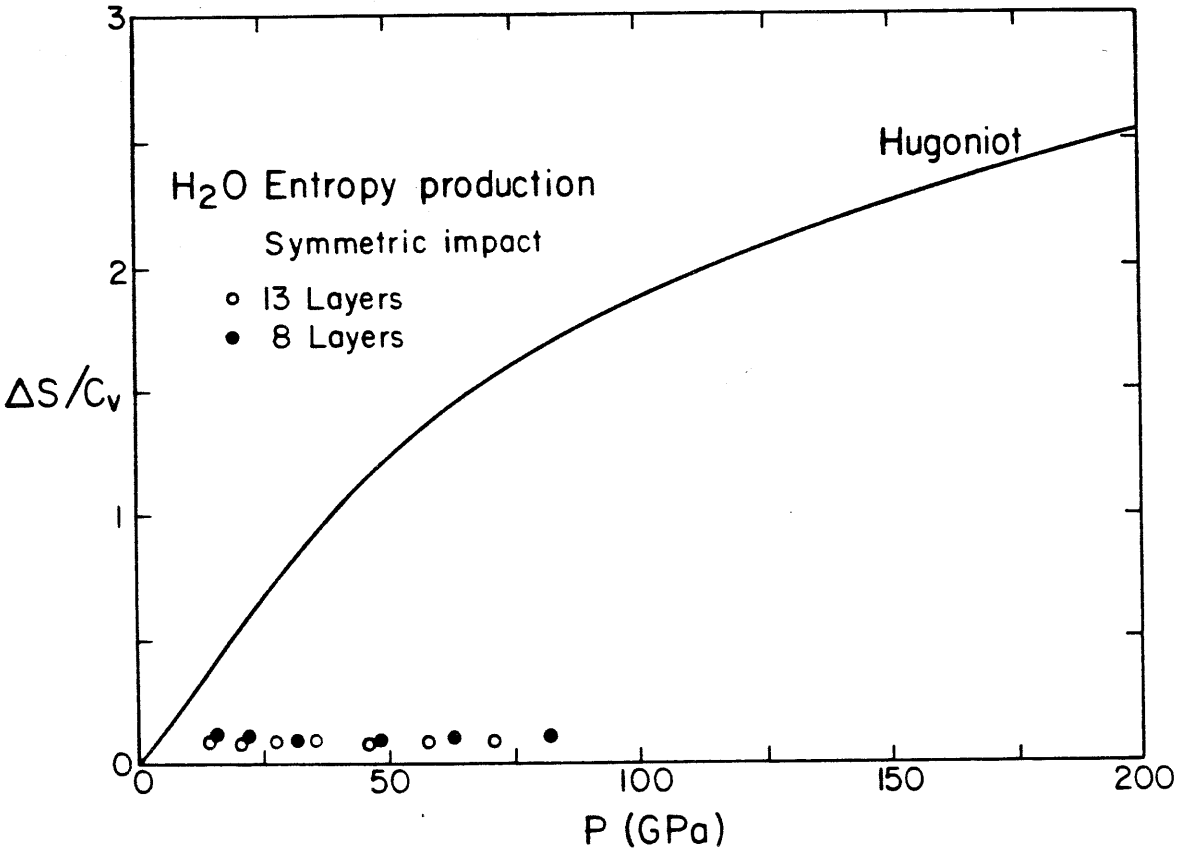

Figure 6-12. Specific entropy rise calculated from results of symmetric impact runs. Entropy in computed experimental points and on theoretical Hugoniot is from equation (10). Note nearly constant low entropy at all pressures.

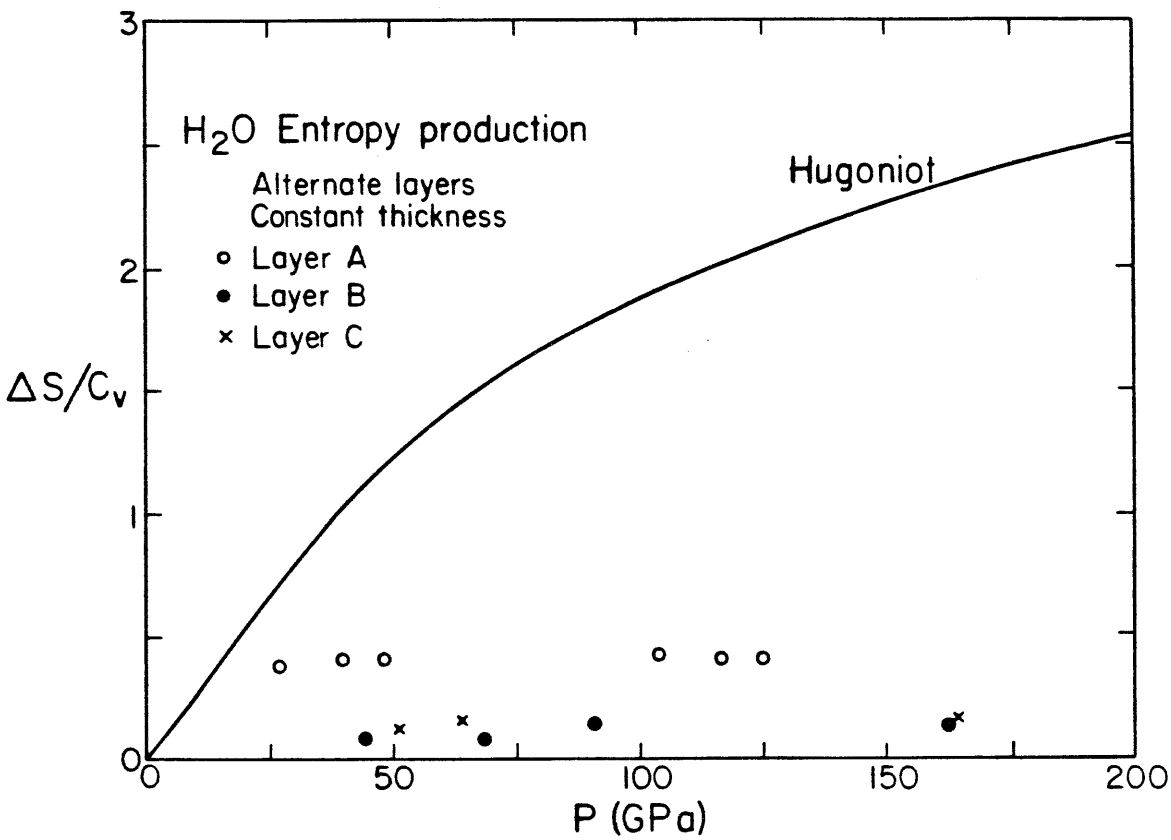

Figure 6-13. Calculated entropy production in constant thickness alternating plate experiment. Entropy production in all three H_2O layers (A, B, and C) is shown with theoretical Hugoniot entropy curve.

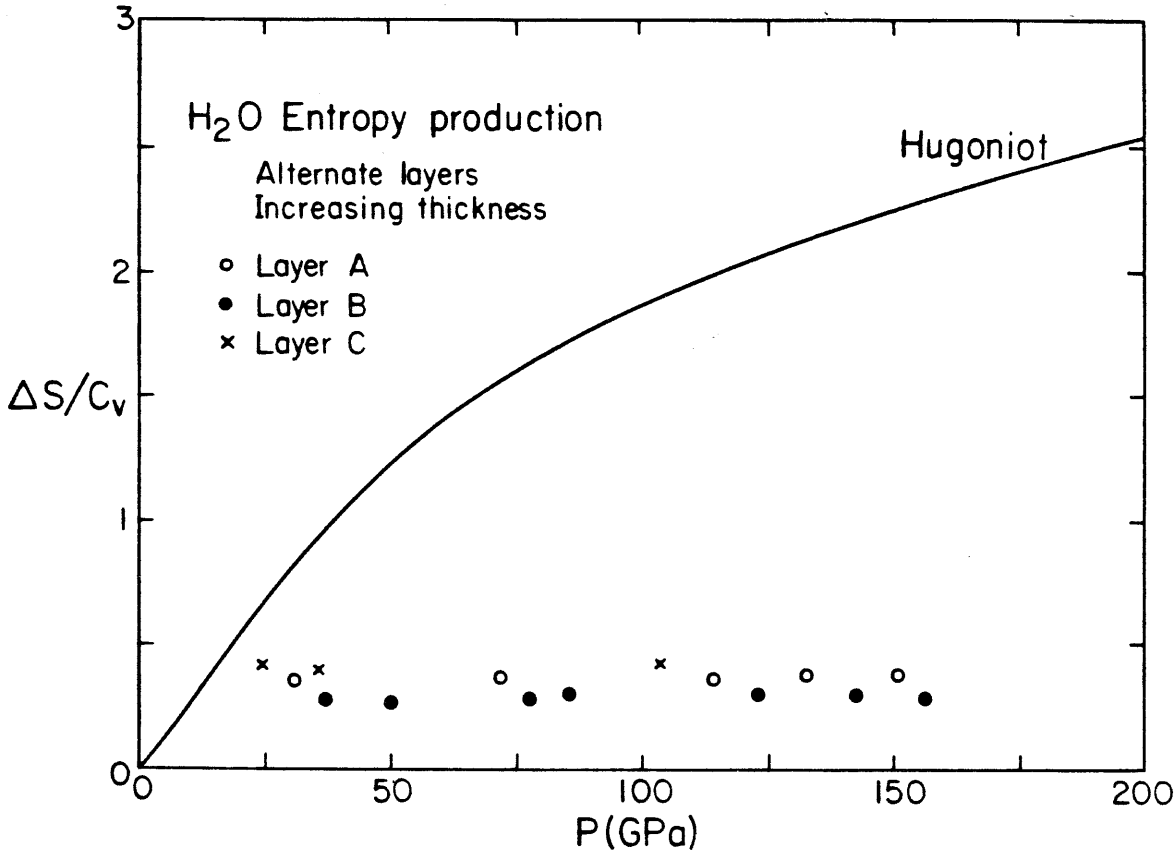

Figure 6-14. Calculated entropy production in increasing thickness alternating plate experiment.

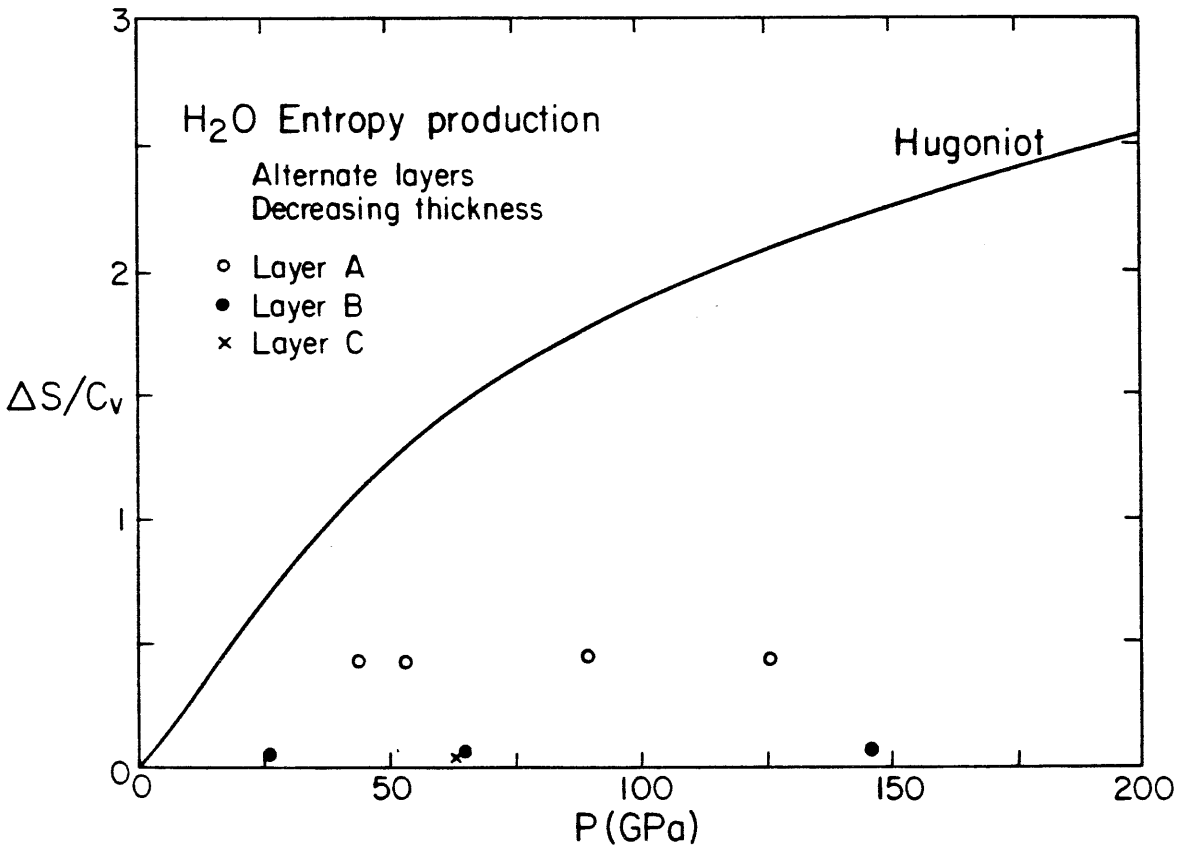

Figure 6-15. Calculated entropy production in decreasing thickness alternating plate experiment. Note exceptionally low entropy rise in this case.

entropy than the directly shocked layers "A." Furthermore, the configuration with decreasing plate thickness along the propagation direction affords the least entropy production, which is even smaller in plates "B" and "C" than that obtained in the symmetric impact runs. Such an experimental configuration may point the way toward the optimum geometry. One desirable refinement would be a configuration which accurately produces the W reverberation pressure in one or more of its layers, thus obviating an independent pressure calibration in actual experiments.

For purposes of completeness in discussing the results of the current research, the following is a brief summary of similar results obtained in calculations with other candidate materials for investigation. Solid carbon dioxide (T_0 = 196 K) and liquid molecular hydrogen (T_0 = 20 K) are two low-density molecular substances whose behavior under conditions of large isentropic compression are of considerable interest. Layered symmetric impact calculations have been carried out for each of these materials, to provide comparison with the H_2O calculations and to give some indication of the range of probable applicability of these techniques to materials of various properties.

The Hugoniot equations of state for liquid H_2 and solid CO_2 have been reported in [4] and [13] respectively, and the fits to the existing data used in the present work appear in Table 6-1. Figures 6-16 and 6-17 present the pressure and entropy results for solid CO_2 compressed in the 13-layer symmetric layer configuration, with an impact velocity of 2.5 km/s. It is apparent that the results obtained are qualitatively similar to those of the H_2O experiments, with only a slightly larger specific entropy production due to the initial shock.

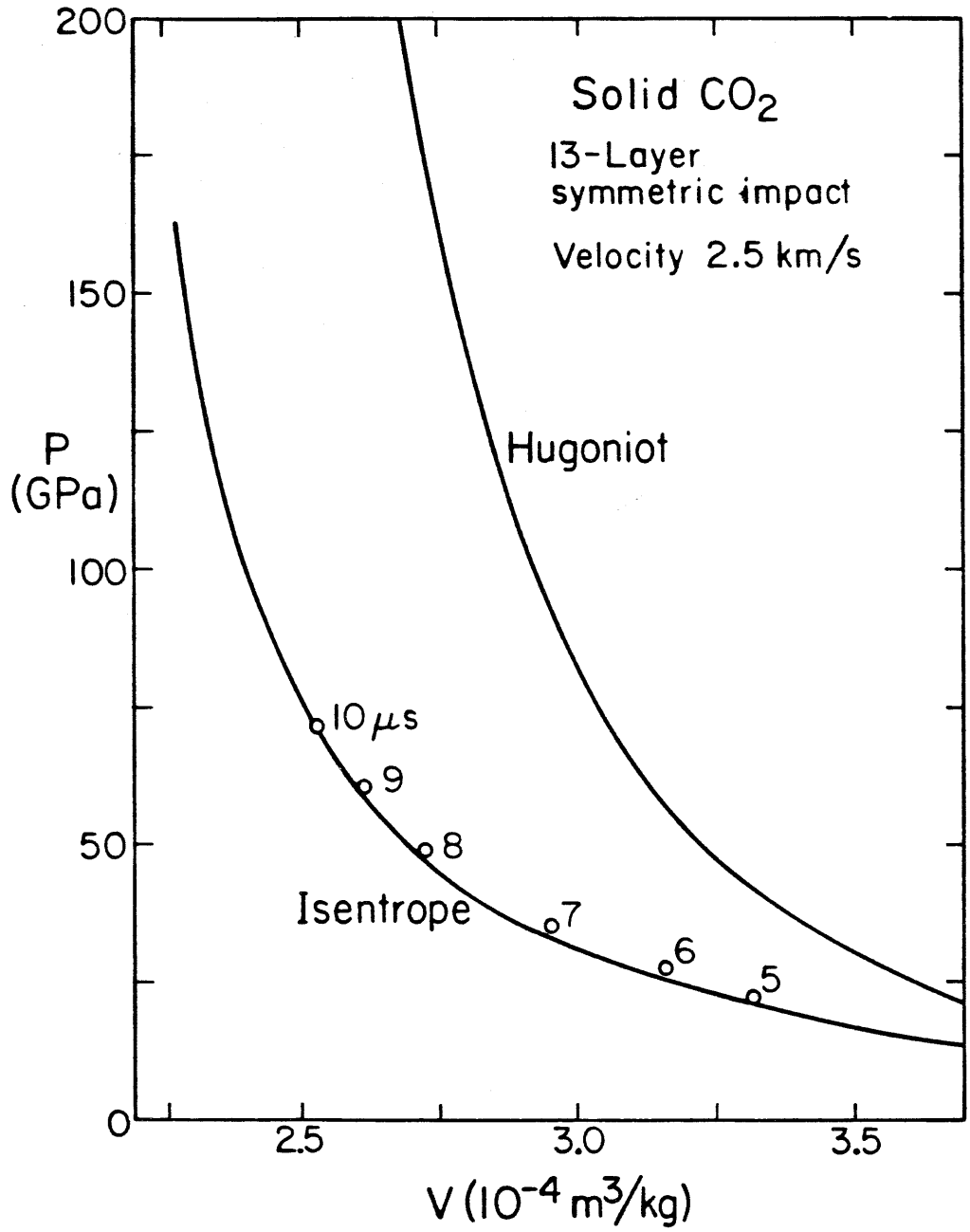

Figure 6-16. Computed results obtained from 13-layer symmetric impact with solid CO_2 replacing water as the investigated layer. CO_2 isentropic compression points plotted with theoretical Hugoniot and isentrope, as in Figure 6-6.

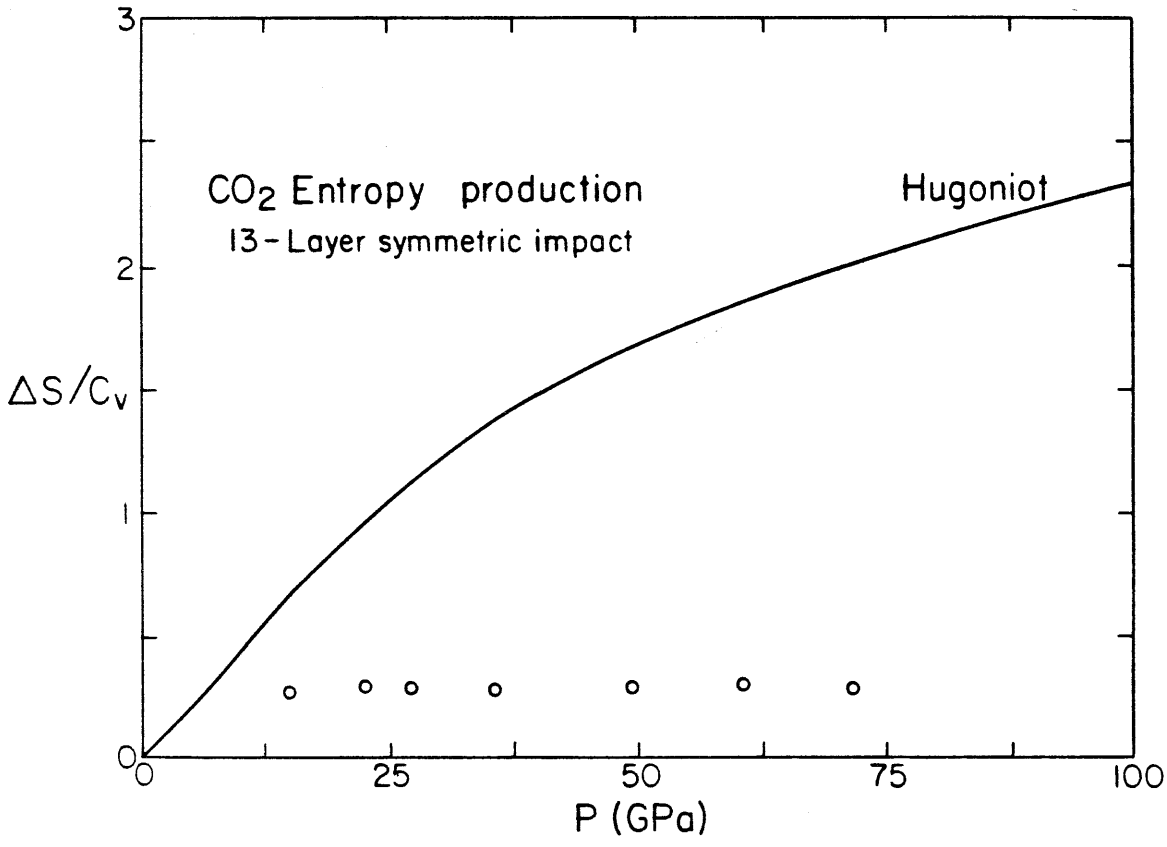

Figure 6-17. Calculated CO_2 entropy production in symmetric impact run of Figure 6-16.

Liquid hydrogen results are shown in Figures 6-18 and 6-19, with two cases illustrated. Both cases incorporate a 6.0 km/s impact velocity. The 8-layer symmetric impact run, analogous to the 8-layer water experiment, reaches a relatively modest peak pressure of ~70 GPa, while achieving states close to the isentrope. For purposes of comparison, a calculation for the case of simple reverberation between thick tungsten plates (as in Figure 6-3) is also shown. This experiment reaches the substantially higher W reverberation pressure but accomplishes this in relatively few large shock steps. The entropy plots of Figure 6-19 show that the symmetric impact experiment produces the least irreversible heat of these cases, but that in either case, the compression of the very low-density hydrogen is accompanied by more specific entropy production in a given configuration than for the relatively dense H_2O and CO_2.

Summary and Implications

The results of the current calculations allow a few broad conclusions to be drawn, in addition to pointing the way toward further calculations and actual experiments. In general, it is apparent that a good approximation to isentropic compression may be realized experimentally through the method of multiple shock interactions. The major obstacle to such work, however, is devising practicable experimental designs which allow density and pressure determinations with useful precision. In the promising calculations of the alternating plate compression experiments, it appears likely that given a sufficiently large number of plates, the tungsten reverberation pressure can be nearly duplicated in the H_2O layers, thus providing an unequivocal pressure determination. In the same experiments,

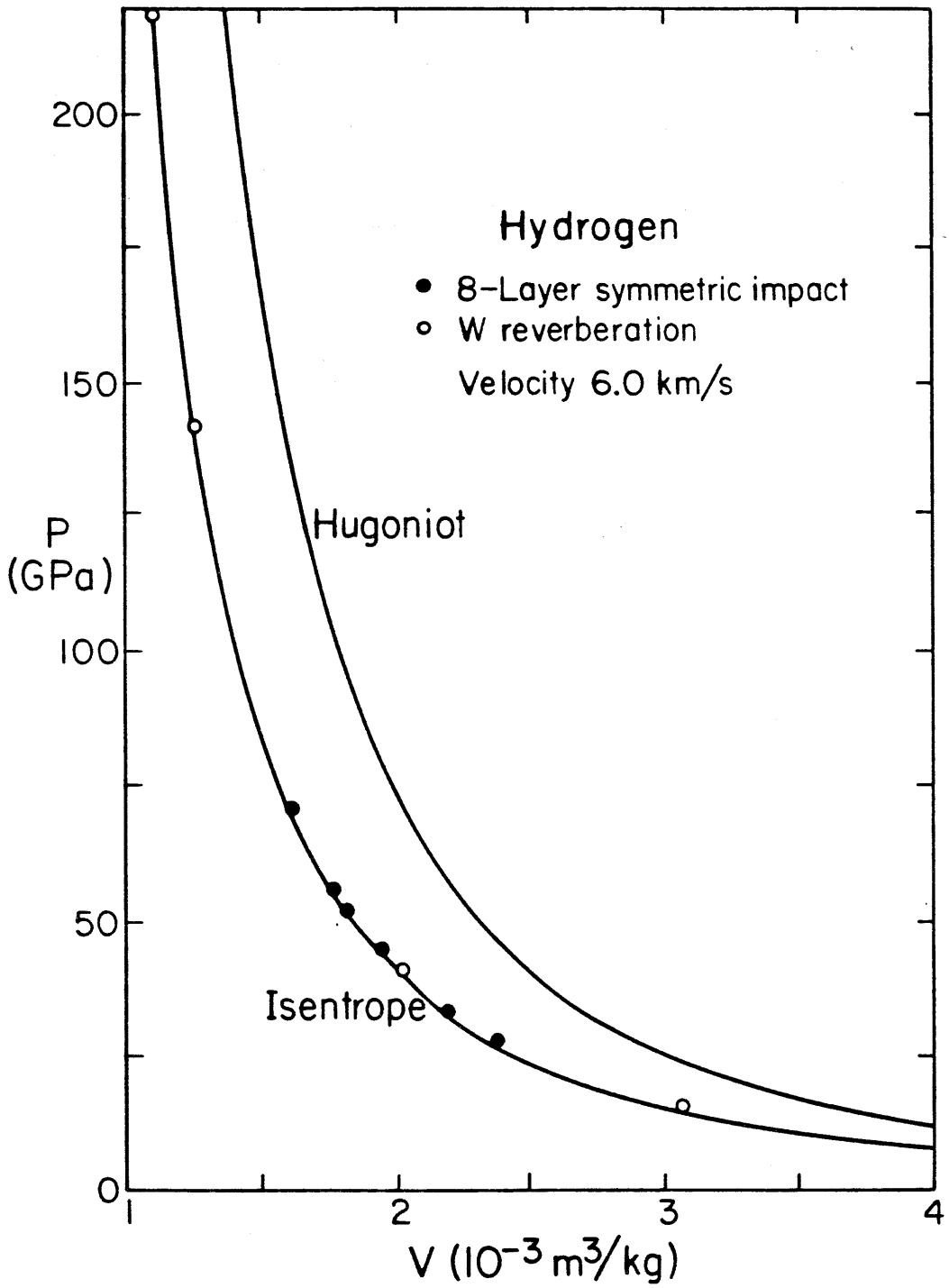

Figure 6-18. Computed pressure-volume results for two runs with liquid hydrogen (H_2) as the investigated sample. Results for 8-layer symmetric impact and simple tungsten reverberation are given.

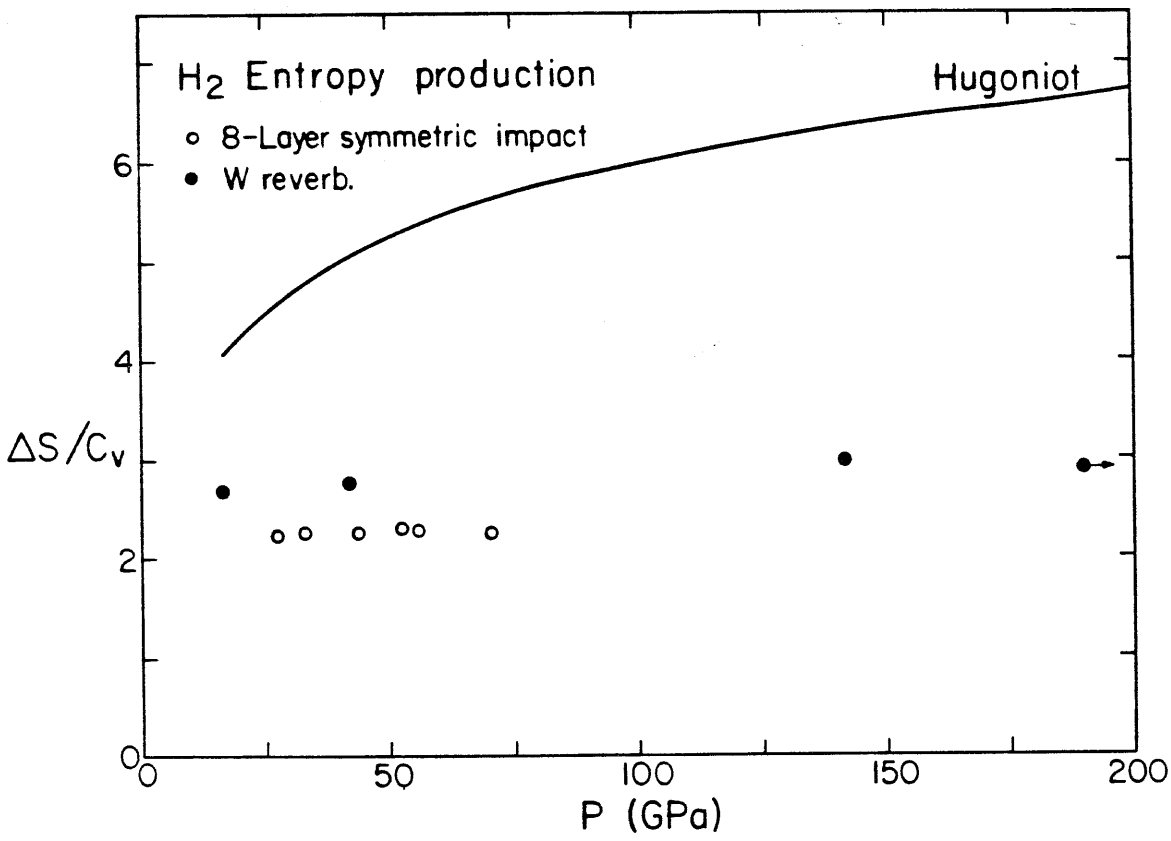

Figure 6-19. Calculated entropy production in liquid H_2 from the two compression runs illustrated in Figure 6-18. 8-layer impact affords less entropy production than W reverberation impact.

density measurements via x-ray shadowgraph techniques could be obtained, given layers of sufficient dimensions to allow satisfactory precision of measurement.

All of the above calculations have assumed one-dimensional flow, neglecting the edge effects which result in any real shock experiment from the finite lateral dimensions of the shocked specimens. In the previously described shock temperature experiments, the spurious effects of edge rarefactions propagating inward were eliminated by studying specimens several times larger in their lateral dimensions than the thickness along the direction of shock motion. In that case, masking of the relatively narrow affected edge region eliminates any spurious radiation coming from the released regions. In the presently considered isentropic compression experiments, however, large target (and impactor) thicknesses are evidently required in order to satisfy simultaneously the requirements for good pressure and density determinations.

While such large thicknesses can be accommodated by devising shock driving systems of large lateral dimensions, the difficulty and cost of performing such experiments rises rapidly with increasing scale. For the present consideration of impact experiments of conventional scale, attention must be focused upon finding variants of the above described isentropic experiments, which can accomplish the desired compression with a minimum thickness of surrounding layers.

Future successful experiments employing the multiple-shock principles illustrated here should take advantage of material configurations which minimize the initial shock amplitude and entropy production in the sample, while subjecting it to as uniform and continuous a compression process

as possible. On the other hand, application of the density-gradient method for conversion of shocks to isentropic waves evidently requires variable density target materials with rather large ranges in initial state. One solution to this problem may be the use of variable porosity media, such as plastic foams. In such a case, variable density medium would not constitute the investigated layer but could be used to transmit a "broadened" shock wave into a material of interest. Clearly in such a case, the sample wave profile would vary in time, and the state of compression would vary from point to point within the medium. Such experiments thus would require density and pressure measurement techniques sensitive to spatial variations as well as to the motion of the studied medium. Imbedded foil x-ray shadowgraph measurements could provide such records.

The basis of such measurements rests upon the Riemann solution for isentropic flow in an ideal fluid. As derived by Rice et al. [14], the particle velocity in such a flow is simply related to the isentropic compressibility through the Riemann integral,

$$u_p = \int_{\rho_0}^{\rho} \frac{C d\rho}{\rho} \quad . \tag{11}$$

Here, C is the sound speed defined by

$$C(\rho) = \left(\frac{\partial P}{\partial \rho}\right)_s^{1/2} \quad . \tag{12}$$

Using this together with the fact that the pressure along the assumed isentropic compression path is a function of the density ρ $(= 1/V)$ only, equation (11) may be rewritten,

$$u_p = \int_{P_0}^{P} \left(-\frac{\partial V}{\partial P}\right)^{1/2} dP \quad . \qquad (13)$$

These equations are applicable in compressive flow for times before x-t characteristics of the flow cross, and the wave profile steepens into a nonisentropic shock. Equation (13) may be applied to an experiment in which a wave of isentropic compression is transmitted to a sample of interest. If a series of thin foils which are opaque to x-rays are imbedded in the sample, inclined at an angle to the plane of oncoming waves, flash x-ray photographs of the sample can be used to characterize the flow with minimal perturbations of the wave. Observations of changing inclination angle and displacement of the foil layers in shadowgraphs taken at two successive times provide measurements of density versus particle velocity throughout the compression wave. Thus in principle, these data could be inverted through equation (13) to obtain the isentrope $P(V)$ for the studied material.

The potential applications of equation-of-state measurements along the isentrope at very high pressures are numerous. For the general subject of this research, the implications of such experiments would be important. Direct observation of states on the isentrope would considerably strengthen the interpretations of shock temperature measurements by placing stricter limits on the Grüneisen γ and its variation with volume and temperature. Furthermore, as the isentropes of various materials are observed to cross the boundaries of new high-pressure phases, a rich field of condensed matter physics will be explored. This is yet another application in which pyrometric temperature measurement could be employed to

advantage, in characterizing the thermal processes in such transitions. In summary, the development of techniques for achieving isentropic compression in solids may prove practicable, and it promises to augment considerably the information currently obtained from more conventional shock wave experiments at high pressure.

REFERENCES

1. Ragan, C. E., Hugoniot measurements near 50 Mbar, preprint no. LA-UR-79-1992, Los Alamos Scientific Laboratory, Los Alamos, New Mexico (1979).

2. Al'tshuler, L. V., N. N. Kalitkin, L. V. Kuz'mina and B. S. Chekin, Shock adiabats at ultrahigh pressures, UCRL translation ref. 02251 (from preprint of Institute of Applied Mathematics, USSR Academy of Sciences), Lawrence Livermore Laboratory, Livermore, California (1976).

3. Al'tshuler, L. V., Use of shock waves in high-pressure physics, Sov. Phys. Usp., 8, 52-91 (1965).

4. Ross, M., A theoretical analysis of the shock compression experiments of the liquid hydrogen isotopes and a prediction of their metallic transition, J. Chem. Phys., 60, 3634-3644 (1974).

5. Kawai, N., S. Mochizuki and H. Fuilta, Densification of vitreous silica under static high pressures higher than two Mb, Phys. Lett., 34A, 107 (1971).

6. Hawke, R. S., D. E. Duerre, J. G. Huebel, R. N. Keeler and H. Klapper, Isentropic compression of fused quartz and liquid hydrogen to several Mbar, Phys. Earth Planet. Int., 6, 44-47 (1972).

7. Pavlovskii, A. I., N. P. Kolokol'chikov, M. I. Dolotenko and A. I. Bykov, Isentropic compression of quartz by the pressure of a superstrong magnetic field, JETP Lett., 27, 264-266 (1978).

8. Kompaneets, A. S., V. I. Romanova, P. A. Yampol'skii, Conversion from shock to isentropic compression, ZhETF Pis. Red., 16, 259-262 (1972).

9. Kompaneets, A. S., V. I. Romanova, and P. A. Yampol'skii, On shock propagation in an inhomogeneous condensed medium, Fizika Goreniya i Vzryva, 11, 807-809 (1974).

10. Lawrence, R. J., and D. S. Mason, WONDY IV - A Computer Program for One-dimensional Wave Propagation with Rezoning, report no. SC-RR-710284, Sandia Laboratories, Albuquerque, New Mexico (1975).

11. Adadurov, G. A., V. V. Gustov, V. S. Zhuchenko, M. Yu. Kosygin and P. A. Yampol'skii, On the transformation of shock compression into isentropic compression, Fizika Goreniya i Vzryva, 9, 576-579 (1973).

12. Van Thiel, M., editor, Compendium of Shock Wave Data, Report UCRL-50108, Lawrence Livermore Laboratory, University of California, Livermore, California (1977).

13. Zubarev, V. N., and G. S. Telegin, The impact compressibility of liquid nitrogen and solid carbon dioxide, Sov. Phys. Dok., 7, 34-36 (1962).

14. Rice, M. H., R. G. McQueen and J. M. Walsh, Compression of solids by strong shock waves, Solid State Physics, 6, 1-63 (1958).

Appendix I

DESIGN AND EXECUTION OF SHOCK PYROMETRY EXPERIMENTS

Experimental Apparatus and Layout

The experimental components which accomplish and support the shock temperature measurements presented in this thesis are described here under four subsystem classifications. These are the target assembly, the pyrometer optical and mechanical unit, the electronic detection and recording subsystem, and the support diagnostics relevant to the light-gas gun operation and performance. The current description applies to shock pyrometry experiments carried out with the Lawrence Livermore Laboratory light-gas gun.

The basic target assembly design is illustrated in Figure I-1, for the case of solid samples. The modifications incorporated for liquid samples are straightforward and are elucidated in Chapter 5. As noted in the illustration, the target assembly is positioned in the evacuated impact chamber so that projectile impact occurs after a free-flight distance of roughly 30 cm. The target position is fixed by the requirement of maintaining the sample location near the axis of symmetry of the pyrometer optical array.

The target assembly is mounted with a three-point adjustable suspension plate, which permits adjustment of the target plane to perpendicularity and concentricity with the projectile launch tube. The

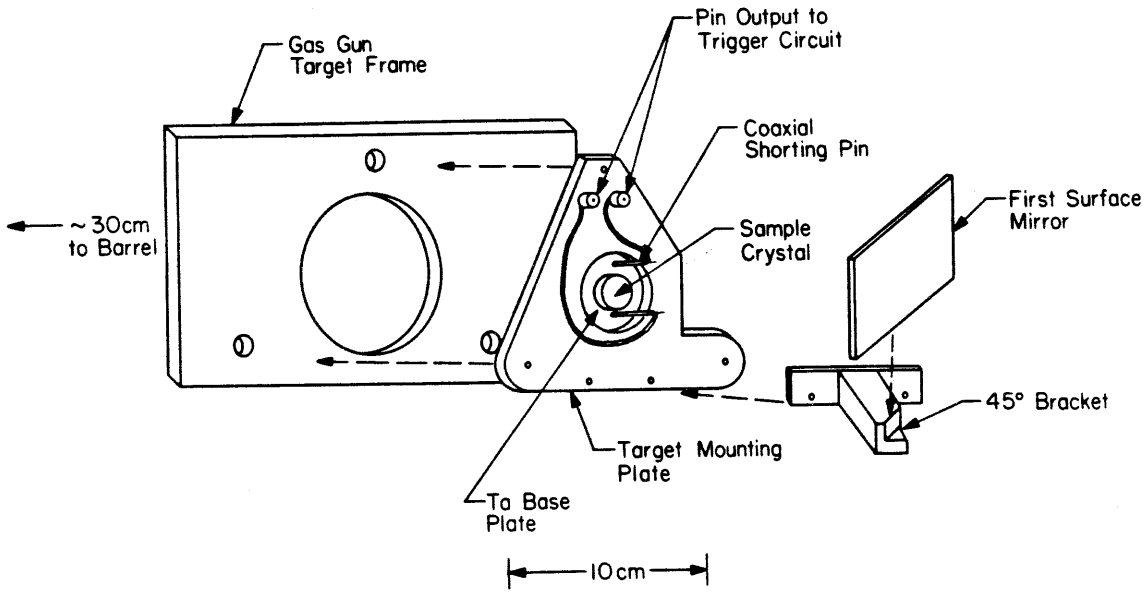

Figure I-1. Light-gas gun target assembly for shock pyrometry experiments. Target plane is adjustable with 3-point suspension, and 45° mirror directs light paths into pyrometer optics. Shorting pins are mounted with contact surfaces at sample/base plate interface plane.

target mounting plate, as illustrated, is a triangular aluminum plate (10 mm thickness), with a central hole to accommodate the sample and with a notch removed to prevent light path obstruction to the pyrometer optical channels. The standard target base plate (usually 1-2 mm thick tantalum) is attached to this plate, with the sample crystal mounted on the base plate rear surface. While the projectile flyer plate diameter is 25 mm in the LLL gun, the sample diameter is typically 17-19 mm in diameter. Sample specimens are cut to 2-4 mm thickness and polished to optical smoothness on each face. Attachment of all target materials is accomplished using epoxy adhesive around component edges, taking care to keep epoxy out of the direct optical path of the pyrometer. Spurious light from edge regions and the epoxy is eliminated by attaching an opaque circular mask to the sample rear surface as the final step of target assembly. This mask restricts the pyrometer view to the central ~10 mm of sample diameter.

Mounted next to the sample on the base plate rear surface are two coaxial self-shorting trigger pins. These pins, which are positioned in a vertical plane through the target center, provide an electronic trigger signal upon shock arrival in the sample, and additionally provide a measurement of projectile "tilt" in the vertical plane. Each of these pins consists of a ~1 mm diameter coaxial conductor pair, with a brass end cap which shorts the outer and center conductors upon the passage of a pressure pulse. These pins are biased at ~150 v. prior to impact, and the shorting pulse is carried through conventional 50 Ω coaxial cable to the appropriate diagnostics.

Finally, an expendable first surface (aluminized) mirror is attached to the target plate with a 45° bracket, thus reflecting light

from the target to the pyrometer optical subsystem, whose axis is perpendicular to the direction of impact, in order to minimize fragment damage to the system.

The pyrometer proper, as shown in Figure I-2, consists of the optical and mechanical assembly entirely outside the evacuated impact tank. Figure I-2 is the cross section in a side view of the pyrometer, so only two of the total of six optical paths are shown. The steel flange plate bolts directly to the side access door of the LLL gun, and vacuum integrity as well as shrapnel protection for the pyrometer optics is afforded by the 10 mm-thick polycarbonate plastic windows. Transmission spectra of commercially available polycarbonate stock (e.g., Lexan and Tuffak brands) verify that it serves as a satisfactory window for wavelengths between 400 and 1100 nm. Vacuum seals are accomplished using conventional neoprene O-rings.

Mounted rigidly to the 19 mm flange plate is the optical frame. Each of the six optical channels consists of a pair of positive achromatic lenses, with a narrow-band interference filter inserted between them. The target-facing and detector-facing lenses of the pair are each 52 mm in aperture diameter and have focal lengths of 508 mm and 193 mm respectively. These focal lengths were selected to be approximately the distances to the target and to the detectors, measured from the lens doublets, so that the light rays between the elements are approximately parallel and strike the interference filters at normal incidence.

The interference filters, which are commercial units of laminated dielectric and glass construction, are removable from their spring clip mountings in the lens cells. Each filter has a transmission half-height

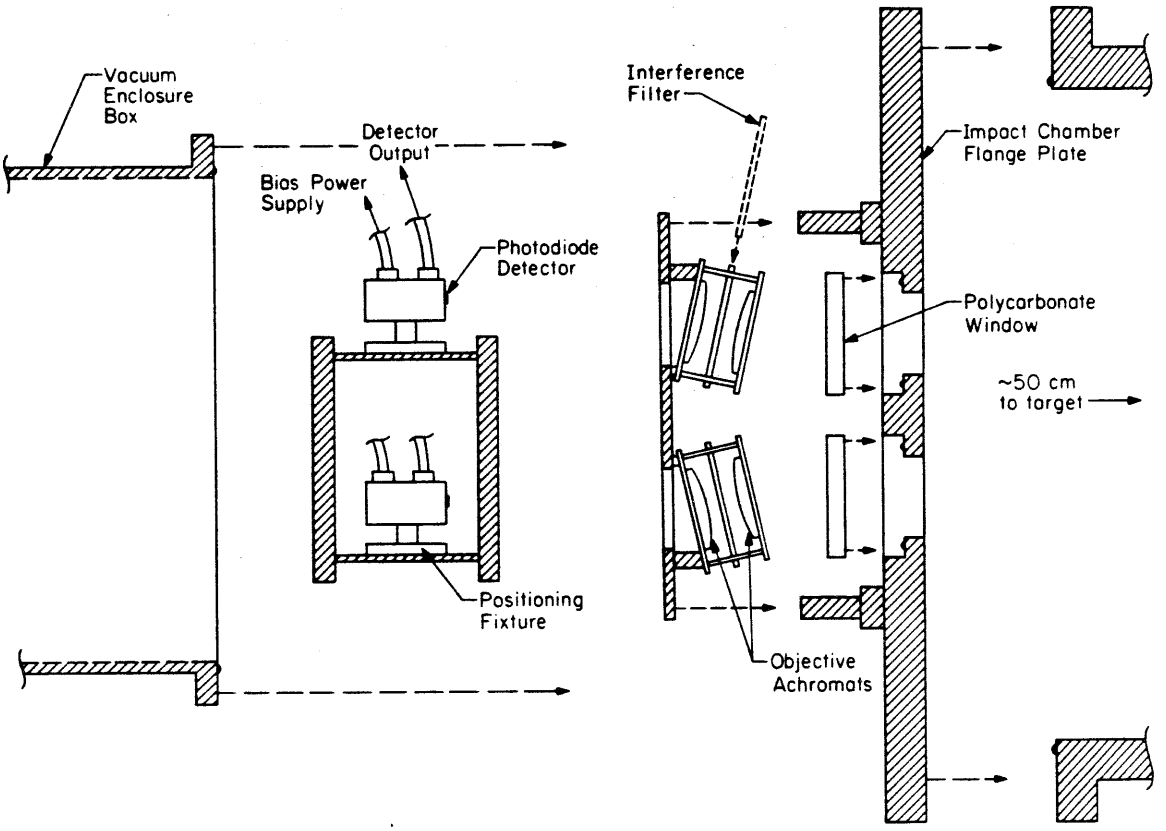

Figure I-2. Exploded view (side cross section) of pyrometer components. Optical elements are fixed to flange plate, while detector array is adjustable in position. Vacuum enclosure box surrounds entire assembly to provide backup vacuum integrity in the event of window failure. Lens aperture is 52 mm and effective system focal length is 140 mm.

wavelength bandwidth of ~9 nm, and the peak transmission of each is ~40%. The central wavelengths of the filters have been determined with a transmission spectrophotometer and are tabulated along with the integrated equivalent bandwidth of each in Table I-1.

The detector rack is located behind the optical frame, supported in the optical focal plane by struts attached to the flange plate (not illustrated). The six individual detectors are mounted on mechanical positioning fixtures, which allow precise adjustment of detector position in all three orthogonal directions.

The entire pyrometer assembly is finally enclosed by a box of 10 mm welded aluminum construction, which provides backup vacuum integrity in the event of a window rupture. As earlier described, the light-gas gun pump gas is hydrogen, so that care must be taken to prevent atmospheric oxygen from entering the hydrogen-filled impact chamber immediately following a shot. Vacuum-secure coaxial BNC feed-through connectors are used to transmit detector signals from the pyrometer and to supply the detectors with external power. Removable side ports allow adjustments and connections to be accomplished with the vacuum box in place.

The detector circuit schematic has been given in Chapter 2. The photodetector, which is a Hewlett-Packard 5802-4207 PIN silicon photodiode, is reverse biased at 10 volts, so that a transmitted photocurrent proportional to the flux of incident photons is produced at the output terminal. This current source drives a 50 Ω effective load, in the form of a coaxial transmission cable, terminated at the recording oscilloscope.

The photodiode active area is approximately 1 mm in diameter, so that it intercepts only a fraction of the ~4 mm diameter area of the

Table I-1

Interference Filter Parameters

Channel identification	Central wavelength λ (nm)	Integrated equivalent bandwidth (nm)
451	450.2	4.37
506	507.9	4.11
546	545.1	4.98
598	598.0	5.04
651	650.0	5.52
793	792.0	8.96

masked target image, which has been demagnified by the focal ratio of approximately 2.6:1. Therefore, in a fixed geometric configuration, the detector output current (or voltage across 50 Ω) is proportional to the image brightness per unit area and is relatively insensitive to small lateral misalignments of the detector and image center. Similarly, sampling only the central portion of the image disk makes the intensity measurement relatively insensitive to depth of focus errors. The central "blur circle" intensity falls off from the value at perfect focus by an amount approximately proportional to the square of the distance from the true focal plane, and in the present case, 0.1% tolerance in detected intensity is obtained with a positioning precision of ~1 mm in focal depth. Furthermore, the image of the shock front remains in satisfactory focus throughout its travel through the sample, since the 3-4 mm shock travel translates into an image shift $(2.6)^2$ times smaller, or ~.5 mm.

Since the onset of shock luminescence in the sample and shorting of the trigger pins occur simultaneously, it is necessary to delay the detector signals relative to the trigger pulses which initiate the oscilloscope sweep. This is accomplished by passing each detector signal through a ~200 ns delay line consisting of low-loss 50 Ω impedance coaxial cable. The voltage waveform then enters the oscilloscope input, with nominal 50 Ω cable termination. The oscilloscopes used in these experiments have been Tektronix models 585 and 7903, with the latter providing superior high-frequency response and greater vertical voltage gain. The scopes are operated with a time base rate of 100 ns per horizontal division in the single sweep mode, and the waveforms are recorded with a Polaroid camera and high-speed (ASA 10,000) recording film. The

photodiode detector has a manufacturer-rated speed of response of ≤ 1 ns with a 50 Ω load, and calibration tests using a pulse-modulated solid-state laser light source have verified that the total system of detectors, cabling, and oscilloscopes are capable of discriminating signals 5 ns or less in duration. In a typical experiment, each of the six detector channels has two cascaded oscilloscopes in parallel with the signal line with different gain sensitivities in order to ensure optimal recording of the signal waveform.

The prompt signals provided by the shorting trigger pins are ultimately routed to three devices. The first of these is the triggering network of the oscilloscope bank. The first pin to close causes the oscilloscope sweeps to begin and fiducial time marks to be superimposed on the beginning of the baselines. Secondly, each of the pin pulses is recorded relative to an absolute time reference fiducial on high-speed Tektronix 519 oscilloscopes. These records provide projectile tilt information. Finally, the trigger pulse provides the stop signal for electronic counters used to measure the projectile flight time.

The most important diagnostic function apart from the pyrometer detectors is the flash x-ray velocity determination. A flash x-ray source with a pulse duration of ~20 ns illuminates the projectile flight path 10 cm. in front of the target face. The shadow of the passing projectile is recorded on Polaroid film, as the x-ray flash is triggered by the projectile interruption of a preceding CW (continuous wave) x-ray beam. The precise location of the target relative to the x-ray photograph frame is determined in a pre-shot calibration photo. A high-speed frequency counter is employed to measure the interval (typically ~20 μs)

between x-ray firing and target pin closing. After corrections are applied for the semi-duration of the x-ray pulse, tilt of the projectile flyer plate and other systematic timing errors, the projectile velocity is determined to within typically 0.2%.

Operational Procedure

The following is a procedural list of events and required operations in the routine conduct of a single shock pyrometry experiment. This list serves as a partial checklist of procedures in preparation for an experiment.

1. Target is mounted in impact tank and adjusted to proper position and orientation for projectile impact.
2. X-ray calibration photo is taken. Photo should show the frame center approximately 9.0-10.0 cm from the target base plate center.
3. New polycarbonate windows are positioned on the door flange plate, which is bolted to the tank door directly adjacent to the target. Window O-rings should be clean and free of cuts. Windows are held in place with a retaining plate finger-tight.
4. Optics frame is bolted to the flange plate with interference filters removed.
5. Detector array is positioned on supporting struts and secured.
6. Small focusing lamp is attached to rear surface of sample crystal. Focusing lamp consists of miniature clear envelope battery-powered bulb.
7. Each channel detector is adjusted in position to give best focus of filament image on detector active area. Adjustment is made for relative depth displacement between bulb filament and actual sample

position. Horizontal positioning fixtures travel on a threaded movement with 32 revolutions per inch of travel.

8. When the focusing procedure is completed, the lamp is removed and the light path is cleared of obstructions.
9. Trigger pin cables within impact tank are connected and verified.
10. Impact tank receives final preparation, is sealed and vacuum pumping begins.
11. Interference filters are inserted into proper optical channels.
12. Internal power supply and signal cables are connected to detector BNC terminals.
13. Vacuum box is installed and cable connections completed to BNC feed-throughs.
14. Vacuum box side ports are installed and box is purged with inert gas (dry nitrogen or argon).
15. External cable connections to oscilloscopes are completed and continuity is verified. Optional signal preamplifiers are connected as necessary.
16. Oscilloscope time bases and vertical sensitivities are calibrated in the settings appropriate to the expected signals. Oscilloscope triggering and cameras are adjusted and verified for single shot exposure.
17. Pyrometer power supply is turned on, and the pyrometer is ready for final gun preparation and firing.

Pyrometer Calibration Procedure

In order to translate experimental signal levels into sample spectral radiance values, calibration must be carried out with a standard light

source of known characteristics. If the calibration is carried out in the same geometric configuration and with the same optical components as in the actual experiment, then a light source of known spectral radiance provides a direct full-system calibration, without the necessity of explicit measurements of detector area, filter bandwidth, optical losses, or subtended solid angles. Any changes in filters or optical components of the pyrometer necessitate recalibration. Sufficient variations (several percent) in the transmission spectra among different lots of window plastic material are observed that recalibration is necessary when changing from one polycarbonate lot to another.

As described in Chapter 2, the standard light source is a tungsten ribbon filament incandescent lamp, which is calibrated in spectral radiance at a specified lamp current and is traceable to National Bureau of Standards sources. The ribbon width is just great enough to illuminate fully the detector active area in the experimental geometry. Table I-2 gives the calibration values for the lamp used in this work, at selected appropriate wavelengths.

The following is a procedural list of steps for the pyrometer calibration. For the purposes of calibration and data reduction, the assumption that the measured spectral radiance is constant across the interference filter line width (~9 nm) introduces negligible error in the present cases.

1. Pyrometer optics and detectors are assembled in the experimental configuration, with the tungsten filament occupying the position of the sample.
2. Fine focusing is accomplished as in the experimental procedure, with

Table I-2

Calibration Lamp Spectral Radiance Values

LLL Standards Lab lamp no. EPT 1013 operated at 35 Amperes A.C.

λ (nm)	Spectral Radiance ($\mu W\ mm^{-2}\ nm^{-1}\ sr^{-1}$)
450	11.6
500	22.9
550	39.6
600	57.7
650	78.3
700	98.5
750	115.
800	126.

interference filters removed.

3. Pyrometer calibration is accomplished at essentially DC response, with light beam interruption by a rotating chopper wheel at ~100 Hz.
4. With chopper rotating and lamp at full current (35 Amperes AC), the detector signal without interference filter is measured in each channel with an oscilloscope. 50 Ω terminators from the experimental layout are used as loads.
5. Since pyrometer signals for the tungsten source at ~2700 K are expected to be prohibitively small, measurements with the narrow band filters in place must be taken with the 50 Ω load omitted, and the oscilloscope high impedance input appears in parallel with the detector circuit internal impedance of ~1 kΩ. This affords an effective gain of 20 in measured voltage. Signal measurements without interference filters and without 50 Ω termination are made to obtain the gain correction for each channel.
6. Signal measurements are made with interference filters in place and without 50 Ω termination. Care should be taken to eliminate sources of external noise, since millivolt-level signals are to be measured with maximum precision (~ a few percent).
7. The calibration factor for each channel is obtained by first obtaining the detector voltages for a 50 Ω load from

$$E_{filter}(50\Omega) = E_{filter}(1k\Omega)\,\frac{E_{white}(50\Omega)}{E_{white}(1k\Omega)}\,. \qquad (1)$$

Dividing the quoted lamp spectral radiance at each wavelength by the signal voltage determined above yields the channel calibration factor,

K_λ in units of watts per square millimeter, per nanometer bandwidth, per steradian, per Volt of signal. Alternatively, this is expressed in the units $W/m^3/sr/V$.

For reference purposes, the calibration factors determined on 10 October 1979 are listed in Table I-3. The pyrometer calibrations obtained in this manner assume that the photodiode quantum efficiency of photocurrent production is constant for response times from DC to the experimental times of 10^{-7} - 10^{-8} s. Furthermore, photocurrent response is assumed proportional to light intensity over the ~3-4 decades of intensity variation between calibrations and experiments. This is consistent with the manufacturer's quoted response linearity over six decades.

The uncertainty in the standard lamp spectral radiance calibration is quoted at ~2-3%, and this limits the precision of the pyrometer calibration. The assumed impedance constancy of the 50 Ω cable terminations from DC up to 10^8 Hz introduces 1% or less uncertainty in the calibration. Experiments have verified that delay cable dispersion introduces no measurable amplitude effect in this frequency range. Therefore, the calibrations given here and the radiance measurements in Appendix II have associated with them a conservatively estimated uncertainty of approximately 4%.

Table I-3

Pyrometer Calibration Factors

Measured 10 October 1979 in LLL Standards Lab.

Channel Identification	λ (nm)	K_λ ($Wm^{-3}\ sr^{-1}\ V^{-1}$)
451	450.2	8.007×10^{14}
506	507.9	5.295×10^{14}
546	545.1	5.024×10^{14}
598	598.0	3.965×10^{14}
651	650.0	3.913×10^{14}
793	792.0	1.500×10^{14}

Appendix II

EXPERIMENTAL SPECTRAL RADIANCE MEASUREMENTS USED IN SHOCK TEMPERATURE DETERMINATIONS

The experimentally measured spectral radiance values for studied samples in the shock pyrometry investigations are tabulated here. The reported intensity values have been obtained from measurements of detector voltage amplitude on oscilloscope records. The calibration factors used for conversion of these voltage measurements into spectral radiance values were obtained by the procedure outlined in Appendix I. In all cases, the intensity measurements refer to the terminal value recorded at the end of shock transit in the sample. As discussed in Appendix I and Chapter 2, the estimated uncertainty in spectral radiance measurements is approximately 4%, although isolated examples of larger systematic deviations occur.

Tables II-1 through II-6 contain the unreduced data for shock pyrometry experiments on NaCl, H_2O, α-quartz, fused silica, forsterite (Mg_2SiO_4) and silver (Ag). Each of these tables contains the identification number, tantalum impactor velocity, and calculated pressure for each shot. The spectral radiance measurements are reported in units of 10^{13} W/m^3/sr, and each of the six measurements at different wavelengths is identified in the column headings by the channel wavelength numbers given in Appendix I.

The temperature and emissivity determinations reported in this thesis have been obtained through a least squares fit of the spectral radiance data to a Planck spectrum. The spectral radiance for emission normal to the surface of the radiating region is assumed to be given by

$$N_\lambda = \varepsilon C_1 \lambda^{-5} [\exp(C_2/\lambda T) - 1]^{-1} \qquad (1)$$

where in SI units, $C_1 = 1.191066 \times 10^{-16}$ Wm^2/sr and $C_2 = 1.43883 \times 10^{-2}$ m-K. If the angular dependence of the radiated flux obeys the blackbody cosine law, then the cancelling effect of area foreshortening as seen by the fixed area detectors causes (1) to be measured with equal validity at all viewing angles. The temperature T and emissivity ε are derived from this fit with uncertainties which reflect the approximate range of solutions consistent within the radiance values and uncertainties.

Table II-1

NaCl Spectral Radiance Data

Shot No.	Ta Flyer Velocity (km/s)	Hugoniot Pressure (GPa)	Spectral Radiance (10^{13} $Wm^{-3}sr^{-1}$)					
			451	506	546	598	651	793
NaCl-2	5.5	87	2.15	--	6.21	--	2.44	--
NaCl-3	5.801	95.0	4.15	4.45	3.96	3.51	3.34	1.99
NaCl-4	6.176	104.5	8.20	--	7.46	6.51	4.97	3.40
NaCl-5	4.899	74.5	.538	.624	.706	.731	.831	.615
NaCl-6	4.797	72.5	.266	.399	.467	.500	.532	.382

Table II-2

H_2O Spectral Radiance Data

Shot No.	Ta Flyer Velocity (km/s)	Hugoniot Pressure (GPa)	Spectral Radiance (10^{13} $Wm^{-3}sr^{-1}$)					
			451	506	546	598	651	793
WET-2	6.2	70	.420	.451	.519	.514	.587	.426
WET-3	6.657	78.5	1.17	1.34	1.27	1.31	1.29	.922
WET-4	5.689	61.0	.197	.288	.283	.364	.374	.320
WET-6	4.906	49.0	--	.0442	.0538	.0710	.0822	.0890

Table II-3

α-quartz Spectral Radiance Data

Shot No.	Ta Flyer Velocity (km/s)	Hugoniot Pressure (GPa)	Spectral Radiance (10^{13} $Wm^{-3}sr^{-1}$)					
			451	506	546	598	651	793
XQ-1	5.720	109.7	2.77	--	--	--	2.53	--
XQ-2	4.600	75.9	.418	.524	.565	.603	.608	.506
XQ-3	5.172	92.5	1.48	1.62	1.59	1.63	1.64	1.13
XQ-4	4.952	85.9	.594	.932	.929	.983	1.03	.740
XQ-5	5.660	107.8	2.03	2.43	2.64	2.23	2.38	1.54
XQ-6	5.395	99.3	1.64	1.96	2.02	1.96	1.91	1.29
XQ-7	5.926	116.5	.748	.943	1.04	.963	1.10	.776
XQ-9	6.297	126.6	1.23	1.49	1.58	1.49	1.48	1.01
XQ-10	6.600	137.0	1.97	2.33	2.35	2.10	2.06	1.28

Table II-4

Fused Quartz Spectral Radiance Data

Shot No.	Ta Flyer Velocity (km/s)	Hugoniot Pressure (GPa)	Spectral Radiance (10^{13} $Wm^{-3}sr^{-1}$)					
			451	506	546	598	651	793
FQ-3	6.483	109.9	5.20	6.07	5.89	4.49	4.45	2.55
FQ-5	5.437	81.2	1.07	1.23	1.17	1.28	1.09	.889
FQ-6	5.134	73.3	.557	.692	.685	.733	.795	.628
FQ-7	6.285	104.2	3.75	4.16	4.00	3.41	3.40	2.02
FQ-8	5.888	93.2	1.92	2.30	2.43	2.14	2.13	1.34
FQ-9	4.543	58.9	.782	1.04	1.12	1.09	1.11	.806
FQ-10	4.943	68.5	.955	1.21	1.29	1.28	1.27	.897

Table II-5

Forsterite Spectral Radiance Data

Shot No.	Ta Flyer Velocity (km/s)	Hugoniot Pressure (GPa)	Spectral Radiance (10^{13} $Wm^{-3}sr^{-1}$)					
			451	506	546	598	651	793
Fo-1	6.520	166	--	--	.536	--	--	--
Fo-2	6.713	175	.556	.820	.658	.681	.730	.552
Fo-3	6.184	153	.324	.410	.468	.500	.520	.427

Table II-6

Ag Spectral Radiance Data

Shot No.	Ta Flyer Velocity (km/s)	Released State Pressure (GPa)	Spectral Radiance (10^{13} $Wm^{-3}sr^{-1}$)					
			451	506	546	598	651	793
Ag-2	4.373	134.7	.721	.860	.904	.916	.967	.675